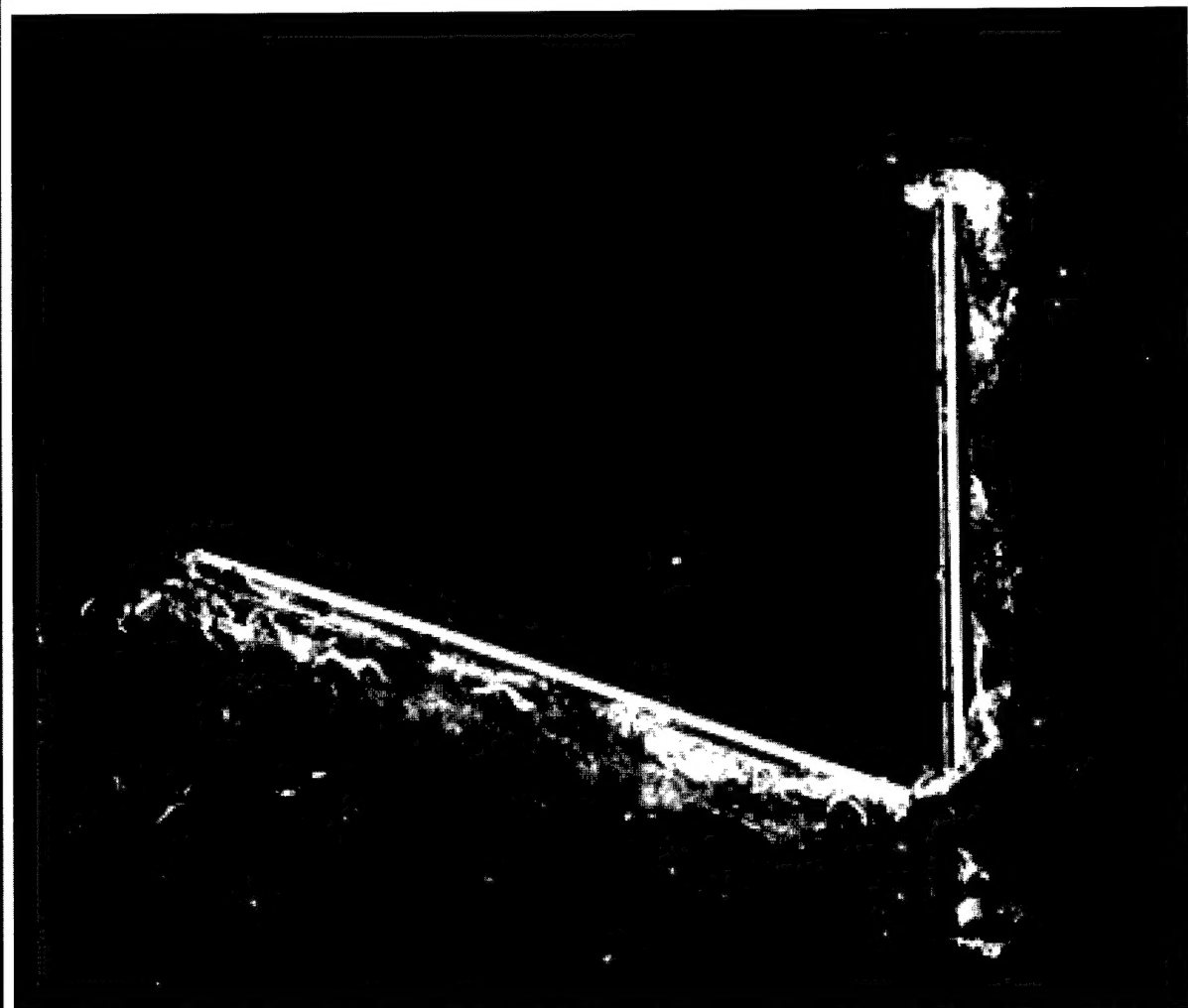


**US Army Corps  
of Engineers®**  
Engineer Research and  
Development Center

## **Analytical and Numerical Models of the RIBS XM99 Ocean-Scale Prototype**

Michael J. Briggs

September 2001



The contents of this report are not to be used for advertising, publication, or promotional purposes. Citation of trade names does not constitute an official endorsement or approval of the use of such commercial products.

The findings of this report are not to be construed as an official Department of the Army position, unless so designated by other authorized documents.



PRINTED ON RECYCLED PAPER

# **Analytical and Numerical Models of the RIBS XM99 Ocean-Scale Prototype**

by Michael J. Briggs

Coastal and Hydraulics Laboratory  
U.S. Army Engineer Research and Development Center  
3909 Halls Ferry Road  
Vicksburg, MS 39180-6199

Final report

Approved for public release; distribution is unlimited

# Contents

---

Preface .....	vii
Conversion Factors, Non-SI to SI Units of Measurement .....	viii
1—Introduction .....	1
Background .....	1
Breakwater Performance .....	3
RIBS Design .....	4
Purpose .....	8
Report Organization .....	9
2—Analytical Models .....	10
Wave Transmission .....	10
Hydrodynamic Pressure .....	15
3—Numerical Model .....	17
WAMIT Theoretical Development .....	17
Output Quantities .....	20
WAMIT Model Generation .....	21
4—Wave Environment .....	26
Processing Algorithms .....	26
Wave Parameters .....	27
5—Field Measurements .....	39
Transmission Coefficients .....	39
Wave Pressures .....	40
6—Results and Discussion .....	43
Transmission Coefficients .....	43
Dynamic Pressures .....	48
7—Summary and Conclusions .....	62
References .....	66
Appendix A: Mass Moments of Inertia .....	A1

## List of Figures

---

Figure 1.	Rapidly Installed Breakwater System (RIBS) concept	5
Figure 2.	Cross section of RIBS XM99	6
Figure 3.	Analytical model of RIBS XM99	11
Figure 4.	WAMIT panel layout - plan view	22
Figure 5.	WAMIT panel layout - 3-D view	23
Figure 6.	RIBS XM99 wave direction orientation	24
Figure 7.	Incident significant wave heights	28
Figure 8.	GEDAP significant and maximum wave heights	28
Figure 9.	Incident wave periods	30
Figure 10.	GEDAP significant and maximum wave periods	30
Figure 11.	MLM incident wave direction and directional spread	31
Figure 12.	Frequency spectrum and directional spreading, unimodal sea	32
Figure 13.	Directional wave spectrum, unimodal sea	33
Figure 14.	Directional wave spectrum, unimodal swell	34
Figure 15.	Directional wave spectrum, bimodal with dominant sea mode	35
Figure 16.	Directional wave spectrum, bimodal with dominant swell mode	36
Figure 17.	Joint distribution of wave period and height	37
Figure 18.	Joint distribution of wave period and wave direction	38
Figure 19.	Joint distribution of wave period and directional spread	38
Figure 20.	Wave transmission coefficient analysis by frequency	44
Figure 21.	Wave transmission coefficients	45
Figure 22.	Joint distribution of wave period and wave transmission based on zero moment wave height	46
Figure 23.	Joint distribution for wave period and wave transmission based on simple average for short range of frequencies	46
Figure 24.	Measured vs. WAMIT wave transmission coefficients	47

Figure 25. External pressure analysis for bow, middle, and stern stations of top level .....	49
Figure 26. Net pressure analysis for bow, middle, and stern stations at the top middle pressure gage location .....	50
Figure 27. Average atmospheric pressure for three reference gages .....	51
Figure 28. Measured external and internal pressure gage depths .....	51
Figure 29. Top level external pressure gage depths .....	52
Figure 30. Middle level external pressure gage depths .....	53
Figure 31. Bottom level external pressure gage depths .....	53
Figure 32. Time series of net pressure for top middle location .....	54
Figure 33. Time series of net pressure for top stern location .....	54
Figure 34. Time series of net pressure for middle middle location .....	55
Figure 35. Time series of net pressure for middle stern location .....	55
Figure 36. Time series of net pressure for bottom middle location .....	56
Figure 37. Time series of external pressure gage statistics for top middle location .....	57
Figure 38. Time series of internal pressure gage statistics for top middle location .....	57
Figure 39. Time series of net pressure gage statistics for top middle location .....	58
Figure 40. Time series of significant and maximum net pressures on top level .....	58
Figure 41. Time series of significant and maximum net pressures on middle level .....	59
Figure 42. Time series of significant and maximum net pressures on bottom level .....	59
Figure 43. WAMIT external dynamic pressure, 3-D view .....	60
Figure 44. WAMIT external dynamic pressure, three gage levels .....	61
Figure 45. Comparison of analytical, WAMIT, and measured external pressures .....	61
Figure A1. Schematic of RIBS XM99 for moment of inertia calculations ..	A2
Figure B1. Time series of external pressure gage statistics for top bow location .....	B2
Figure B2. Time series of external pressure gage statistics for top stern location .....	B2
Figure B3. Time series of external pressure gage statistics for middle bow location .....	B3

Figure B4. Time series of external pressure gage statistics for middle middle location .....	B3
Figure B5. Time series of external pressure gage statistics for middle stern location .....	B4
Figure B6. Time series of external pressure gage statistics for bottom bow location .....	B4
Figure B7. Time series of external pressure gage statistics for bottom middle location .....	B5
Figure B8. Time series of external pressure gage statistics for bottom stern location .....	B5
Figure B9. Time series of internal pressure gage statistics for top stern location .....	B6
Figure B10. Time series of internal pressure gage statistics for middle middle location .....	B6
Figure B11. Time series of internal pressure gage statistics for middle stern location .....	B7
Figure B12. Time series of internal pressure gage statistics for bottom middle location .....	B7
Figure B13. Time series of net pressure gage statistics for top stern location .....	B8
Figure B14. Time series of net pressure gage statistics for middle middle location .....	B8
Figure B15. Time series of net pressure gage statistics for middle stern location .....	B9
Figure B16. Time series of net pressure gage statistics for bottom middle location .....	B9

## **List of Tables**

---

Table 1. Incident Wave Angles: Global, Analytical, and Numerical .....	24
Table 2. Wave Parameters for Numerical Model .....	25
Table 3. Short, Missing, Bad, and Edited Wave Data .....	29
Table 4. Interesting Wave Conditions .....	37
Table 5. Pressure Gage Codes .....	40
Table 6. Pressure Gage Coordinates .....	41

# Preface

---

This report describes analytical and numerical models of the Rapidly Installed Breakwater System (RIBS) XM99 ocean-scale floating breakwater study conducted at Cape Canaveral, FL, by the U.S. Army Engineer Research and Development Center (ERDC), Coastal and Hydraulics Laboratory (CHL), Vicksburg, MS.

The ERDC study team was under the technical direction of Dr. Donald T. Resio, Senior Research Scientist. Significant technical assistance in conducting the study was provided by Dr. Jeffrey A. Melby, Harbors and Entrances Branch (HN-H), Dr. Leon E. Borgman, consultant, Dr. Nobuhisa Kobayashi, University of Delaware, Dr. Jimmy E. Fowler and Mr. Ivano Mileto, HN-H.

This study was conducted during the period May 1999 through June 1999 under the general supervision of Dr. James R. Houston, former Director, CHL; Mr. Thomas W. Richardson, Acting Director CHL; Mr. Gene Chatham, Chief, HN; and Mr. Dennis G. Markle, Chief, HN-H.

At the time of publication of this report, Dr. James R. Houston was Director of ERDC, and COL John W. Morris III, EN, was Commander and Executive Director.

*The contents of this report are not to be used for advertising, publication, or promotional purposes. Citation of trade names does not constitute an official endorsement or approval of the use of such commercial products.*

# Conversion Factors Non-SI to SI Units of Measurement

---

Non-SI units of measurement used in this report can be converted to SI units as follows:

Multiply	By	To Obtain
Acres	4,046.873	Square meters
Cubic feet	0.028317	Cubic meters
Cubic yards	0.7645549	Cubic meters
Feet	0.3048	Meters
Miles (U.S. nautical)	1.852	Kilometers
Miles (U.S. statute)	1.609347	Kilometers
Tons (long, 2,240 lb mass)	1,016.047	Kilograms

# 1 Introduction

---

This report describes analytical and numerical modeling efforts to quantify the performance and response of a new type of Rapidly Installed Breakwater System (RIBS) being developed at the U.S. Army Engineer Research and Development Center's (ERDC) Coastal and Hydraulics Laboratory (CHL). The RIBS concept was initially developed to address problems encountered by military personnel during Logistics-Over-The-Shore (LOTS) operations. The primary problem occurs during these operations when sea states become elevated and negatively impact crews trying to discharge cargo and equipment onto smaller vessels from Tactical Auxiliary Crane Ships (TACS) and roll-on/roll-off (RO/RO) vessels. The goal of the RIBS is to provide a protected offshore area where offloading operations can safely continue during these elevated sea states.

## Background

### **Historical perspective (abstracted from Fowler 1997)**

The U.S. Army Corps of Engineers has the primary technical role in breakwater design and construction in the United States. Over the last 50 years, they have been actively engaged in a wide range of breakwater research, relating to civil and military missions. Breakwaters can be broadly classed into two categories: gravity-based and floating. Gravity-based structures rest on the bottom and form barriers to wave propagation. They maintain stability by incorporating sufficient mass within individual structural elements to resist wave-induced motions. If a gravity-based breakwater does not extend to the water surface, it is termed a "submerged" or berm breakwater. Gravity-based breakwaters are the types of breakwater commonly seen in most ports and harbors around the world. The second class of breakwater, floating breakwaters, occupy only the top section of the water column and must be anchored to the sea floor to maintain position and orientation.

Floating wave breakwaters have historically been referred to as vertical wave barriers, curtain walls, wave screens, etc. For many years, ERDC has been involved with the design and deployment of floating breakwaters, primarily for application within bays or estuaries that are semiprotected from very large wave generation. Such structures typically are intended to attenuate waves with

heights not exceeding 1.2 m (4 ft) and periods not exceeding 4 sec. Extrapolation to an open ocean environment is at least an order of magnitude greater in difficulty. In an oceanic environment, waves with heights up to 6.1 m (20 ft) are common during storm conditions, with associated periods up to 18 sec. One of the most famous floating breakwaters was the Bombardon floating breakwater along the Normandy coast during World War II. It was deployed in depths of approximately 27.4 m (90 ft) mean sea level (msl) at a rate of about 305 to 366 m (1,000 to 1,200 ft) per day (Jones 1971). Although it was credited with providing valuable protection during the early phases of the invasion, a major storm heavily damaged it after only a few weeks of operation.

### **Military significance**

Today's military must be capable of quickly and efficiently projecting its forces to any location around the globe. Furthermore, once these forces are on the ground, it is critical to adequately sustain these forces. Since 90 percent of the Army's equipment is moved via Sealift, there is a mandate for a strong chain of operations that can create robust, sea-based links between major depots within the U.S. and potential operational areas around the world. Recent investments in infrastructure within the U.S. and in large Sealift ships have greatly increased our capacity to get necessary supplies to ports of debarkation in any theater. However, there are insufficient areas around the world that have large port facilities available that can directly load or off-load modern deep-draft Sealift ships. Furthermore, given the importance of such facilities to U.S. force projection and sustainment, it is quite likely that such facilities would be high-priority targets for enemy actions. Given the limited number of ports around the world that meet Army needs for force projection and sustainment, and the likelihood that such ports may be damaged or denied to U.S. forces, it is critical that the Army maintain realistic force-projection alternatives to large shore-based port facilities.

The only reasonable alternative available today is via Logistics Over the Shore (LOTS) or Joint Logistics Over the Shore (JLOTS, when two or more services are involved) operations. In these operations, supplies from Sealift ships are offloaded at offshore anchorages onto smaller vessels termed lighters. Lighters then transport the supplies to smaller ports and harbors, to causeways along the shore, or directly onto the beach.

### **The problem**

Existing LOTS capabilities allow operations to be conducted in sea states 1 and 2, or significant wave heights up to 0.9 m (3 ft). Sea state 3 (SS3) conditions consist of waves with peak periods in the range 3 to 6 s and significant wave heights between 0.9 to 1.5 m (3 to 5 ft). Throughput rates documented during a LOTS exercise conducted at Ft. Story, VA, in 1984, show that SS3 conditions seriously diminish or halt system throughput altogether. In 1991 and again in

1993, results from two major LOTS exercises provided evidence that ships and lighters were unable to perform their roles in SS3.

If global sea states remained primarily in sea states 1 and 2 and only rarely attained SS3 and higher levels, the inability to continue operations into these conditions would not be a serious problem for U.S. forces. However, extensive studies have concluded that SS3 conditions can be expected well over 50 percent of the time in many areas of U.S. interest around the globe. As an example of the problems that this can cause, Operation Restore Hope in Somalia in 1993 was plagued by the inability to maintain adequate throughput of critical supplies (Briggs et al. 1996). Gen. Gordon R. Sullivan, then Army Chief of Staff, concluded that one of the primary contributors to these shortages was the inability of the ships offshore to discharge their cargo in SS3.

## Breakwater Performance

According to Jones (1971), an ideal wave barrier will have the following performance characteristics: (a) good performance or attenuation of wave energy in the operating range of wave conditions, (b) high mobility or readily and rapidly transportable with existing land and sea equipment and constraints, (c) quick installation and removal without undue difficulty, (d) able to survive a "design" storm, (e) economic to build and use, and (f) reusable. Unfortunately, performance and mobility are somewhat conflicting requirements. As a result, we have never had a truly effective floating breakwater in energetic wave environments, with most being relegated to the relatively benign wave climates in sheltered marinas and aquiculture facilities.

Of the criteria above for rating a floating breakwater, the most important is performance or wave attenuation. Wave attenuation is accomplished by wave reflection, interference due to wave radiation, and energy extraction/dissipation due to breaking, turbulence, and friction. Based on his survey of performance data from 106 laboratory and field tests, Jones found that the velocity field is the most important parameter affecting floating breakwater performance. For water depth to wavelength ratios of  $d/L > 0.5$  (i.e., deepwater waves), the wave has circular orbits that decrease rapidly with distance below the surface. The velocity is only one-fifth of its surface value at middepth. This condition corresponds to waves with wave periods smaller than about 4.4 sec in 15.2-m (50-ft) water depth. Therefore, a fairly rigid barrier from the surface with depth of submergence (i.e., draft) less than the full depth blocks out a significant portion of the kinetic energy and is relatively effective. A barrier blocking the upper half of the water column should be able to block 96 percent of the waves energy (i.e., 4 percent transmitted,  $K_t = 0.2$ ) associated with SS3 waves.

For intermediate and shallow-water waves (i.e.,  $d/L \leq 0.5$ ), however, the water particle motions are more in a horizontal line, moving to and fro. The amplitude and speed of the water particles become constant over the entire water column as the wave becomes a shallow water wave. The same barrier occupying only 50 percent of the water column would transmit 49 percent of the wave

energy. To achieve a reduction of 96 percent as before, the depth of submergence would have to be 90-95 percent of the water column.

Jones also found that wave steepness and relative breakwater length parallel to the wave travel (i.e., width) are important parameters affecting wave attenuation. Although less important, wave steepness becomes more significant if breaking and turbulence are present. Of course, larger wave heights require a larger structure for survivability and overtopping. For floating breakwaters aligned normal to the wave direction, the relative length should be greater than unity. In general for a given wavelength, if the draft is small, the relative length must be larger, and vice versa. Thus, if the draft is relatively shallow, the breakwater width needs to be longer to compensate.

Jones also reported that previous tests and studies have shown that to be effective, floating breakwaters must have widths on the order of one-fourth to one-third of the wavelength being attenuated and be very rigid and massive to prevent the breakwater from acting as a wavemaker. In addition, floating breakwaters have (a) a strong dependence of breakwater performance on wave period, (b) mooring difficulties, and (c) higher potential for structural failures during large wave events. These factors were the driving force behind recent floating breakwater developments at ERDC.

## RIBS Design

### Concept

The new concept of RIBS was designed with the breakwater performance criteria previously described. This concept promises to expand floating breakwater technology by allowing operations in SS3 conditions. The driving force behind the RIBS concept has been the fact that SS3 is a "war stopper" for present force projection plans and technology. The objective of RIBS is to reduce the waves from SS3 to SS2 within the lee of the structure to facilitate JLOTS and other civilian operations along exposed portions of the world's coastlines.

RIBS is a floating breakwater with two legs in a "V" shape in plan view, that provide a sheltered region from waves and currents (Figure 1). The legs of the RIBS can consist of a continuous rigid structure, a hinged structure with one or more joints, a flexible water beam membrane structure, or a hybrid of rigid and flexible components. Based on previous experience, it appears that the RIBS legs will need to be of the order of 1.5 to 3 wavelengths in length and extend through the water column a depth sufficient to deflect most of the wave energy. In the past, floating breakwaters were generally positioned broadside to the incoming waves. The RIBS concept is based on the ability of the thin leg structures to diffract and reflect waves because of the angle the legs make to the incoming waves (Resio et al. 1997). Each leg of RIBS acts as a diffraction element for obliquely incident waves, leaving calm water inside and behind the

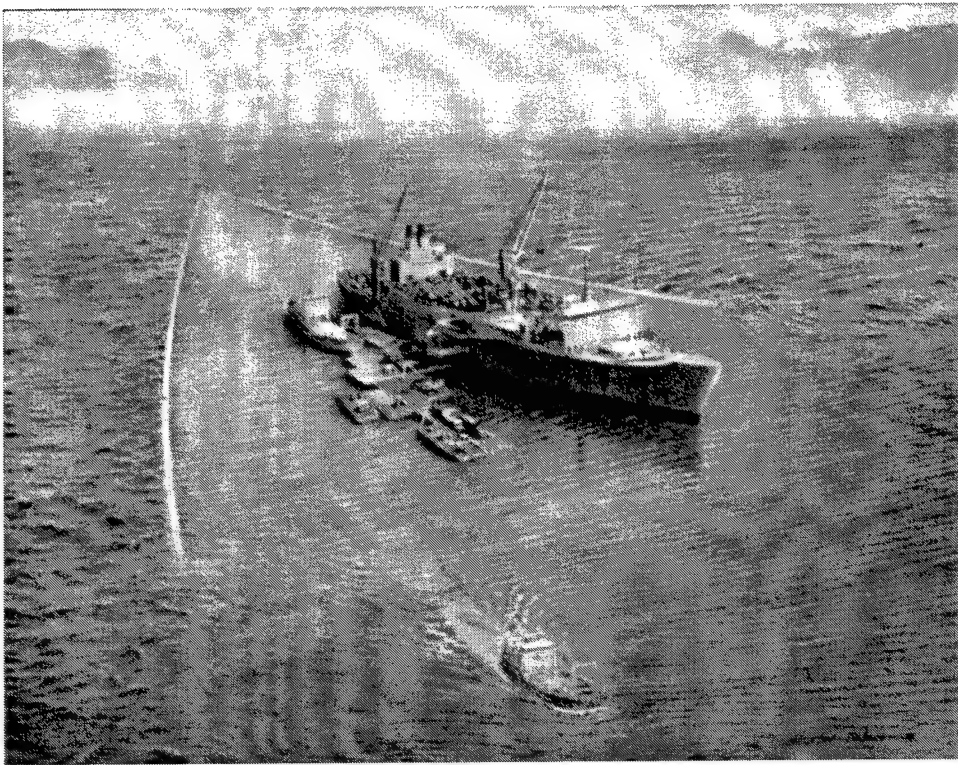


Figure 1. Rapidly Installed Breakwater System (RIBS) concept

structure. Mooring loads are minimized because the structure is designed to deflect incoming waves rather than absorb and reflect them.

The goal of the RIBS program is to produce a floating breakwater that can meet the Department of Defenses's (DOD) needs for sea-state mitigation during JLOTS operations. To accomplish this, the final version of the RIBS must (a) reduce wave heights by at least 50 percent in the lee of the breakwater; (b) be rapidly deployable, even in SS3, and (c) be transportable with existing Army assets or a plan must exist to acquire necessary deployment assets.

Since the beginning of the RIBS program in 1995, more than 100 laboratory and four field experiments have been conducted in support of the RIBS development (Briggs et al. 1996; Fowler et al. 1996; Briggs, Demirbilek, and Matheu 1998). The RIBS XM99 is the latest of the field models tested in the RIBS program.

### RIBS XM99 Field Study

**Specifications.** The RIBS XM99 was deployed in Melbourne, FL, for 10 days from May 20 to 30, 1999. This ocean-scale version had full scale dimensions, except that it was only about two-thirds as long as the final design. The XM99 version explored a new construction concept that resembled a Venetian blind. It was also known as the "VE-RIBS," or vertically expandable RIBS

because the legs tripled their draft once placed in the water. Each leg was 77.1 m (253 ft) long, 2.4 m (8 ft) wide, and 7.3 m (24 ft) deep. Water depth in the test site averaged 13.4 m (44 ft) during the deployment. The legs consisted of four horizontal levels, constructed from Mabey Truss frames, and attached to each other by a fabric material on all sides (Figure 2). The 2-m-tall (6.4-ft-) top

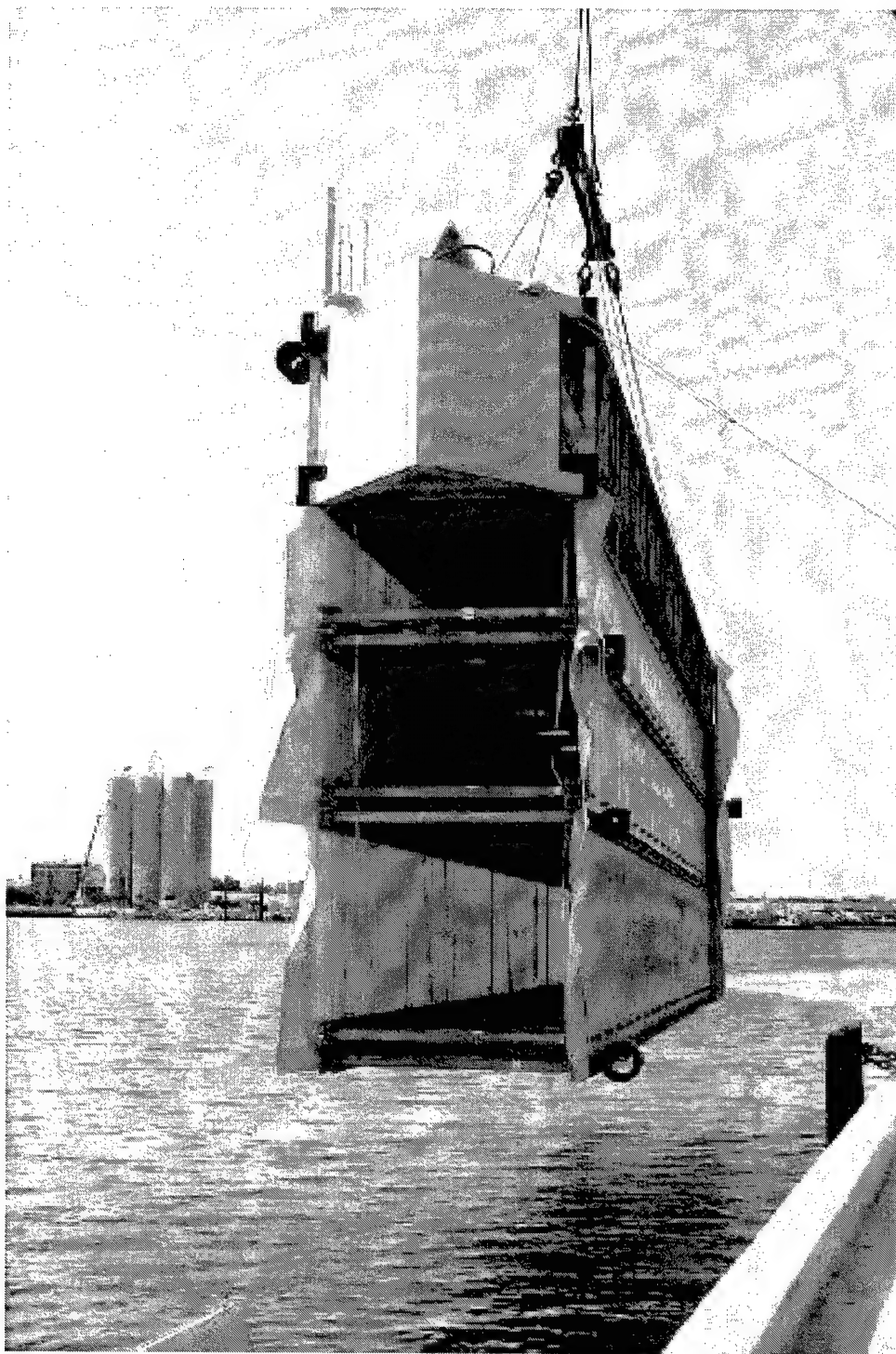


Figure 2. Cross section of RIBS XM99

layer or top deck is the main structural element from which the other layers are supported. The vertical distance between each layer is variable: 0.9 m, 1.2 m, 1.8 m (3 ft, 4 ft, and 6 ft) from the top down. To relieve large vertical and lateral bending stresses, it had four 61-cm-long (2-ft-) joints at the corners of the top deck, 45.7 m (150 ft) from the bow of each leg. Design values for the horizontal area moments of inertia  $I_{xx}$  for the top deck and other three levels were 6,119,000 and 2,622,000  $\text{cm}^4$  (147,000  $\text{in}^4$  and 63,000  $\text{in}^4$ ), respectively. Likewise, vertical area moments of inertia  $I_{yy}$  were 2,248,000 and 10,800  $\text{cm}^4$  (54,000  $\text{in}^4$  and 260  $\text{in}^4$ ).

The XM99 was moored at three points from buoys at the bow and stern of each leg.

**Instrumentation.** The XM99 instrumentation included sensors for measuring (a) incident wind, wave, and currents, (b) transmitted waves and pressures, and (c) structural motions, loads, and strains. Data for the entire system was monitored, collected, analyzed, and stored by an Integrated Motion Monitoring Information System (IMMIS) designed in cooperation with Coastal Leasing, Inc. These data were collected by "master-slave" data loggers located longitudinally at the bow, middle, and stern of each leg. Most of this instrumentation was concentrated on the top deck of the port leg, but some was also located on the starboard leg and the lower levels of the port leg. Sampling rates for most instrumentation was 4 Hz, with analog inputs of 0-5 volts direct current (VDC). A self-contained, omnidirectional datasonics acoustic telemetry modem transferred data to a shore-based data acquisition and analysis system.

A datawell directional buoy, located about 457 m (1,500 ft) in front of the XM99, measured incident wave conditions. Transmitted wave heights were measured with a Datawell nondirectional buoy, located 30.5 m (100 ft) from the nose or bow of the XM99 along the center line. An acoustic doppler current profiler (ADCP) measured currents. An anemometer recorded wind conditions during the study.

Five Trimble Global Positioning System (GPS) loggers were located on the top deck of each leg to monitor six degrees of freedom (DOF) motions. These integrated, 12-channel GPS receivers are capable of submeter positioning accuracy and provide superior weak-signal reception, allowing differential corrections over long distances and challenging weather conditions.

Triaxial accelerometers were installed on four levels of the port leg to measure vertical, lateral, and surge accelerations. On the external side, 12 accelerometers were located at bow, middle, and stern stations on the surface, top deck, middle, and bottom levels. On the internal side, five accelerometers were located at middle and stern stations on the top and middle levels and middle station on the bottom level. In addition, three accelerometers were mounted on the external side fabric panels at bow, middle, and stern locations between the top deck and second level of the port leg. Acceleration ranges between  $\pm 2$  g's were recorded.

Pressure gages were co-located with the accelerometers (except for the three surface stations) to collect wave-induced pressures for calibrating the hydrodynamic pressure estimates from the analytical and numerical models.

Hitec Products strain gages were located on the top deck for measurements of vertical and lateral bending moments. Nine strain gages were positioned at the corners and the diagonal at the bow, middle, and stern station cross sections. These gages are one-eighth in. long, full bridge with 100 ohm strain elements, temperature compensated, and attached to stainless steel shims that were welded and bolted to the structure. These gages have excellent signal to noise ratio and low power consumption. They were calibrated so that 0.1 to 5 VDC corresponds to  $\pm 1,000$  microstrain.

Finally, mooring line loads were measured with national scale load cells at the three ends of the XM99. These units were sized for a 76 mm (3 in.) shackle pin for 445 kN (100 kip) loads at the stern ends and 1,112 kN (250 kip) load at the bow. Output signals were from 0.1 to 5 VDC for zero to full scale of the load link.

## Purpose

The analytical and numerical model studies conducted for the RIBS XM99 field study are described in this report. Various closed-form solutions for vertical barriers with simplified boundary conditions exist in the literature (Resio, Fowler, and Briggs 1995). These formulations are based on linear, asymptotic approximations for an infinitely long barrier. In real-world situations, however, complicated geometries and floatation elements produce very complex, nonlinear systems. Consequently, although an understanding of the physics of these systems can provide guidance for the overall direction of these studies, mathematical and computer solutions are not yet capable of providing realistic solutions. Therefore, efforts have concentrated on laboratory-scale models and ocean-scale field trials of various RIBS concepts. In these experiments, V-shaped floating structures have been exposed to a wide range of incident wave conditions that have validated the RIBS concept. Thus, a key objective of this research is to compare the measured performance to predicted values from analytical and numerical models. A long-term goal is to improve these predictive capabilities with empirical relationships from measured data.

Hydrodynamic analysis is used to estimate the response of a structure to waves in the six rigid body modes of surge, sway, heave, pitch, roll, and yaw. The focus in this report is the hydrodynamic parameters of wave transmission and dynamic pressure. Of the criteria for rating a floating breakwater, the most important is performance, as quantified by wave transmission. Dynamic pressures are an important quantity because they are used to calculate the wave forces and moments, operational stresses, and ultimate RIBS design for survivability.

Since RIBS is large relative to the wavelength of the design SS3 wave conditions, its presence will affect the wave field. Therefore, a three-dimensional, numerical radiation/diffraction code is required to perform the hydrodynamic analysis of the wave-structure interaction. The numerical model used in this study is the linear radiation/diffraction program Wave Analysis MIT (WAMIT) for the analysis of wave-structure interaction. There are no analytical tools available for predicting wave transmission and dynamic pressures of the complicated RIBS floating structure in irregular seas. However, there are two analytical models for wave transmission of rigid, thin, vertical barriers in the presence of normally incident waves that will be used in this research. Unfortunately, there is very little available for predicting dynamic pressures.

## Report Organization

In Chapter 2, the analytical models of wave transmission and dynamic pressure are described. The WAMIT numerical model, boundary value problem, and parameter formulations are described in Chapter 3. Chapter 4 describes the procedures used to analyze the field data for wave transmission and dynamic pressure. The wave environment during the RIBS XM99 deployment is described in Chapter 5. Predictions from the analytical and numerical models are compared to each other and the field measurements of transmission coefficients and dynamic pressure in Chapter 6. Finally, a summary and conclusions are presented with recommendations for future research in the last chapter.

## 2 Analytical Models

---

In this chapter, analytical models for wave transmission and dynamic pressure are described.

### Wave Transmission

#### Background

Breakwater performance or effectiveness is usually defined by the transmission coefficient  $K_T$ , that relates the size of the transmitted wave to the incident wave as

$$K_T = \frac{H_T}{H_I} \quad (1)$$

where  $H_T$  is the transmitted wave height and  $H_I$  is the incident wave height. A value of  $K_T = 0.50$  or less is indicative of very good performance as the transmitted wave height is reduced to one half of its incident value, equivalent to only 25 percent of its incident energy.

Wave transmission for a floating breakwater is a function of many wave and structural parameters. Wave parameters include the wave period or frequency, wavelength, wave height, water particle velocity, water depth, and wave direction. Structural parameters include the structure length, depth of submergence (i.e., draft), rigidity, and orientation to incident waves.

#### Theory

Either simple analytical or complex numerical methods can be used to predict wave transmission for rigid, thin, vertical barriers in the presence of normally incident waves. Various simple analytical solutions are available (Ursell 1947; Wiegel 1960; Kriebel and Bollmann 1996). Numerical solutions include various methods (Liu and Abbaspour 1982; Losada, Losada, and Roldan 1992; Mandal and Dolai 1994; Sawaragi 1995). In contrast, very little field and laboratory data

exist for floating breakwaters, mostly for regular waves only (Wiegel 1960; Peratovich, Nottingham, and Drage, Inc. 1992; Kriebel and Bollmann 1996).

In this report, only the analytical theories of Wiegel (1960) and Kriebel and Bollman (1996) are presented. This report also includes some of the ideas expressed by Kobayashi (1998). Both analytical models are based on linear theory and can be represented by the definition sketch shown in Figure 3 for the XM99. The fixed, impermeable, vertical legs form a "V" with an interior angle of  $\theta_r$ . The wave transmission of oblique waves problem is defined within two regions. Region 1 consists of the incident and reflected waves and Region 2 the transmitted waves. The origin of the coordinate system is at the bow of the XM99, with the positive y-axis along the starboard leg, the x-axis normal to this leg, and the z-axis positive up from the still-water surface. The water depth is defined by  $h$  and the draft of the XM99 by  $d$ . The incident wave angle  $\theta_I$  is measured counterclockwise from the positive x-axis. Oblique waves in the range  $0 \leq \theta_I \leq 90$  deg are considered in this analysis. Regular (i.e., monochromatic) waves are defined by the wave period  $T$  and wave height  $H_I$ . Regular waves are used in the analysis for simplicity. Reflected and transmitted waves are characterized by wave heights  $H_R = K_R H_I$  and  $H_T = K_T H_I$ , where  $K_R$  and  $K_T$  are reflection and transmission coefficients, respectively. Evanescent or spurious waves from the breakwater motions are higher-order phenomenon that are assumed to be small and decay rapidly with distance from the legs.

In the analytical model for wave transmission, the legs are assumed to be fixed, rigid, thin, vertical, and infinitely long. These assumptions are considered a reasonable first approximation. The fixed and rigid assumption is predicated on the fact that the bending rigidity of the RIBS legs is sufficient to prevent the XM99 from acting as a wavemaker, so that the displacements are reasonably small relative to the wave height. The beam of the XM99 is small relative to the wavelengths in SS3, so the thin assumption is justified. The vertical assumption

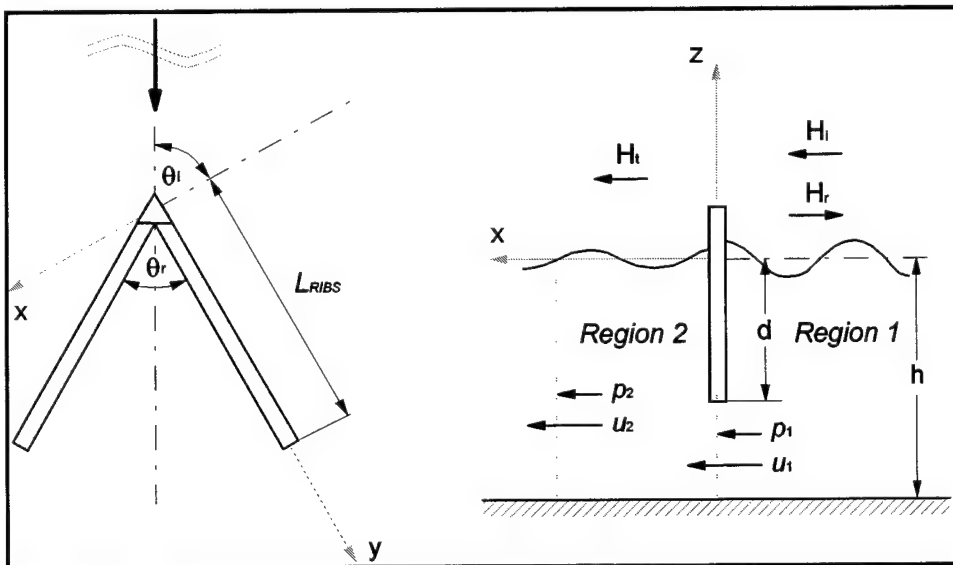


Figure 3. Analytical model of RIBS XM99

is warranted as long as the inclination angle of the RIBS leg does not exceed about 20 deg from the vertical (Liu and Abbaspour 1982). The infinitely long assumption is valid if the dimensions of the legs are sufficiently large relative to the projected wavelengths along the x- and y-axes. One final assumption is that the transmitted waves from the starboard leg are not reflected from the port leg back into the interior of RIBS. Of course, this does occur, but it is assumed to be a small effect.

Free surface elevations for the incident  $\eta_I$  and reflected  $\eta_R$  waves in Region 1 are given by linear wave theory as

$$\eta_I = \frac{H_I}{2} \cos(k_x x + k_y y - \omega t) \quad (2)$$

$$\eta_R = \frac{H_I}{2} K_R \cos(-k_x x + k_y y - \omega t + \varphi_R) \quad (3)$$

where

$k_x = k \cos \theta_I$  = wave number in the x-direction,

$k_y = k \sin \theta_I$  = wave number in the y-direction,

$k$  = wave number given by  $kg \tanh kh = \omega^2/g$ ,

$\omega = 2\pi/T$  = angular frequency,

$K_R$  = reflection coefficient, and

$\varphi_R$  = reflection phase difference.

Units of  $\eta_I$  and  $\eta_R$  are the same as  $H_I$  and  $H_R$ . In Region 2, the transmitted wave elevation  $\eta_T$  is

$$\eta_T = \frac{H_I}{2} K_T \cos(k_x x + k_y y - \omega t + \varphi_T) \quad (4)$$

where  $K_T$  is the transmission coefficient and  $\varphi_T$  is the transmission phase difference. The two phase differences  $\varphi_R$  and  $\varphi_T$  can be neglected without any loss of generality and are done so from here on in the derivations.

The wave transmission beneath the RIBS leg is a function of the time-averaged energy flux, or rate of work done by the dynamic pressure. This is known as the transmitted wave power and is equal to the incident wave power under the barrier. Wave power is the time average over one wave of the depth-integrated product of dynamic pressure and horizontal fluid velocity. In Region 1, the dynamic pressure  $p_1$  and horizontal velocity  $u_1$  are given by

$$p_1 = \rho g K_p (\eta_I + \eta_R) \quad (5)$$

$$u_1 = \frac{gk}{\omega} K_p (\eta_I - \eta_R) \cos \theta_I \quad (6)$$

where the pressure response factor  $K_p$  is

$$K_p = \frac{\cosh[k(h+z)]}{\cosh kh} \quad (7)$$

In Region 2, the dynamic pressure  $p_2$  and horizontal velocity  $u_2$  are

$$p_2 = \rho g K_p \eta_T \quad (8)$$

$$u_2 = \frac{gk}{\omega} K_p \eta_T \cos \theta_I \quad (9)$$

The time-averaged energy flux  $F_1$  in Region 1 is

$$F_1 = \frac{1}{T} \int_0^T \int_{-h}^{-d} p_1 u_1 dz dt = \frac{\rho g^2 k}{8\omega} H_I^2 \frac{\sinh[2k(h-d)] + [2k(h-d)]}{4k \cosh^2 kh} (1 - K_R^2) \cos \theta_I \quad (10)$$

Similarly in Region 2, the energy flux  $F_2$  is

$$F_2 = \frac{1}{T} \int_0^T \int_{-h}^0 p_2 u_2 dz dt = \frac{\rho g^2 k}{8\omega} H_I^2 \frac{\sinh(2kh) + 2kh}{4k \cosh^2 kh} K_T^2 \cos \theta_I \quad (11)$$

Setting the two energy fluxes equal to each other, Kriebel and Bollman (1996) obtained an expression for the transmission coefficient

$$K_T = \sqrt{(1 - K_R^2) T_F} \quad (12)$$

where the factor  $T_F$  is defined as

$$T_F = \frac{\sinh[2k(h-d)] + 2k(h-d)}{\sinh(2kh) + 2kh} \quad (13)$$

Kriebel and Bollman's (1996) relationship for  $K_T$  includes the effects of the reflected waves and was called the Modified Power Transmission Theory (MPTT). Wiegel (1960) developed the original Power Transmission Theory (PTT) for the wave transmission coefficient, that did not include the effects of reflected waves

$$K_T = \sqrt{T_F} \quad (14)$$

Kriebel and Bollman (1996) obtained an expression relating the transmission and reflection coefficients by assuming continuity of the horizontal water particle velocities at the boundary along the starboard leg (i.e.,  $x = 0$ ) between the two regions

$$K_T = 1 - K_R \quad (15)$$

Finally, they set the two expressions in Equations 12 and 15 equal to each other and solved for  $K_T$  as a function of  $T_F$

$$K_T = \frac{2T_F}{1 + T_F} \quad (16)$$

Both Wiegel (1960) and Kriebel and Bollman (1996) assumed that the waves were normal to the breakwater leg (i.e.,  $\theta_I = 0$  deg). Therefore, their derivations did not include the  $\cos \theta_I$  term in the previous equations. However, as can be seen in the derivations for  $K_T$  in Equations 14 and 16, wave transmission appears to be independent of the incident wave direction (since there is no term involving  $\theta_I$ ), even if it is included in the derivation.

Other researchers have found a small variation in  $K_T$  with incident wave direction. Losada et al. (1992) found that  $K_T$  is almost constant in the range  $0 \leq \theta_I \leq 60$  deg and approaches zero as  $\theta_I \rightarrow 90$  deg. Sawargi (1995) noted in his book that  $K_T$  was essentially unchanged for  $\theta_I \rightarrow 40$  deg from the normal to the breakwater.

Since  $K_T$  and  $K_R$  are related, knowing  $K_R$  should be useful in estimating  $K_T$ . Helm-Petersen (1998) investigated the reflection coefficients  $K_R$  of three types of coastal structures with vertical fronts using multidirectional seas (up to 30 deg directional spreading) in a physical model. Coastal structures included a vertical porous structure (i.e., gabion baskets), and caissons with vertical fronts (fully reflecting), perforated vertical fronts with 25 percent porosity, and vertical fronts on top of impermeable mounds with and without berms. Of course, these structures extend to the bottom, so no wave transmission under the structure is included in these reflection coefficients. For the porous vertical structure, Helm-Petersen found that  $K_R$  varied between 0.6 and 0.8, decreased as the peak frequency increased, and remained constant for wave directions from 0 deg (i.e., normal) to 30 deg. For caissons with vertical fronts,  $K_R$  was about 0.95 and showed little variation with incident wave angle (0 to 40 deg) or directional spreading. For the porous vertical front caissons,  $K_R$  decreased from 0.5 for 0 deg incident wave angle to 0.3 at an angle of 60 deg. Finally, for vertical caissons on mounds,  $K_R$  ranged from 0.6 for a mound with no berm to 0.35 with a berm. Thus, one might expect that the wave transmission coefficient is not too sensitive to wave directions up to about 40 deg from the normal to the breakwater, although it might tend to increase since the reflection coefficient is decreasing.

In summary, wave transmission coefficients are mainly a function of the wave period  $T$  or wavelength  $L$ , the water depth  $h$ , and the draft or depth of submergence  $d$  of the RIBS. Typical nondimensional parameters used to describe the performance are the relative water depth  $h/L$  and the relative draft of the breakwater  $d/h$ . There is probably some variation in the transmission coefficient with incident wave direction. What has not been considered in these derivations is wave energy dissipation. From an energy balance standpoint, the incident energy should equal the sum of the reflected, transmitted, and dissipated energy. Wave energy dissipation can occur due to wave breaking, absorption, turbulence, and flow separation under the legs due to the oscillatory nature of the waves.

## Hydrodynamic Pressure

Dynamic pressures are an important quantity because they are used to calculate the wave forces and moments, operational stresses, and ultimate RIBS design for survivability.

### Theory

The total wave pressure consists of a hydrostatic term  $p_{static}$  and a hydrodynamic  $p_{dyn}$  term.

$$p_{tot} = p_{static} + p_{dyn} = -\rho g z + \rho g \eta K_p \quad (17)$$

where  $\rho$  is the density of water,  $g$  is gravitational acceleration,  $z$  is the vertical coordinate measured positive upward from the water surface,  $\eta$  is the free surface elevation, and  $K_p$  is the pressure response factor. The hydrostatic term is a constant term based on position in the water column and controls the buoyancy force on the RIBS. The dynamic pressure controls the wave forces and the degree of bending on the RIBS. In developing the wave transmission model, Kriebel and Bollman (1996) derived a formulation for the dynamic pressure that includes the incident and reflected pressure. This derivation has been widely accepted and is used in this report.

The  $p_1$  external (i.e., Region 1) and  $p_2$  internal (i.e., Region 2) pressures were derived previously in the section on wave transmission and are repeated here.

$$p_1 = \rho g K_p (\eta_1 + \eta_R) \quad (18)$$

$$p_2 = \rho g K_p \eta_T \quad (19)$$

These equations for  $p_1$  and  $p_2$  are the same as Equation 17 except that the value for  $\eta$  in Equation 17 has been replaced by the appropriate value in Regions 1

and 2. The same assumptions as previously stated for the wave transmission coefficient apply.

To estimate forces and moments on RIBS, the differential or net dynamic pressure  $p_{net}$  is required. Therefore,  $p_{net}$  is defined as the difference between the external and internal pressures (corresponding to Regions 1 and 2)

$$p_{net} = p_1 - p_2 = \rho g K_p (\eta_I + \eta_R - \eta_T) \quad (20)$$

For a thin RIBS leg (which was our original assumption), this reduces to

$$p_{net} = \rho g K_p (1 - K_T) H_I \cos(k_y y - \omega t) \quad (21)$$

where the relationship given by Equation 17 for  $K_R$  and  $K_T$  has been used. Since the beam  $B$  of the RIBS XM99 is 2.4 m (8 ft), we can include some phase difference across the leg by retaining the x-axis term  $\cos(k_x x)$ . Equation 21 then becomes

$$p_{net} = \rho g K_p (1 - K_T) H_I \cos(k_x x) \cos(k_y y - \omega t) \quad (22)$$

The horizontal wave force acting on a unit length of the RIBS can then be calculated by integrating this value for the net pressure over the draft of the RIBS. A total horizontal wave force estimate would be obtained by integrating this unit force over the entire length of the RIBS. Bending moments and stresses can be determined from the unit wave force using simple beam theory with appropriate end conditions.

# 3 Numerical Model

---

## WAMIT Theoretical Development

The numerical program WAMIT (Wave Analysis MIT), developed by the Massachusetts Institute of Technology, was used in this study (Newman 1994; Lee 1995a and 1995b; Newman 1997). It solves a boundary value problem consisting of finding the velocity potential that satisfies the Laplace equation and four linearized boundary conditions for the free surface, bottom, body surface, and the radiation condition at infinity. The numerical solution is the boundary element method based on a three-dimensional, constant panel method (CPM) that determines radiation and diffraction velocity potentials on the body wetted surface using Green's theorem by adjusting the strength of the distributed sources over the panels. The analysis is performed in the frequency domain, with the flow assumed to be ideal and time-harmonic. In the solution, WAMIT provides the excitation forces and motion amplitudes and phases for a fixed or freely floating body resulting from diffraction and/or diffraction plus radiation potentials. Fluid loading on a rigid, floating RIBS, the diffraction and radiation solution, is reported.

Among the available general purpose boundary element codes for performing linear radiation/diffraction analysis of floating bodies, WAMIT is probably the most robust and computationally efficient. The code has been thoroughly benchmarked for accuracy and is the industry standard. It was developed by a consortium composed of industry and academic sponsors including Chevron, Det Norske Veritas, Exxon, Mobil, Naval Surface Warfare Center, Norsk Hydro, Offshore Technology Research Center, Petrobras, Saga, Shell, and Statoil. Krouse (1998) describes the feasibility studies being carried out by McDermott Technology Inc. and the Gulf Coast Regional Maritime Technology Center for the mobile offshore base using WAMIT to estimate Response Amplitude Operators (RAO) for the rigid body motions.

Fathi, Lee, and Newman (1994) used WAMIT to calculate the exciting forces and RAO's for a floating flexible container. Zhao and Triantafyllou (1994) used WAMIT to study the hydroelastic response of long flexible tubes in waves. Newman (1994) presented several examples illustrating the capabilities of the WAMIT numerical model for deformable bodies. Included among the examples were bending of a floating barge and motions of two barges connected by a

hinge. Lee (1997) used WAMIT to study the wave-interaction and structural deflections of a very large floating structure (VLFS). The structure was idealized as a barge, floating on shallow water, and approximated as a plate.

### Boundary value problem

The fluid is assumed to be inviscid and incompressible and the flow irrotational. Small amplitude, time harmonic motions are assumed to justify linearization and superposition. Potential theory permits the representation of the velocity field by the gradient of the velocity potential  $\phi$ , which must satisfy Laplace's equation in the fluid domain

$$\nabla^2 \phi = 0 \quad (23)$$

Linearized boundary conditions on the free surface  $z = 0$  and bottom  $z = -h$  are

$$\frac{\partial \phi}{\partial z} = \frac{\omega^2}{g} \phi \quad (24)$$

$$\frac{\partial \phi}{\partial z} = 0 \quad (25)$$

where  $\omega$  is incident wave angular frequency and  $g$  is gravitational acceleration. The velocity potential of the incident wave is therefore

$$\phi_i = \frac{igA}{\omega} K_p e^{-ik(x \cos \theta_i + y \sin \theta_i - \omega t)} \quad (26)$$

where  $A$  is wave amplitude,  $\theta_i$  is incident wave angle,  $K_p$  is the pressure response factor defined as

$$K_p = \frac{\cosh k(h+z)}{\cosh kh} \quad (27)$$

$h$  is water depth, and  $k$  is the wave number which satisfies the dispersion relation

$$\frac{\omega^2}{g} = k \tanh kh \quad (28)$$

Linearization permits the decomposition of the total velocity potential into two components

$$\Phi = \Phi_R + \Phi_D \quad (29)$$

where  $\Phi_R$  is the radiation potential and  $\Phi_D$  is the diffraction potential. Similarly, the diffraction potential can be expressed as the combination of the incident wave potential  $\Phi_I$  and a scattered potential  $\Phi_S$

$$\Phi_D = \Phi_I + \Phi_S \quad (30)$$

The scattered potential is due to the disturbance of the incident wave field by the fixed body. Again, by superposition, we can define the radiation potential as

$$\Phi_R = \sum_{j=1}^6 \xi_j \Phi_j \quad (31)$$

where  $\xi_j$  are the complex motion amplitudes corresponding to the six rigid-body degrees of freedom and  $\Phi_j$  are the unit amplitude radiation potentials in each mode in the absence of waves.

The appropriate boundary conditions for the diffraction problem are imposed on the undisturbed position of the body surface  $S_B$  by equating the normal derivatives of  $\Phi_D$  to zero

$$\frac{\partial \Phi_D}{\partial n} = 0 \quad (32)$$

where the unit vector  $n$  is normal to the body boundary and points out of the fluid domain.

The final condition to make the boundary value problem unique is to prescribe a radiation condition at infinity. This condition states that any waves on the free surface, other than those due to the incident wave themselves, are due to the body and are radiating and decaying away from the body. The incident wave potential is excluded from this condition. The radiation boundary condition is also known as the Sommerfeld condition and is defined by

$$\Phi_S \propto e^{i\omega x}, \quad \text{as } x \rightarrow \pm\infty \quad (33)$$

### Integral equations for the velocity potential

The boundary value problem is solved in WAMIT using Green's theorem to derive an integral equation for the diffraction velocity potentials on the body surface

$$2\pi\phi_D(x) + \iint_{S_b} \phi_D(\xi) \frac{\partial G(\xi, x)}{\partial n_\xi} d\xi = 4\pi\phi_I d\xi \quad (34)$$

The Green's function or wave source potential  $G(\xi, x)$  is the velocity potential at the point  $x$  due to a point source of strength  $-4\pi$  located at the point  $\xi$ . It satisfies the free surface and radiation boundary conditions and in finite depth is given by

$$G(x, \xi) = \frac{1}{r} + \frac{1}{r''} + 2 \int_0^\infty \frac{(k+K)\cosh k(z+h)\cosh k(\zeta+h)}{k \sinh kh - K \cosh kh} e^{-kh} J_0(kr) dk \quad (35)$$

where

$$r^2 = (x - \xi)^2 + (y - \eta)^2 + (z - \zeta)^2 \quad (36)$$

$$(r'')^2 = (x - \xi)^2 + (y - \eta)^2 + (z + \zeta + 2h)^2 \quad (37)$$

and  $J_0(kr)$  is the Bessel function of order zero,  $(\xi, \eta, \zeta)$  are coordinates of the source points,  $r$  and  $r''$  are radial distances from source points.

For small values of  $r$ ,  $r'$ , and  $r''$ , singular components of the Green's function may occur. Also, a logarithmic singularity may occur for small values of  $r'$  in the ascending series expansion of the wave source potential. These small values usually occur when the source and field points are close to each other and to the free surface. These types of problems are overcome by increasing the number of panels (i.e., decreasing the size of the panels) around the perimeter of the structure and along the free surface. A cosine spacing or finer regular spacing in these areas usually ensures convergence of the discretization scheme.

## Output Quantities

### Wave transmission coefficient

The free-surface elevation is obtained from the dynamic free surface

$$\eta = -\frac{1}{g} \left\{ \frac{\partial \phi}{\partial t} \right\}_{z=0} \quad (38)$$

boundary condition. The nondimensional form is equivalent to the transmission coefficient and is given by

$$\bar{\eta} = \frac{\eta}{A} = K_T \quad (39)$$

where  $A$  is wave amplitude. These values are calculated at each of the specified field points in the fluid domain.

### Dynamic pressure

The dynamic pressure on the body surface is related to the velocity potential by the linearized Bernoulli equation

$$p = -\rho \frac{\partial \phi_D}{\partial t} \quad (40)$$

The normalized pressure is

$$\bar{p} = \frac{p}{\rho g A} \quad (41)$$

where  $\rho$  is water density and  $A$  is the wave amplitude.

The hydrodynamic pressure acting on the central point of each panel consists of components from the incident, scattered, and radiation potentials. The incident and scattered pressures are due to the pressure from the incident waves on the motionless structure. The radiated pressure component is due to the motion of the RIBS in still water.

## WAMIT Model Generation

From a hydrodynamic point of view, the RIBS XM99 structure is relatively simple and can be modeled as a flat, rectangular barge using the program BARGEN (barge generation) preprocessing code. Because of symmetry, BARGEN only requires input for the quarter model (i.e., quadrant) for each leg. Since only one leg of RIBS is created, the program TRANSFORM rotates, shifts, and images the BARGEN single leg model to the full, two-legged RIBS model with the proper interior angle. The POTEN (for wave potentials) module of WAMIT solves for the velocity potentials on each panel of the body for each component of the radiation and diffraction problem and the FORCE (for wave force) module evaluates the force coefficients, and field points for free-surface elevations and fluid pressures.

The WAMIT model of the RIBS XM99 had leg lengths of 76.2 m (250 ft), beam of 2.4 m (8 ft), and draft of 7.3 m (24 ft). The two legs were connected with an interior angle of 60 deg. Each leg (i.e., sides, ends, and bottom) was discretized with 2,596 panels using 50 longitudinal, 2 transverse, and 24 vertical panels with equal spacing. Thus, the panels were 1.5 m (5 ft) long, 1.2 m (4 ft) wide, and 0.3 m (1 ft) high. The right-hand coordinate system was located with the origin at the surface and centered along the longitudinal center line, half way

from the bow or nose of the structure. Two- and three-dimensional views of the panel layout are shown in Figures 4 and 5, respectively.

Wave conditions were selected to cover a range of wave periods and wave directions, representative of sea state 3 and those likely to occur during the deployment. Ten wave periods from 3 to 12 sec were modeled. Figure 6 is a schematic of the actual RIBS XM99 orientation. The “design” orientation of the XM99 was for the nose or bow to point to 135 deg so that waves traveling towards 315 deg (i.e., from 135 deg) were aligned with the center line or x-axis. In the WAMIT model, wave directions are measured counterclockwise from the x-axis. Waves with directions parallel to the center line of 0 deg (i.e., 315 deg), parallel to the starboard leg of 30 deg (i.e., 285 deg), and normal to the port leg of 60 deg (i.e., 255 deg) were simulated. Because of symmetry, only the half plane was modeled. Table 1 lists the correspondence between the analytical and numerical models and the global coordinate system. The operating window of the XM99 was 120 deg, clockwise from 255 to 15 (i.e., 375) deg.

Newman and Lee (1992) recommends a minimum of 6 to 12 panels per wavelength for the smallest wavelength (i.e., highest frequency). The

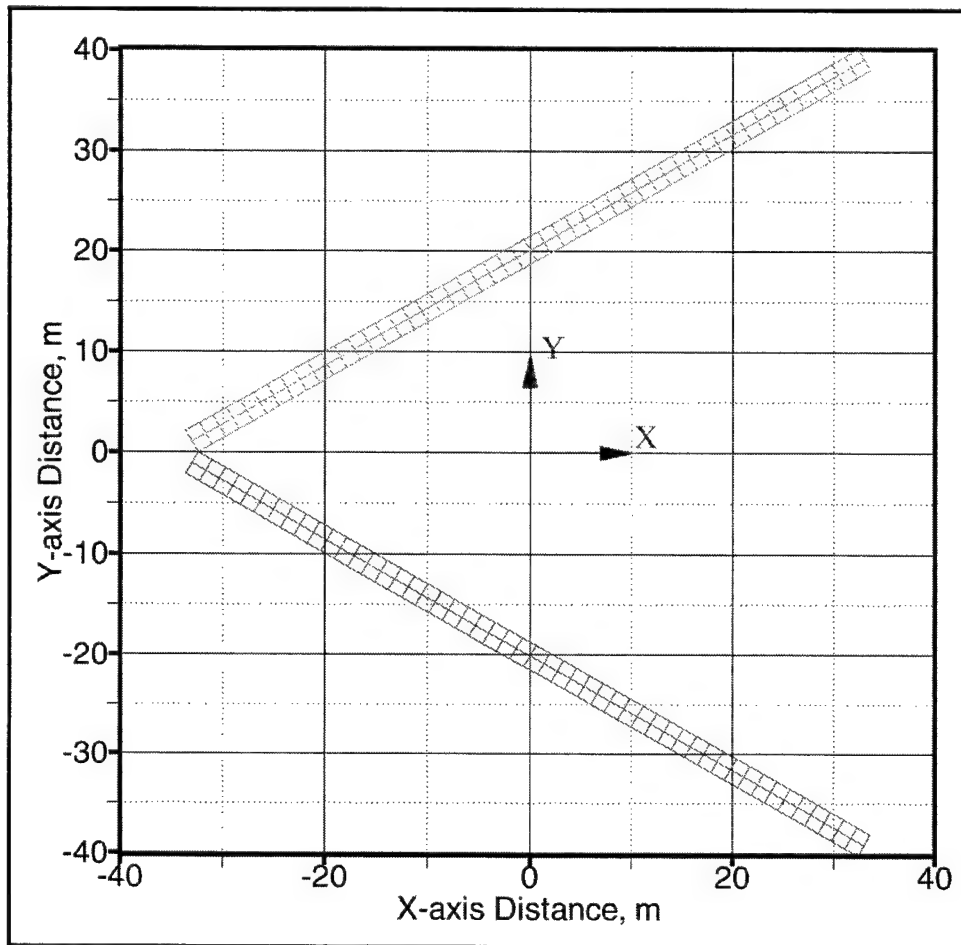


Figure 4. WAMIT panel layout - plan view

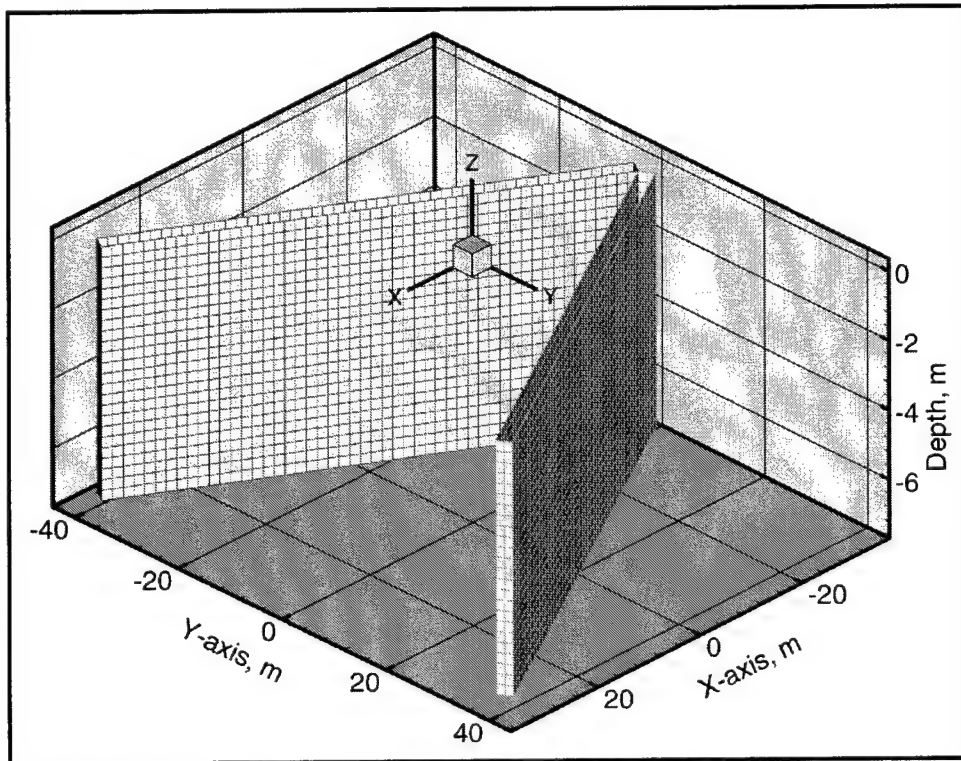


Figure 5. WAMIT panel layout - 3-D view

longitudinal panel length of 1.5 m (5 ft) corresponds to a minimum of 9.2 panels per wavelength for the shortest wavelength of 14.0 m (46 ft) at 3 sec. The leg length is equivalent to 5.4 wavelengths for this 3-sec wave period. The corresponding values for the longest wave at a 12 sec wave period (128.9 m wavelength) are 84.7 panels per wavelength and leg length of 0.6 times the wavelength. Table 2 lists the wavelengths, wave numbers, number of panels per wavelength, and wavelengths per leg for each wave period.

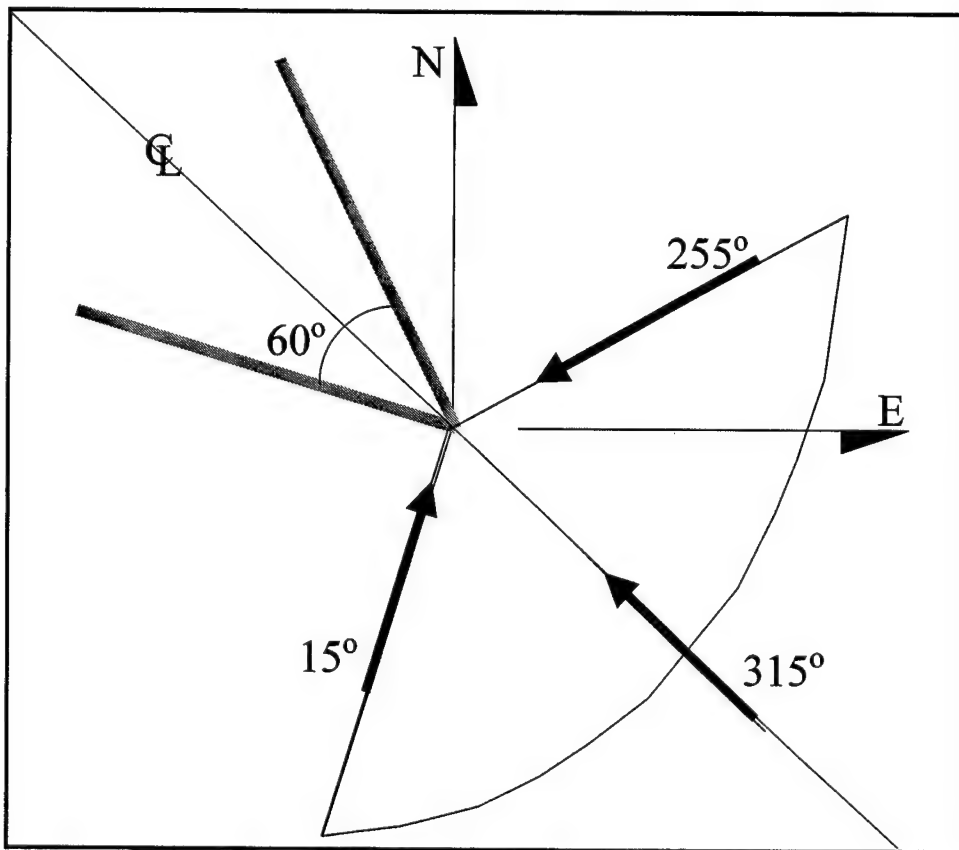


Figure 6. RIBS XM99 wave direction orientation

**Table 1**  
**Incident Wave Angles: Global, Analytical, and Numerical**

Compass, deg	Analytical, deg	WAMIT, deg	Comment
15 (375)	0	-60	Normal to starboard leg
345	30	-30	
315	60	0	Along center line
285	90	30	
255	120	60	Normal to port leg

**Table 2**  
**Wave Parameters for Numerical Model**

Period, T sec	Wavelength, L		Wave Number, k	
	ft	m	1/ft	1/m
3.0	46.08	14.05	0.1364	0.4474
3.5	62.67	19.10	0.1003	0.3289
4.0	81.63	24.88	0.0770	0.2525
4.5	102.56	31.26	0.0613	0.2010
5.0	124.77	38.03	0.0504	0.1652
5.5	147.55	44.97	0.0426	0.1397
6.0	170.36	51.93	0.0369	0.1210
6.5	192.93	58.81	0.0326	0.1068
7.0	215.16	65.58	0.0292	0.0958
7.5	237.04	72.25	0.0265	0.0870
8.0	258.59	78.82	0.0243	0.0797
8.5	279.85	85.30	0.0225	0.0737
9.0	300.86	91.70	0.0209	0.0685
9.5	321.65	98.04	0.0195	0.0641
10.0	342.24	104.32	0.0184	0.0602
10.5	362.68	110.54	0.0173	0.0568
11.0	382.96	116.73	0.0164	0.0538
11.5	403.12	122.87	0.0156	0.0511
12.0	423.17	128.98	0.0148	0.0487

# 4 Wave Environment

---

## Processing Algorithms

Incident waves were measured with a Datawell Directional Waverider buoy, located approximately 457 m (1,500 ft) in front of the RIBS XM99. This incident wave data was processed with three different algorithms. These included the Datawell on-board buoy processing, a GEDAP (software package) single channel frequency analysis, and a Maximum Likelihood Method (MLM) directional spectral analysis.

### Datawell analysis

For the Datawell directional buoy, the directional wave spectra are estimated based on translational motions instead of wave slopes. The buoy contains a heave-pitch-roll sensor, a three-axis compass, and two x- and y-axis accelerometers. The three accelerations for heave and the two horizontal components are digitally integrated to get filtered displacements in the vertical, north, and west directions. Analog outputs of the accelerometers are low pass filtered with a cutoff frequency of 1.5 Hz, resampled at 3.84 Hz, and low-pass filtered again with a 10<sup>th</sup> order filter with a cutoff of 0.6Hz. The Datawell algorithm calculates the Fast Fourier Transform (FFT) every half hour from eight overlapping segments of 200 sec of data. The final record length is 1,535 points or 1,200 sec (i.e., 20 minutes). The number of degrees of freedom is 16, at a sampling frequency of 1.28 Hz (i.e.,  $\Delta t = 0.781$  sec).

### GEDAP analysis

GEDAP is a general purpose software package for control signal generation, time and frequency domain analyses, and data manipulation, archival, and presentation. It was originally developed by the National Research Council of Canada Hydraulics Laboratory. It is a modular package that is fully integrated by a common file and support structure and an interactive graphics package.

The GEDAP program “VSD” was used to estimate the variance spectral density by smoothing the modified periodogram of the total record. The

modified periodogram was obtained by multiplying the record by a 10 percent cosine bell window on the data to reduce leakage. Cutoff frequencies of 0.0 and the Nyquist frequency of 0.64 Hz (i.e., half of the sampling frequency) were used. The filter or equivalent bandwidth was 0.01 Hz giving 20 degrees of freedom.

### MLM directional spectral analysis

For the MLM analysis, a Matlab version of the standard multidirectional spectral analysis software for the directional spectral wave generator was used. The data were zero-meaned, tapered by a 10 percent cosine bell window, and Fourier transformed to the frequency domain. The spectral and cross-spectral estimates were Gaussian smoothed with an effective bandwidth of 0.01 Hz. A wrapped normal directional spreading function was used as an initial estimate and an MLM algorithm was used to improve this initial estimate. The overall mean wave direction and mean directional spreading were calculated according to the International Association of Hydraulic Engineering and Research (IAHR) List of Sea State Parameters (1997) for multidirectional waves.

## Wave Parameters

### Time series

**Significant wave height.** Significant wave heights from the GEDAP and Datawell analyses are compared in Figure 7. The MLM values are slightly smaller than these two and are not shown. Figure 8 shows the significant and maximum wave heights from the GEDAP analysis. The dashed lines represent the lower limits of the sea state 3 (SS3) and sea state 4 (SS4) wave environments. The blank spaces are due to breaks in the data. In general, the GEDAP values are higher than the Datawell, but have the same shapes and trends. During the deployment, significant wave heights were less than SS3, except for periods on May 22 and May 29. Maximum wave heights (Figure 8) exceeded the SS3 lower limit on many occasions, however.

**Significant wave periods.** Significant wave periods from the GEDAP and Datawell analyses are shown in Figure 9. Figure 10 is the GEDAP analysis of the significant and maximum wave periods. This maximum wave period corresponds to the period of the maximum wave height, and does not necessarily imply a larger value than the significant wave period. The large fluctuations are due to the multi-modal character of the wave environment. The deployment period was characterized by unimodal sea only and swell only, and combined bimodal, and even trimodal, sea and swell wave spectra. Thus, the large variations in wave period are due to the shifting in wave energy between sea and swell peaks. In general, the GEDAP and MLM (not shown) values tend to track each other better, showing both sea and swell peaks. The Datawell values tend to track the sea peaks only.

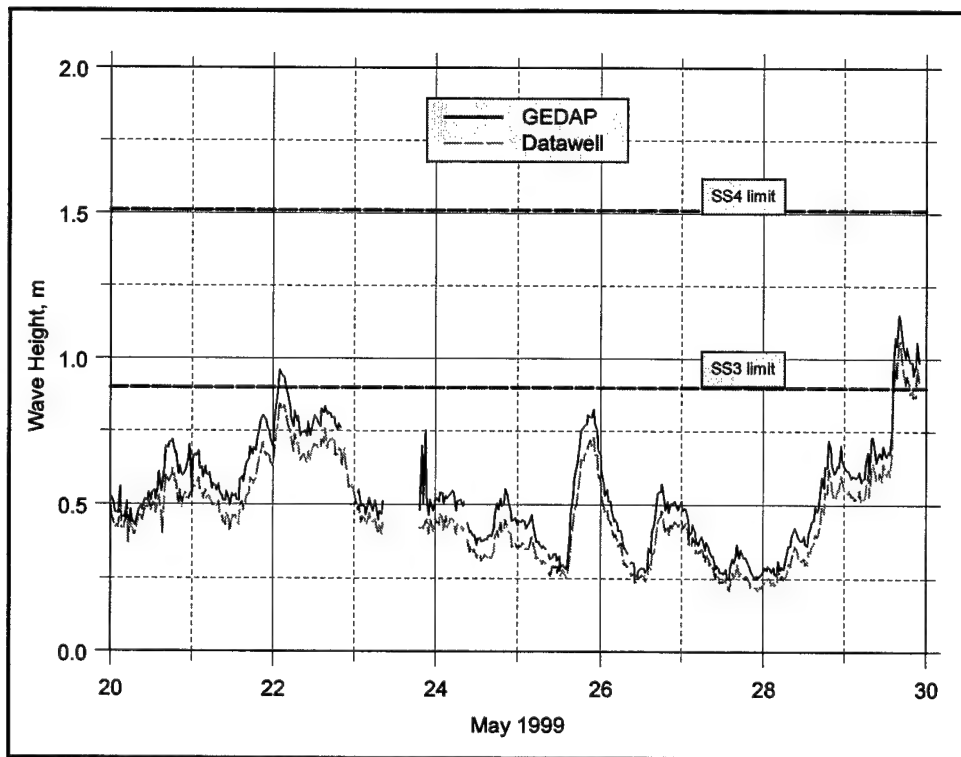


Figure 7. Incident significant wave heights

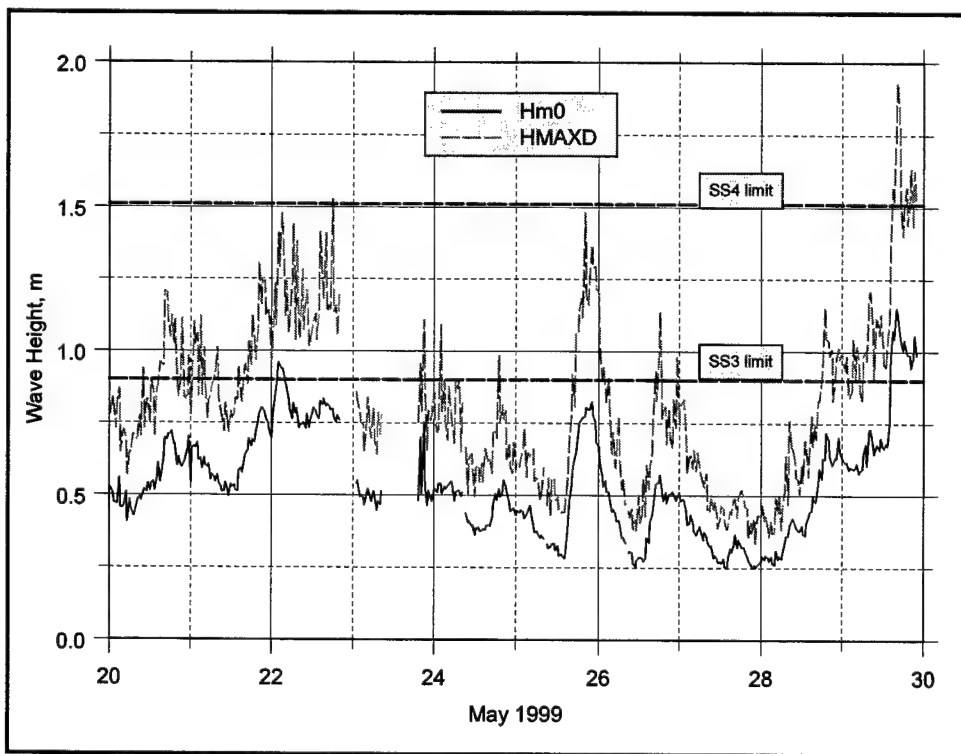


Figure 8. GEDAP significant and maximum wave heights

**Table 3**  
**Short, Missing, Bad, and Edited Wave Data**

Date	Short Data	Missing or Bad Data		Edited Data	
	Directional	Directional	Nondirectional	Directional	Nondirectional
May 20	0500	0000, 1530	0000 - 1340	0530, 2230, 2300, 2330	
May 21	1130			0000, 0030, 0130, 0330, 0500, 0530, 0830 - 1000, 1130, 2000	1520, 1700
May 22		2030 - 2330	0000 - 0740	0000, 0530, 1000 - 1130, 1400	1920
May 23		0900 - 1900		0000, 0100, 0300, 0330, 0530, 2000	
May 24	1600	0900	0000 - 0840	0530	
May 25	1700	0830		0730, 0900, 1430, 1630	1600, 2040
May 26		0830	0000 - 0740	0530	
May 27				0700, 0800, 0900, 1400, 1500 - 1630	
May 28			0000 - 0940	1300, 1800	1640, 1720, 2000, 2040
May 29		2230 - 2330		0700, 1430	1020, 1100
May 30	1000	0000, 0100, 0200, 0300	All	0230, 0330, 1100, 1230, 1330, 1400	

Note: Nondirectional data recorded every 20 min. Directional data collected every half hour.

**Mean wave direction and spreading.** Figure 11 is a time series of mean wave direction and directional spread at the peak frequency from the MLM analysis. The dashed line at 255 deg is the lower limit on the range of effective wave directions for the RIBS XM99. Most of the mean wave directions were within this window. The optimum “design” condition, with waves in the vicinity (i.e.,  $\pm 15$  deg) of 315 deg, occurred for several hours between May 24 and May 27. Directional spreading ranged from 30 to 80 deg, the former value representative of a more narrow directional spreading.

### Directional spectral plots

Figures 12 and 13 are typical plots from the MLM directional spectral analysis. The upper panel of Figure 12 shows the frequency spectrum and the lower panel illustrates the integrated directional spectra and the spreading function at the peak frequency. The directional spectra is obtained by summing the energy at each wave direction over all frequencies. Figure 13 contains a contour and three-dimensional plot of the directional wave spectra from the MLM analysis.

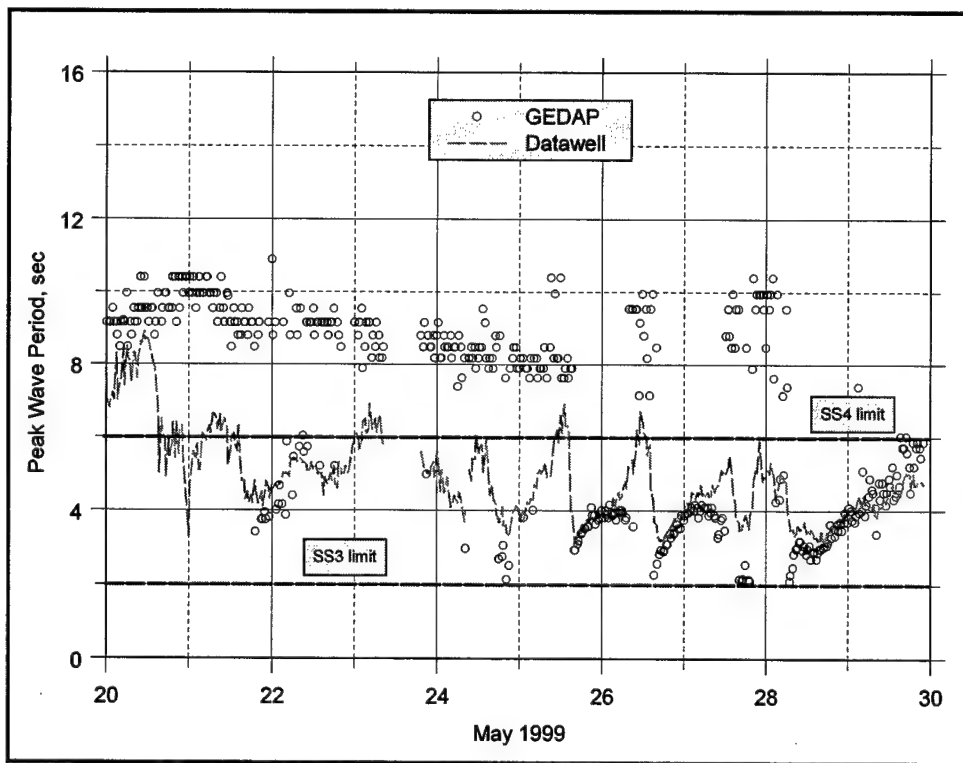


Figure 9. Incident wave periods

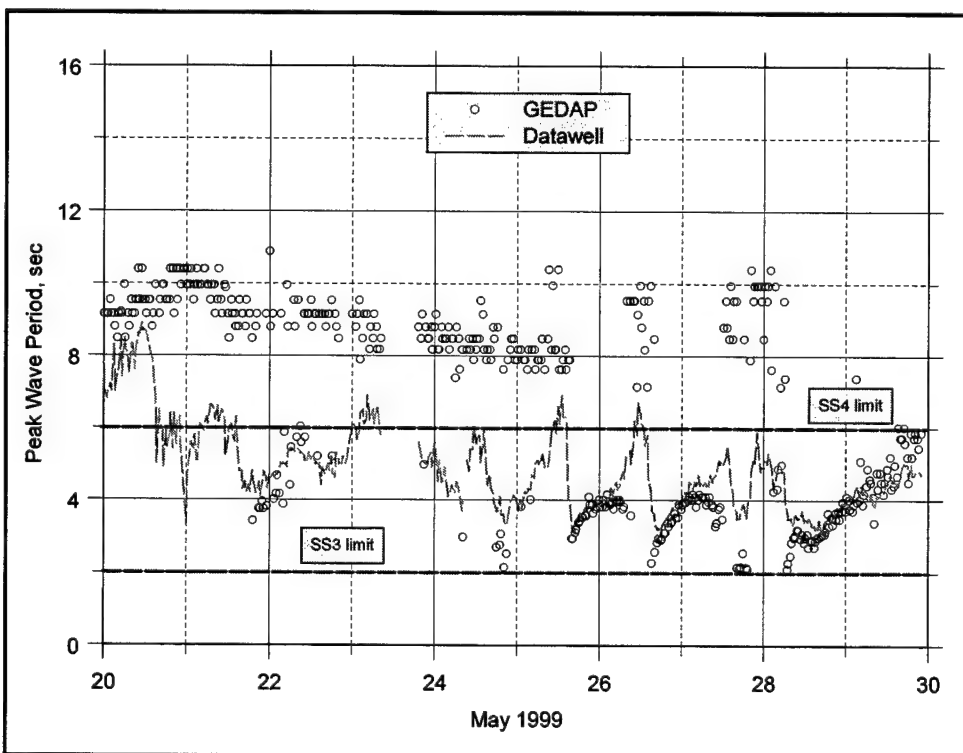


Figure 10. GEDAP significant and maximum wave periods

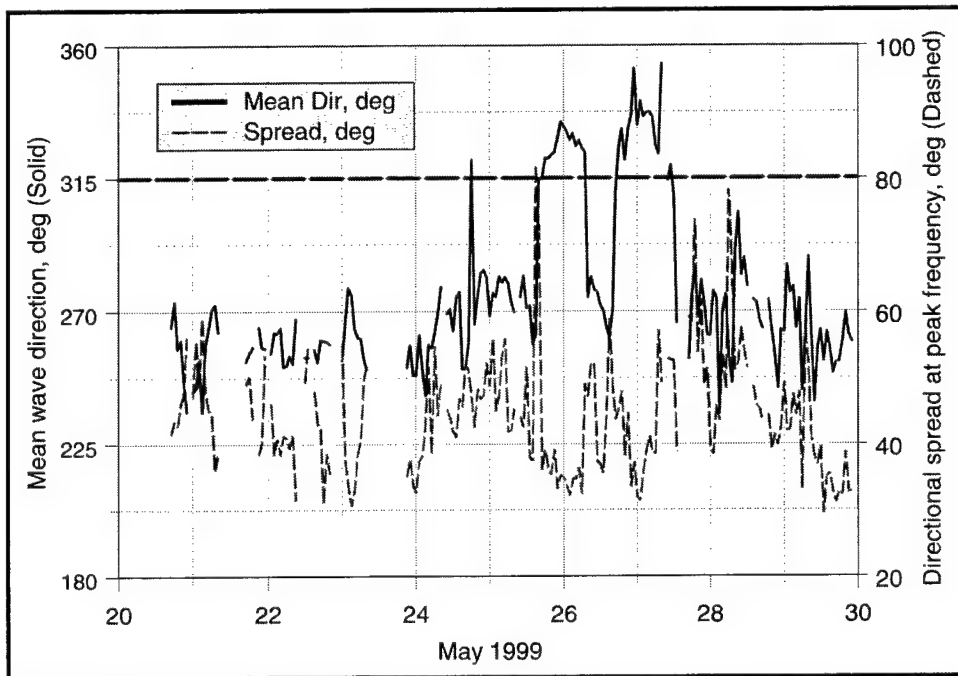


Figure 11. MLM incident wave direction and directional spread

Both figures are for the unimodal sea spectra for May 25, 1800 hours, with a peak period of 3.3 sec, significant wave height of 60 cm, mean wave direction of 322 deg, and directional spreading of 39 deg.

Figures 14 to 16 are typical contour and three-dimensional plots of the directional wave spectra for various unimodal and bimodal spectra. Figure 14 is an example of a unimodal swell spectrum for May 23, 600 hours, with a peak period of 8.3 sec, wave height of 40 cm, wave direction of 261 deg, and spread of 40 deg. A bimodal spectrum with a dominant sea mode for May 24, 1800 hours, is shown in Figure 15. The peak period is 2.7 sec, with a height of 41 cm, direction of 321 deg, and spread of 47 deg. Finally, a bimodal spectrum with a dominant swell mode (i.e., lower frequency peak) for May 21, 1800 hours, is shown in Figure 16. The peak period is 9.1 sec, with a height of 55 cm, direction of 256 deg, and spread of 50 deg. Additional interesting wave cases are listed in Table 4.

### Joint distribution plots

Joint distribution plots of significant wave height, mean wave direction, and directional spread versus peak wave period from the GEDAP analysis are shown in Figures 17 to 19, respectively. Figure 17 is the joint distribution for wave period and height. It shows that the wave data split nicely into sea and swell categories. The sea conditions are also representative of the SS3 and smaller conditions with wave periods less than 6 sec. The swell conditions have peak periods greater than 6 sec. The largest recorded significant wave height was

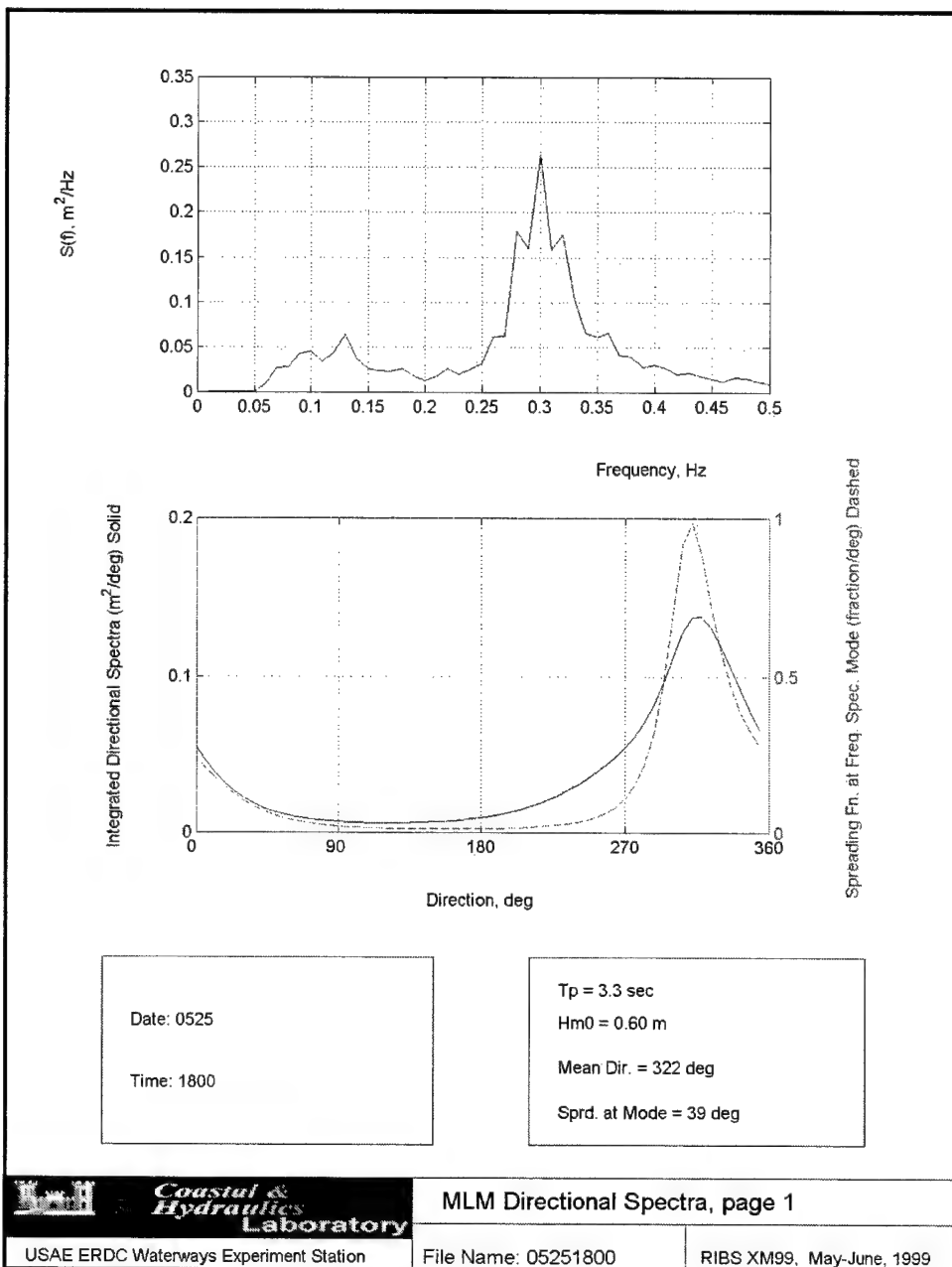


Figure 12. Frequency spectrum and directional spreading, unimodal sea

1.15 m at a peak wave period of 4.71 sec. The largest peak period was 10.9 sec at a significant wave height of 0.70 m.

Figure 18 is the joint distribution of mean wave direction and peak wave period from the MLM analysis. As expected, wave directions are more tightly grouped in the swell waves (i.e., periods greater than 7 sec) than the sea waves. The lower limit at 255 deg indicates that most of the waves encountered during the XM99 deployment were within the window of allowable wave directions for effective performance. The largest wave direction was at 354 deg with a wave

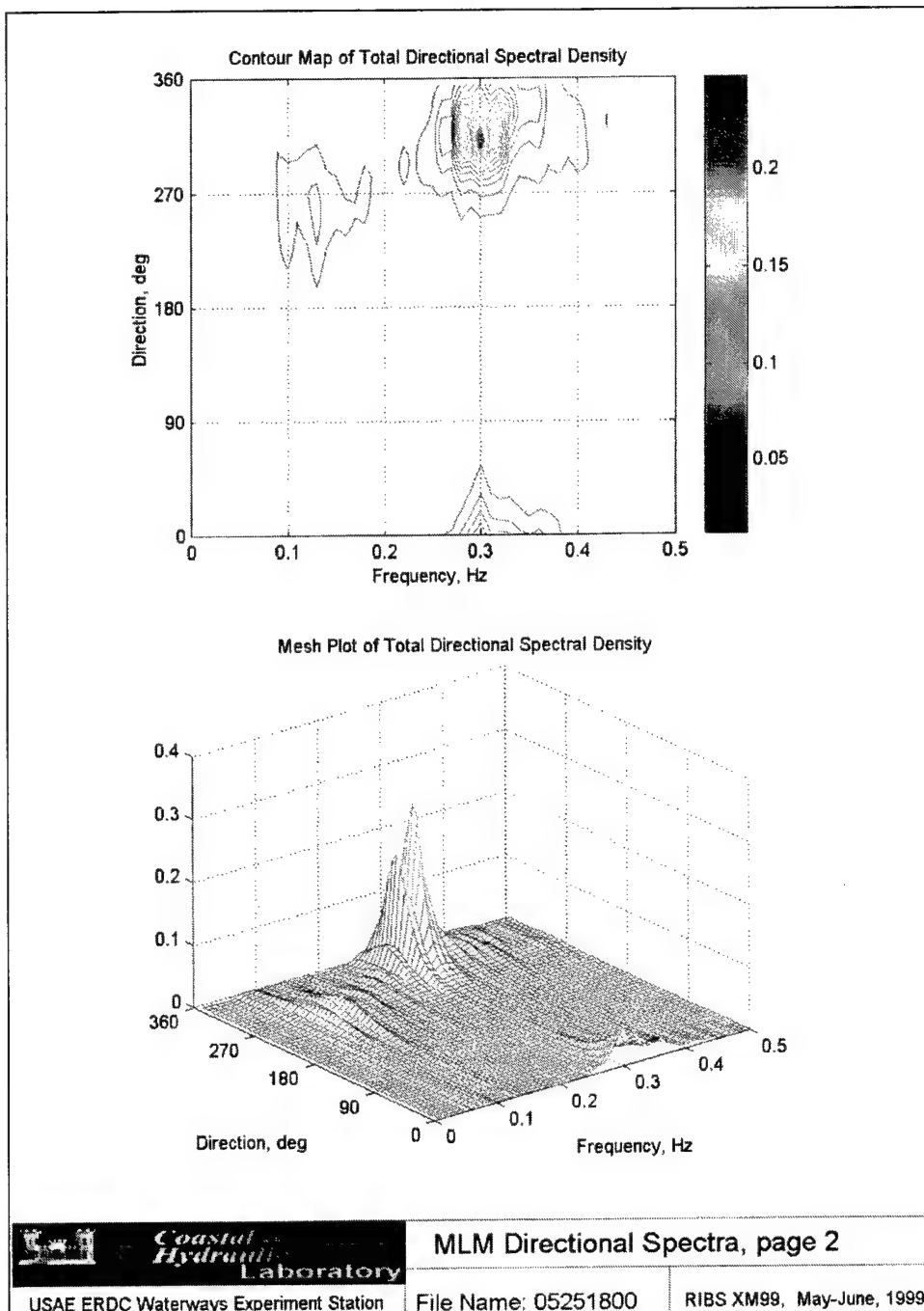


Figure 13. Directional wave spectrum, unimodal sea

period of 3.94 sec. The smallest wave direction of 236 deg occurred at wave periods of both 4.23 and 10.39 sec. Waves with mean wave directions within  $\pm 15$  deg of 315 deg occurred 22 times with wave periods ranging from 2.7 to 4.2 sec. These waves are probably all within the “design” direction window for the XM99 of 315 deg, parallel to the its center line. Three occurrences were at 315 deg.

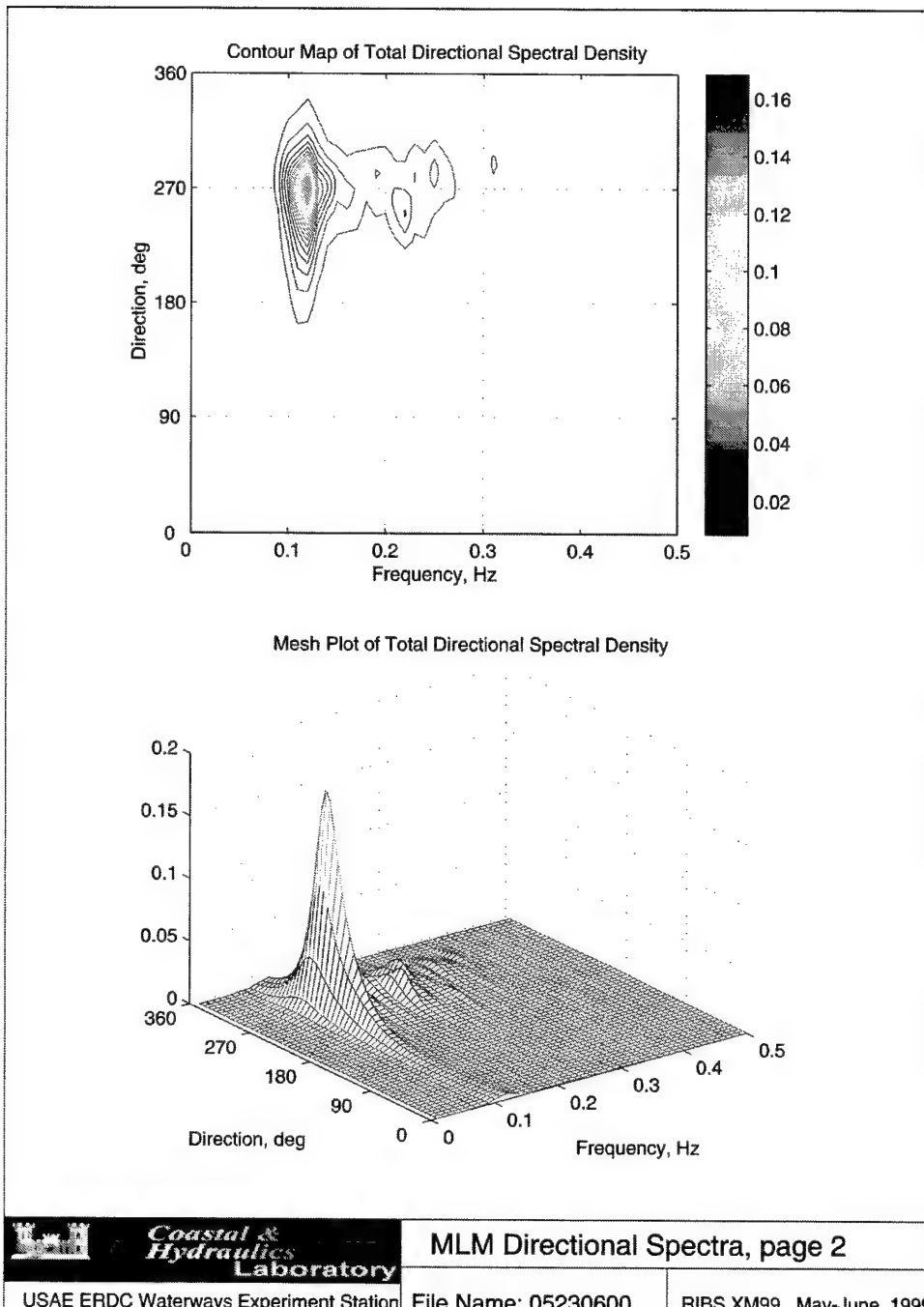


Figure 14. Directional wave spectrum, unimodal swell

Figure 19 is the joint distribution for directional spread and peak wave period. Most of the spread values are between 30 and 60 deg. The maximum spread of 82 deg occurs with a peak period of 7.9 sec. Some of the larger values above 60 deg may be spurious points. The minimum value is 29.5 deg at 4.2 sec. Values of 30 to 50 deg are representative of fairly narrow spreading. In general, swell waves would be more narrow than sea conditions.

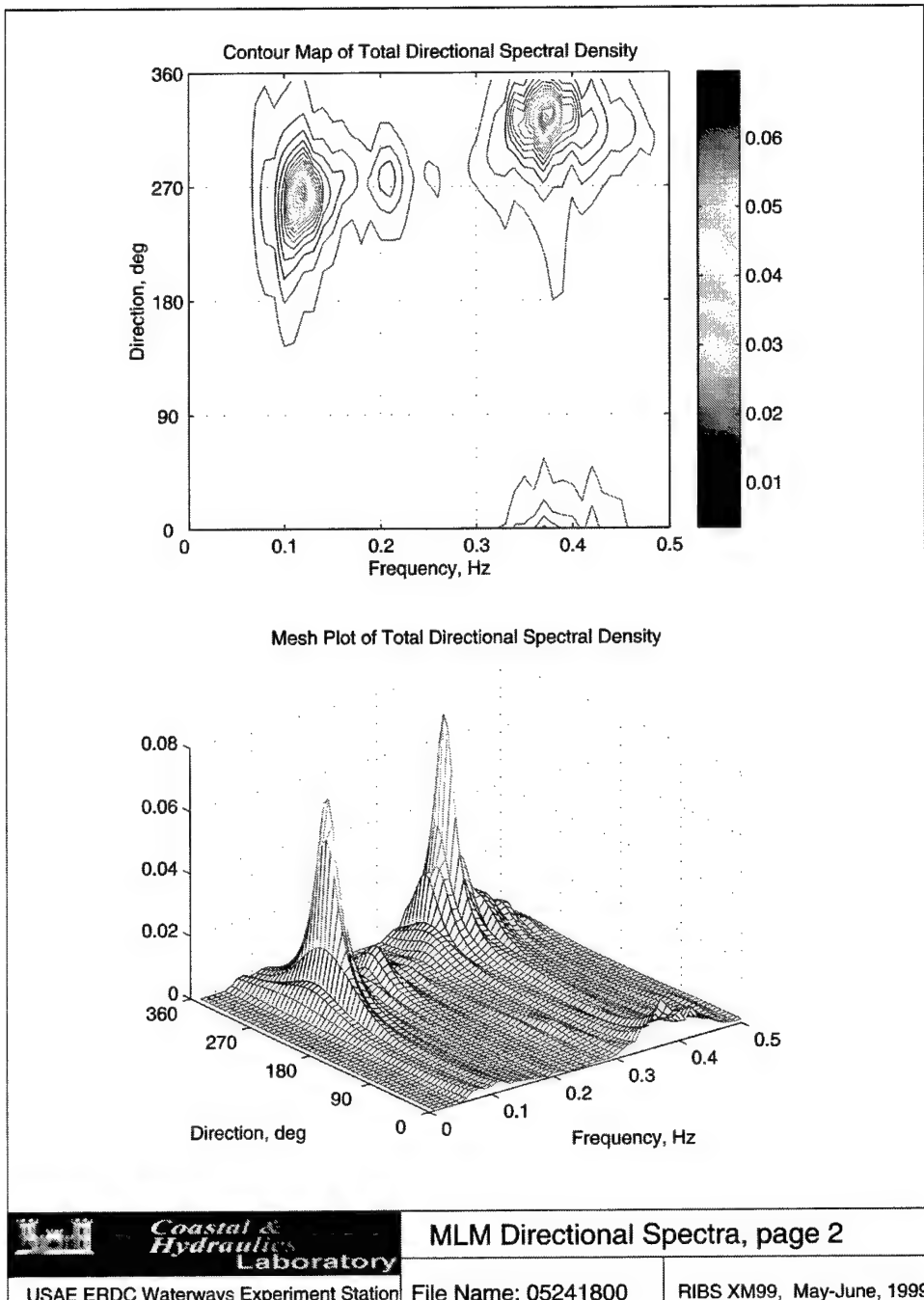


Figure 15. Directional wave spectrum, bimodal with dominant sea mode

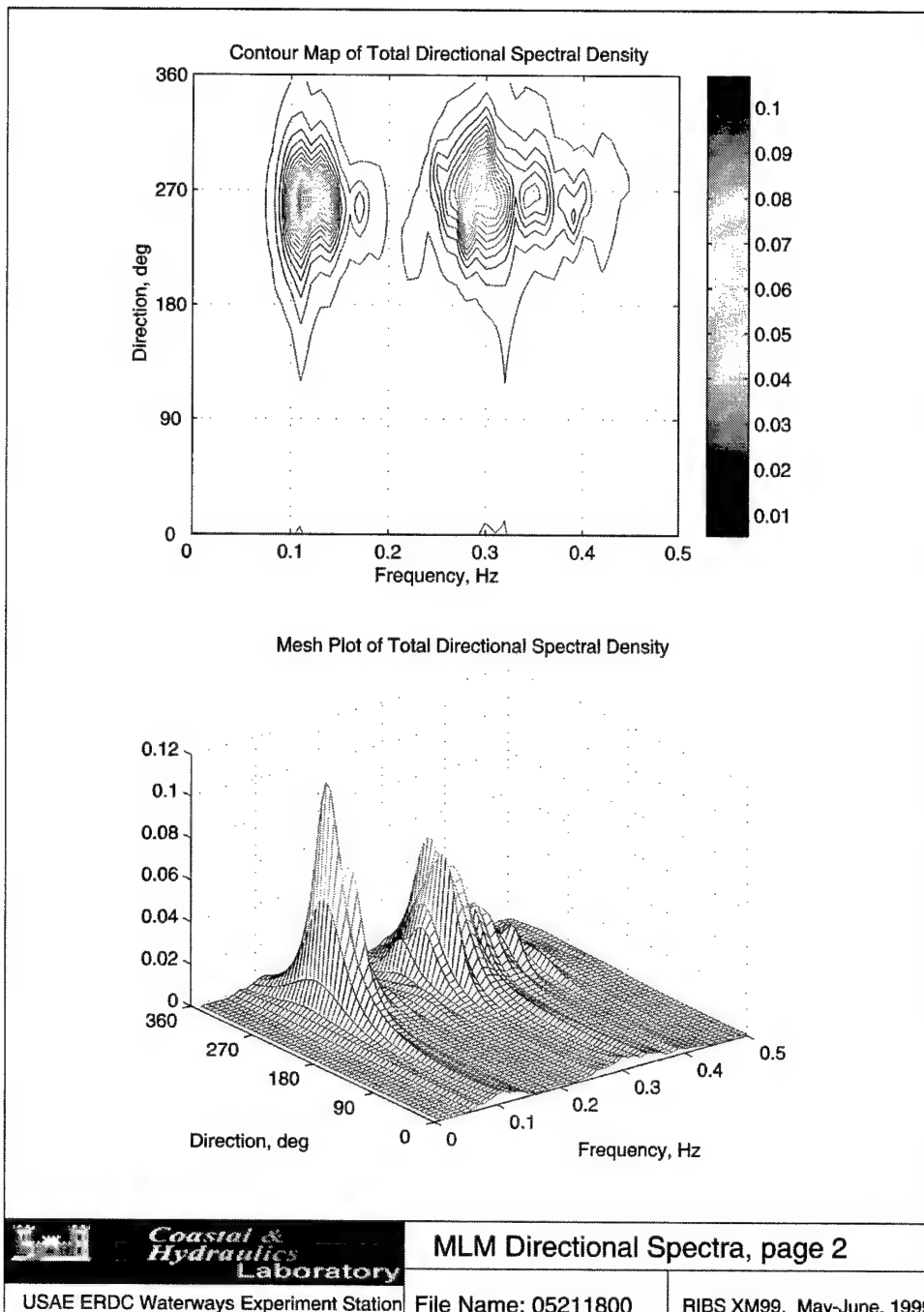


Figure 16. Directional wave spectrum, bimodal with dominant swell mode

**Table 4**  
**Interesting Wave Conditions**

Date	Time	Period, sec	Height, m	Direction, deg	Spread, deg
May 21	1800	3.75	0.80	265	38
May 22	1200	9.52	0.79	254	49
	1500	9.14	0.81	257	48
	1800	9.52	0.80	260	31
May 23	0600	8.47	0.51	261	40
	1800				
	2100	4.97	0.75	251	35
May 24	1800	2.69	0.50	321	47
May 25	1800	3.36	0.72	322	39

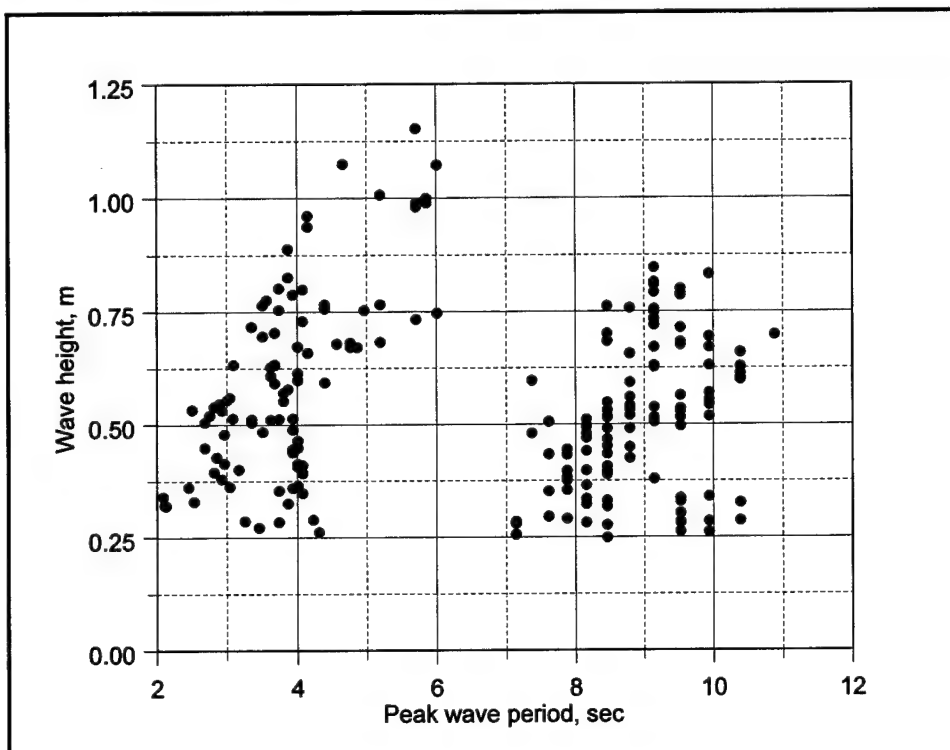


Figure 17. Joint distribution of wave period and height

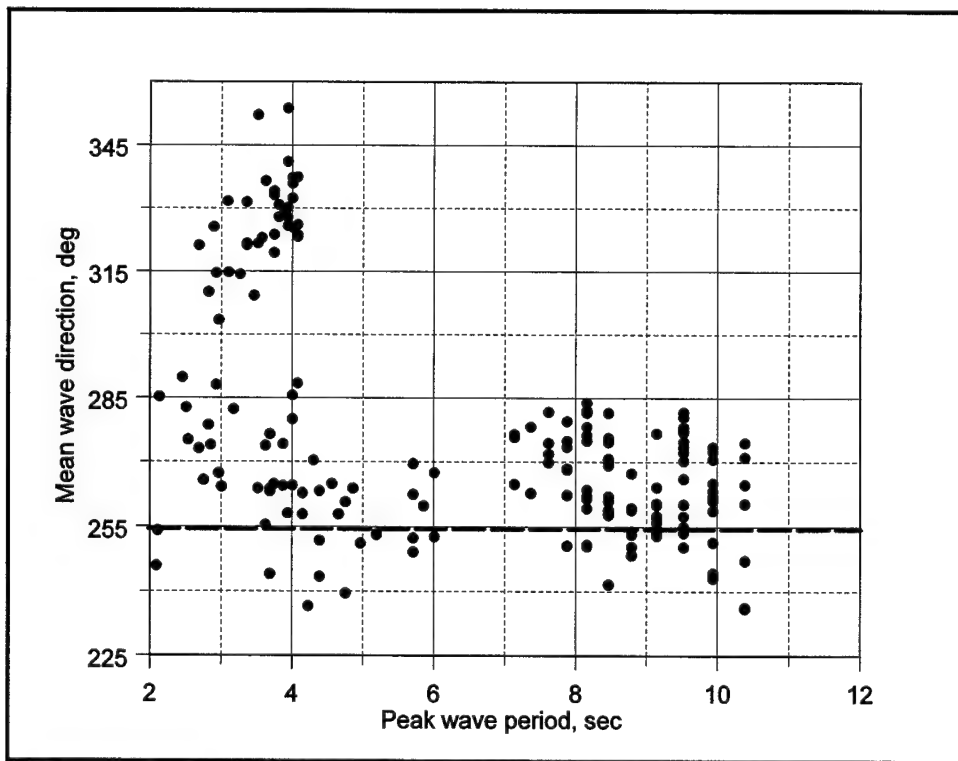


Figure 18. Joint distribution of wave period and wave direction

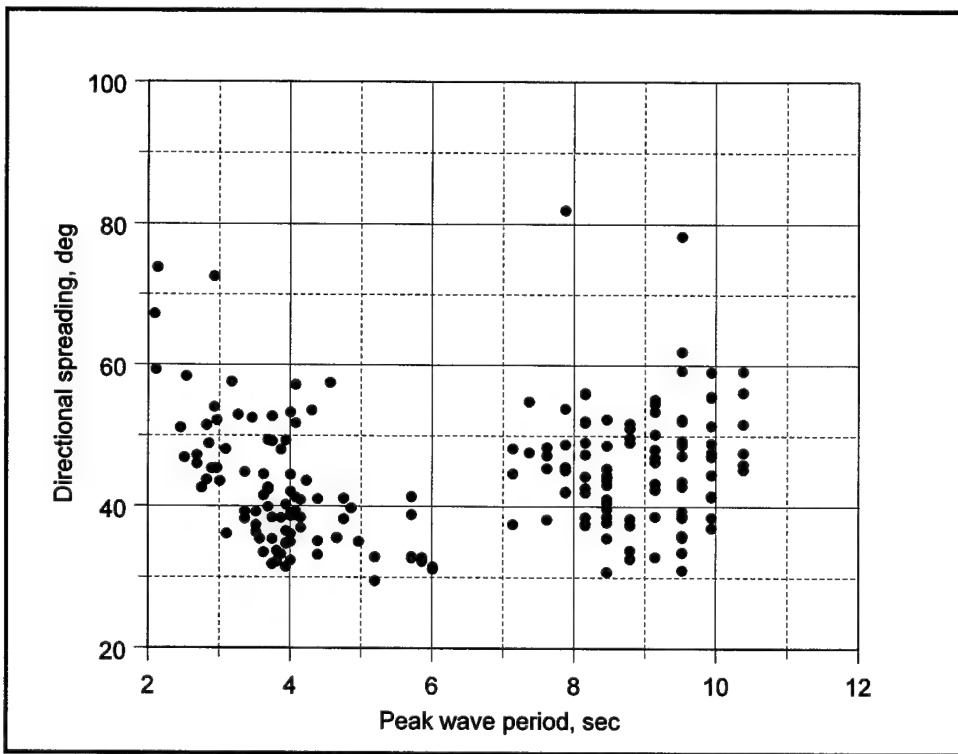


Figure 19. Joint distribution of wave period and directional spread

# 5 Field Measurements

---

## Transmission Coefficients

The transmission coefficient presented in Equation 1 is an overall value of the wave transmission for the entire wave field. It is based on the zero moment wave height  $H_{m0}$  given by

$$H_{m0} = 4\sqrt{m_0} \quad (42)$$

where the zeroth moment  $m_0$

$$m_0 = \sum S(f) \Delta f \quad (43)$$

is the sum over all frequencies of the spectral density estimates. A frequency-dependent transmission coefficient  $K_T(f)$  can be defined as

$$K_T(f) = \frac{H_r(f)}{H_i(f)} = \sqrt{\frac{S_r(f)}{S_i(f)}} \quad (44)$$

where the  $H_{m0}$  wave height is used and  $S_r(f)$  and  $S_i(f)$  are the transmitted and incident wave spectral estimates at frequency  $f$ , respectively. The incident values are measured from the Datawell directional buoy. Because of the distance from this buoy to RIBS (i.e., 457 m), it is assumed that these spectral estimates do not include any reflected energy from RIBS.

The total wave transmission coefficient may be defined as a weighted average of the frequency-dependent wave transmission coefficient

$$K_T = \sum_{f_l}^{f_u} Wgt(f) K_T(f) \quad (45)$$

where  $f_l$  and  $f_u$  are lower and upper frequency limits, respectively. These cutoff limits can be selected to cover the entire frequency range, a range enclosing

some percentage of the total energy, or some other range. The weighting function can be a constant, as in  $1/N$  to give a simple average, or an energy-based value given by

$$Wgt(f) = \frac{S_I(f)\Delta f}{m_0} \quad (46)$$

where  $S_I(f)$  is the measured spectral density and  $m_0$  is the zeroth moment of the incident wave.

## Wave Pressures

Wave pressures were measured at twelve external and five internal locations on the port leg of the RIBS XM99. On the external side, gages were located at three stations on each of four vertical levels. The three stations are bow, middle, and stern. The four levels are the surface, top, middle, and bottom. The five gages on the internal side were located on the top, middle, and bottom levels at the middle and stern stations. There was no stern station gage on the bottom level, however. Table 5 is a schematic of the pressure gage locations and codes for the external and internal gages. The origin of a local coordinate system for positioning the instrumentation was located in the center of the top deck, at the stern end of the port leg. Positive x-axis pointed to the bow, positive y-axis to the center of the RIBS, and positive z-axis up. Table 6 lists the coordinates for these gages in this local coordinate system.

**Table 5**  
**Pressure Gage Codes**

Level	Station Location		
	Bow	Middle	Stern
<b>Reference Gages</b>			
Surface	511	507	503
<b>External Gages</b>			
Top	512	508	504
Middle	513	509	505
Bottom	514	510	506
<b>Internal Gages</b>			
Top	—	564	561
Middle	—	575	562
Bottom	—	576	—

**Table 6**  
**Pressure Gage Coordinates**

Level	Station Location								
	Bow			Middle			Stern		
	x (m)	y (m)	z (m)	x (m)	y (m)	z (m)	x (m)	y (m)	z (m)
<b>Reference Gages</b>									
Surface	67.71	0.00	0.38	35.16	0.00	0.38	1.20	0.00	0.38
<b>External Gages</b>									
Top	67.71	0.00	-3.11	35.16	0.00	-3.11	1.20	0.00	-3.11
Middle	67.71	0.00	-4.79	35.16	0.00	-4.79	1.20	0.00	-4.79
Bottom	67.71	0.00	-7.08	35.16	0.00	-7.08	1.20	0.00	-7.08
<b>Internal Gages</b>									
Top	-	-	-	35.16	2.71	-3.11	1.20	2.71	-3.11
Middle	-	-	-	35.16	2.71	-4.79	1.20	2.71	-4.79
Bottom	-	-	-	35.16	2.71	-7.08	--	--	--

Data were collected at a sampling rate of 4 Hz for the first 30 minutes of every hour and transferred to the receiving computer during the second half hour. A total of 7,200 points were collected for each 30-min record. These data were analyzed with the GEDAP software package. The procedure is described in the following paragraphs. It is understood that each of the pressure quantities is a time series, but that the relationship as a function of time (i.e., “(*t*”)) is not shown.

The three surface pressure gages were reference gages to measure atmospheric pressure. The submerged pressure gages measured absolute pressure  $p_{abs}$  that included the local atmospheric pressure  $p_{atm}$ . Therefore, the first step in the analysis procedure involved the estimation of the atmospheric pressure from the three surface gages. An average value for all three reference gages was calculated. This average value of the atmospheric pressure  $p_{atm}$  was then subtracted from the absolute pressure to obtain the gage pressure  $p_{gage}$  for each gage

$$p_{gage} = p_{abs} - \bar{p}_{atm} \quad (47)$$

The second step in the procedure involved the estimation of the gage depths for the pressure gages. This depth is a function of the hydrostatic component of pressure  $p_{static}$ . Since this value is a constant for each pressure gage, it can be estimated by finding the mean or average of each gage. The gage depth is obtained by converting  $p_{static}$  into an equivalent water depth (i.e., 50.9 kP/m (2.25 psi/ft) of water).

The third step in the analysis is to zero-mean the time series by subtracting  $p_{static}$  to obtain the dynamic pressure  $p_{dyn}$

$$p_{dyn} = p_{gage} - p_{static} \quad (48)$$

where the gage pressure  $p_{gage}$  is the same as the total wave pressure  $p_{tot}$  from Equation 17. The time series records for each of the external and internal pressure gages now consisted of only the dynamic wave pressure component.

The fourth step in the data processing was to calculate the net pressure  $p_{net}$  at each of the five locations where both external and internal gages were available. It was calculated by subtracting the internal pressure gage  $p_{int}$  from the external pressure gage  $p_{ext}$

$$p_{net} = p_{ext} - p_{int} \quad (49)$$

The final step in the procedure consisted of calculating time and frequency domain parameters from the time series for external, internal, and net pressures. In the time domain, a zero down-crossing analysis was performed. Calculated statistics included the minimum and maximum pressures, RMS pressure, significant pressure height and associated period, and maximum pressure height. In the frequency domain, a standard spectral analysis routine was used on the pressure data. This consisted of a 10 percent cosine bell window, variance restoration, and a frequency bandwidth of 0.01 Hz between zero and the Nyquist frequency at 2.0 Hz to obtain 16 DOF spectral estimates. Frequency domain parameters included a zero-moment pressure and peak period from the pressure spectrum. Each of these values was saved to a file for archival and subsequent processing and analysis.

# 6 Results and Discussion

---

In this chapter, measured and predicted transmission coefficients and dynamic pressures are compared. The unimodal sea spectrum of May 25, 1800 hours is used as an example.

## Transmission Coefficients

Figure 20 is from the wave transmission analysis for the measured data discussed in the previous chapter. The middle panel shows incident and transmitted wave spectra. The upper panel gives the transmission coefficient  $K_T(f)$  as a function of frequency. The horizontal dashed line is the desired cutoff for wave transmission at  $K_T = 0.5$ . The vertical dashed line is at a frequency of 0.17 Hz (i.e., 6 sec), corresponding to an upper limit of SS3. The lower panel is a summary table of the calculations for the transmission coefficient. Minimum and maximum values, the average, and 90 percent confidence limits are shown for the entire frequency band and the limited or short band of frequencies greater than 0.17 Hz. The averages are simple averages over the values of  $K_T$ . For the short frequency band from 0.17 to 0.5 Hz, the average  $K_{T, \text{SS3}} = 0.37$ . This compares to the value of  $K_{T, \text{Ave}} = 0.51$  for the entire frequency band from 0 to 0.5 Hz.

The reader should not be alarmed by the values of the transmission coefficient greater than 1.0 in the low frequencies. The relative amount of energy in these low frequencies is so small that the amount of wave amplification would not be noticed by an observer on a ship. Also, the energy values at these frequencies are so small that they may be heavily influenced by signal noise and not actually as large as these calculations indicate they may be. This is part of the justification for using an energy-based weighting function for the estimation of the wave transmission coefficient as these seemingly large amplifications would not be present if the  $K_T$  were weighted this way. Future research with wave transmission coefficients will examine energy-based weighting functions.

Figure 21 is a time series of wave transmission values during the 10 days of deployment. The solid curve is the traditional definition of the wave transmission coefficient, the ratio of transmitted wave height to incident wave height (Equation 1). The dashed curve (i.e.,  $T < 6$  s) is the simple average from the reduced or short frequency band of frequencies greater than 0.17 Hz. The

07 February 2001 13:21

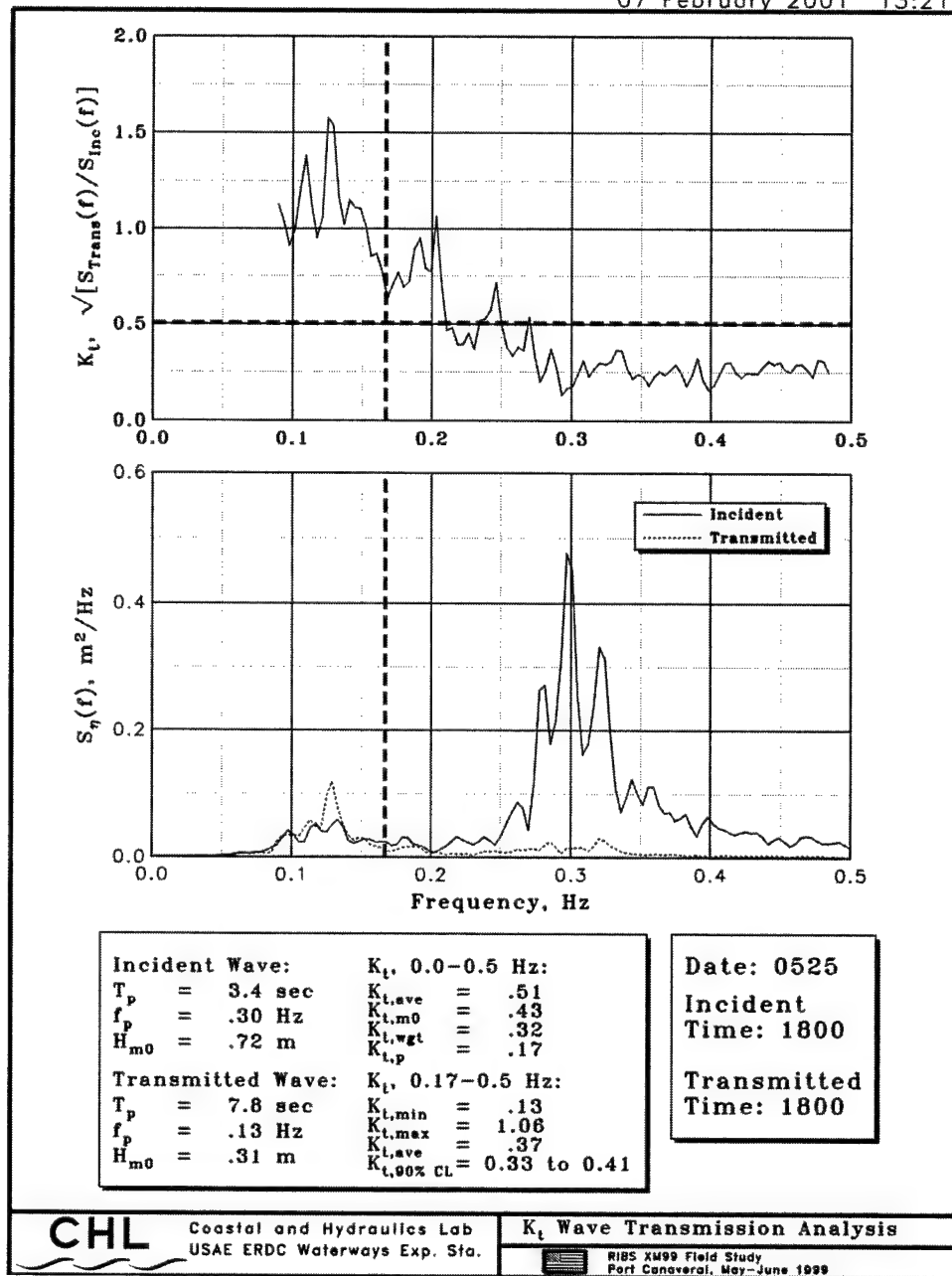


Figure 20. Wave transmission coefficient analysis by frequency

reduced frequency band values are usually less than the full band, with the amount of difference being a function of wave period and direction. Values for the full band range from  $K_t = 0.3$  to  $1.00$ . The short frequency band values range from  $K_{t,SAve} = 0.25$  to  $0.9$ . Wave transmission coefficients are less than the  $K_t = 0.5$  desired level of efficiency (i.e., dashed line) for several hours every day, with the best performances on May 22, 23, 25, 26, and 28.

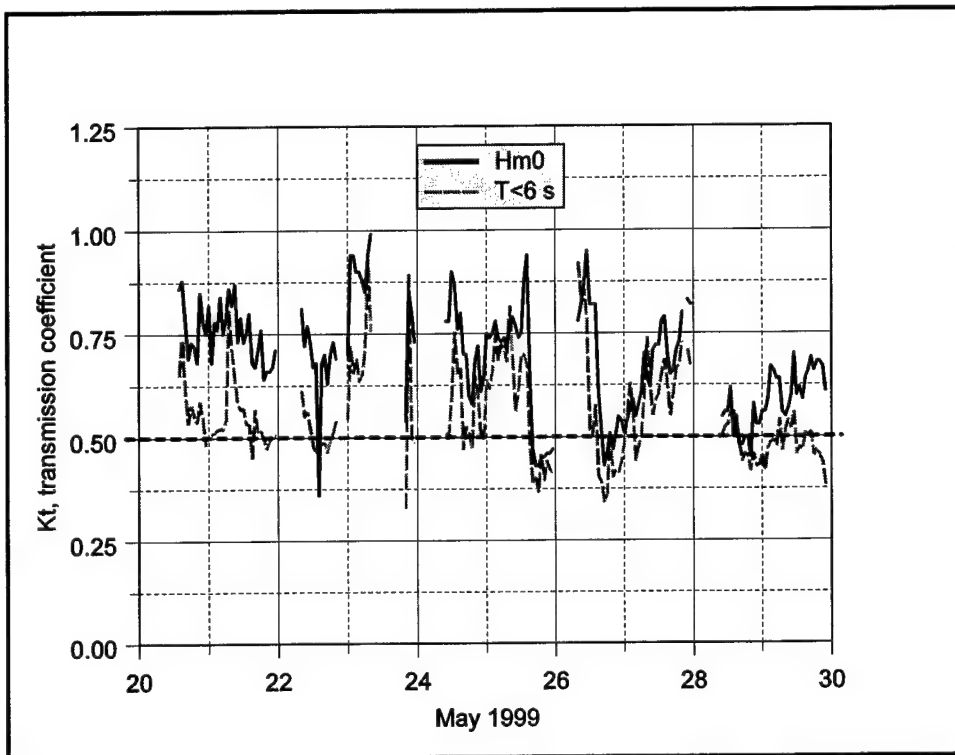


Figure 21. Wave transmission coefficients

Joint distribution plots of wave transmission coefficient and peak wave period are shown in Figures 22 and 23 for the full band and short band of frequencies, respectively. Wave transmission values group into either sea or swell regimes depending on whether the dominant mode of the waves is in the sea or swell band of frequencies. For the traditional  $K_T$  shown in Figure 22, wave transmission is less than the threshold value  $K_T = 0.5$  on 17 occasions for the sea conditions. There are no occurrences less than the threshold for the predominantly swell wave conditions. For the  $K_{T,SAve}$  for the short range of frequencies shown in Figure 23, however, there are a large number of wave transmission values less than the threshold for both sea and swell conditions.

The peak wave period in these figures can be for a unimodal sea or swell, or a dominant sea or swell mode of a bimodal or multimodal sea state. Wave transmission values in Figure 22 are based on the full range of frequencies from 0 to 0.5 Hz, which include both sea and swell frequencies. Since the RIBS XM99 was not designed for swell waves, only unimodal sea waves will have wave transmission less than the threshold. For the short range of frequencies calculation method for wave transmission shown in Figure 23, however, it is possible to have values less than the threshold for both sea and swell waves. This is because the method begins at a frequency of 0.17 Hz, effectively eliminating the swell range of frequencies. Thus, bimodal or multimodal waves will have their contribution to the transmission coefficient from the swell mode eliminated and the overall value reduced. For those wave cases with dominant sea modes, the secondary swell mode may have been nearly equal in energy and contributing

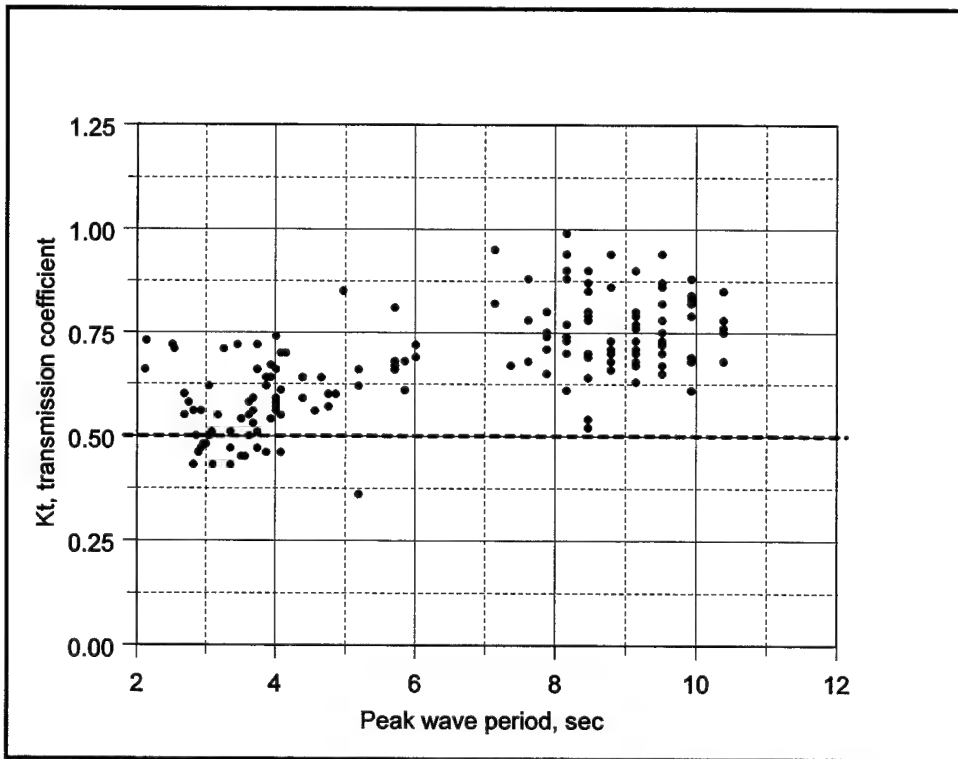


Figure 22. Joint distribution of wave period and wave transmission based on zero moment wave height

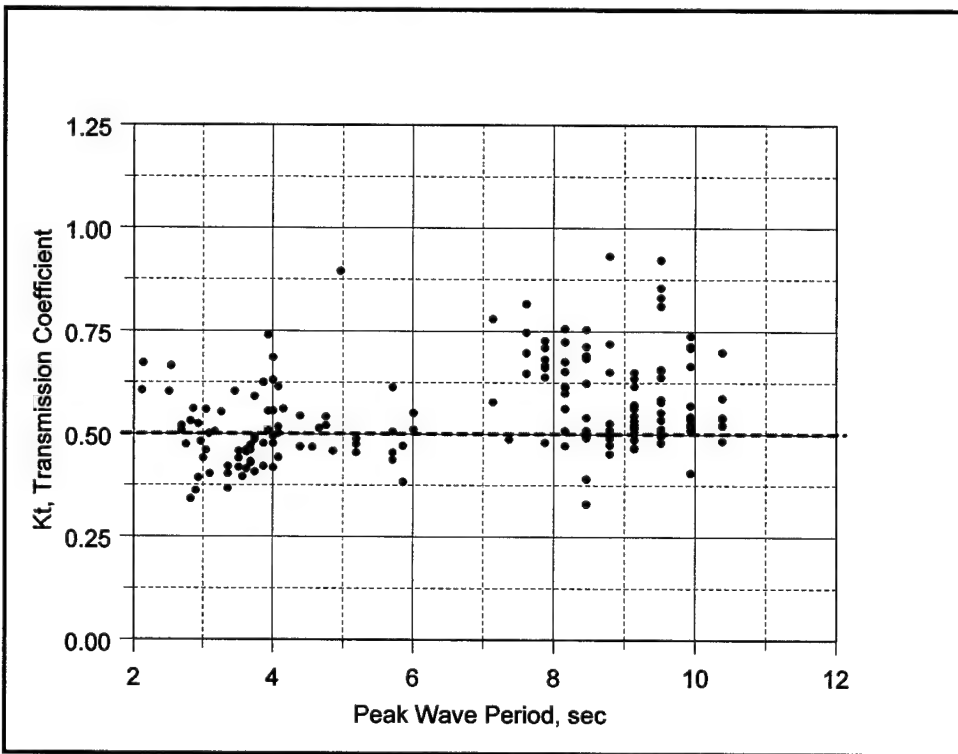


Figure 23. Joint distribution of wave period and wave transmission based on simple average for short range of frequencies

substantially to the overall wave transmission. The elimination of this swell mode results in the increase in the number of occurrences below the threshold level. Similarly, for the dominant swell mode cases (i.e., wave periods greater than 7 sec), the elimination of the primary swell mode leaves the contribution to the wave transmission coming from the secondary sea mode. The relative amount of energy in this secondary sea mode to the primary swell mode determines how much the wave transmission is reduced. The 21 values below the threshold for the swell conditions are probably from secondary sea modes that had a substantial portion of energy relative to the primary swell mode. The cases of wave transmission above the threshold are probably determined by wave direction and directional spreading exceeding the range of allowable directions for the RIBS XM99.

Figure 24 compares the wave transmission coefficients from the WAMIT model and the field measurement for the example case. The curve is for the WAMIT prediction along the center line of the RIBS XM99. In general, the  $K_T$  oscillates along the center line of the XM99, with values ranging from 0.03 to 0.4. The transmitted gage appears to have been located at the point of an anti-node for this wave period and direction. The agreement is very good, if the  $K_{T,Ave} = 0.37$  value from the reduced frequency band is used.

Of course, one should realize that the field measurement is for one location. Although it is assumed to be fixed, in reality the transmitted wave buoy probably undergoes some movement about a watch circle of the mooring. So this value is an average for the range of positions within that watch circle during the data

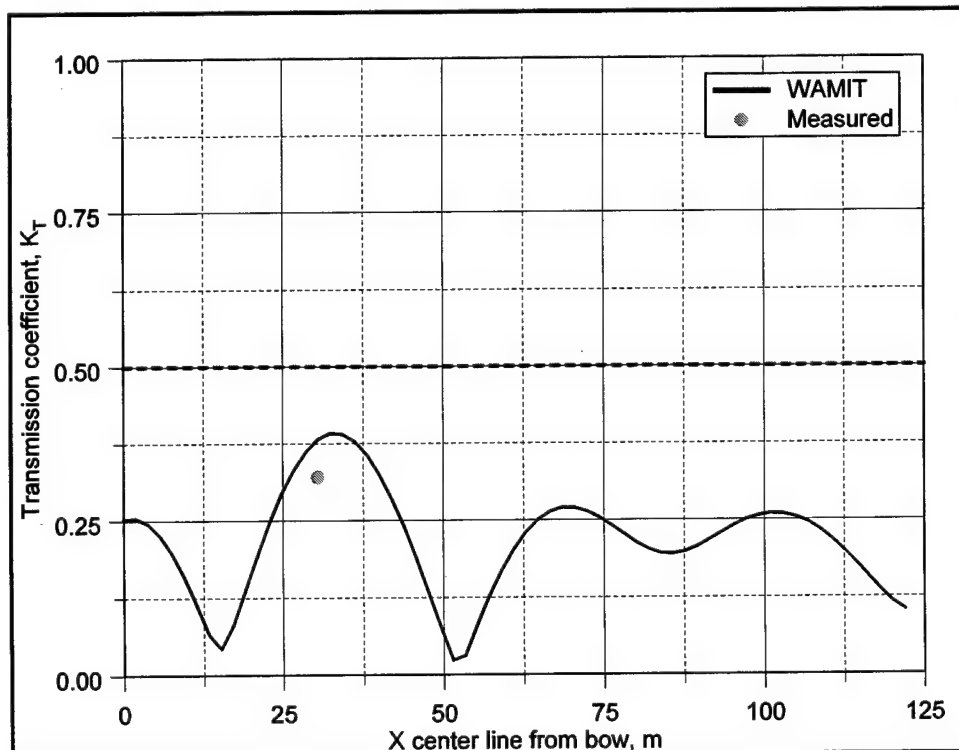


Figure 24. Measured vs. WAMIT wave transmission coefficients

collection interval. Thus, the field value could be plotted for points within the watch circle on either side of this curve and other WAMIT predictions on either side of the center line.

## Dynamic Pressures

### Measured pressures

The nine external pressure gages were analyzed for each of the three levels. Figure 25 is a typical plot of the bow, middle, and stern stations for the top level for May 25 at 1800 hours. Time series, frequency spectra, and relevant statistical estimates are shown for each of the three gage locations. Hard copy output for each of the 2,160 external pressure gage time series (i.e., 9 gages  $\times$  10 days  $\times$  24 hr/day) is archived in RIBS project notebooks and the calculated parameters are stored in files.

The internal and net pressure analyses were combined because there were only five internal pressure gage locations. Figure 26 is a typical plot of the external, internal, and net pressure time series and corresponding spectral analysis for May 25 at 1800 hours. This figure is similar to the previous one for the external gages. The external gage is repeated to show the relationship among the two measured pressures and the net pressure calculation. Again, hard copies of these 1,200 net pressure plots (i.e., 5 gages, 10 days, 24 hr/day) are stored in the RIBS project notebooks and the calculated parameters are stored in files.

Figure 27 is a time series of the average atmospheric pressure for the three reference gages. During the course of the field study, this parameter was very stable, varying between a low of 101.4 kP (14.70 psi) to a high of about 102.5 kP (14.86 psi).

Figure 28 shows the variation of the gage depth for the five external and internal gage pairs. For each pair, the solid line represents the external gage and the dashed line the internal gage. They group according to what vertical level they correspond to. These values were obtained from the static pressure for each gage. In general, these gage depths are consistent with the external and internal gage at approximately the same depths. This is essential for accurate net pressure estimates and also indicates that the RIBS XM99s set in the water were fairly consistent. The maximum vertical variation across the width of the XM99 was approximately 15 cm (0.5 ft) between the middle level, middle gages. These values vary slightly from the original gage vertical positions (Table 6) because they reflect the actual changes in the gages due to buoyancy changes and other factors affecting the RIBS XM99 flotation in the water.

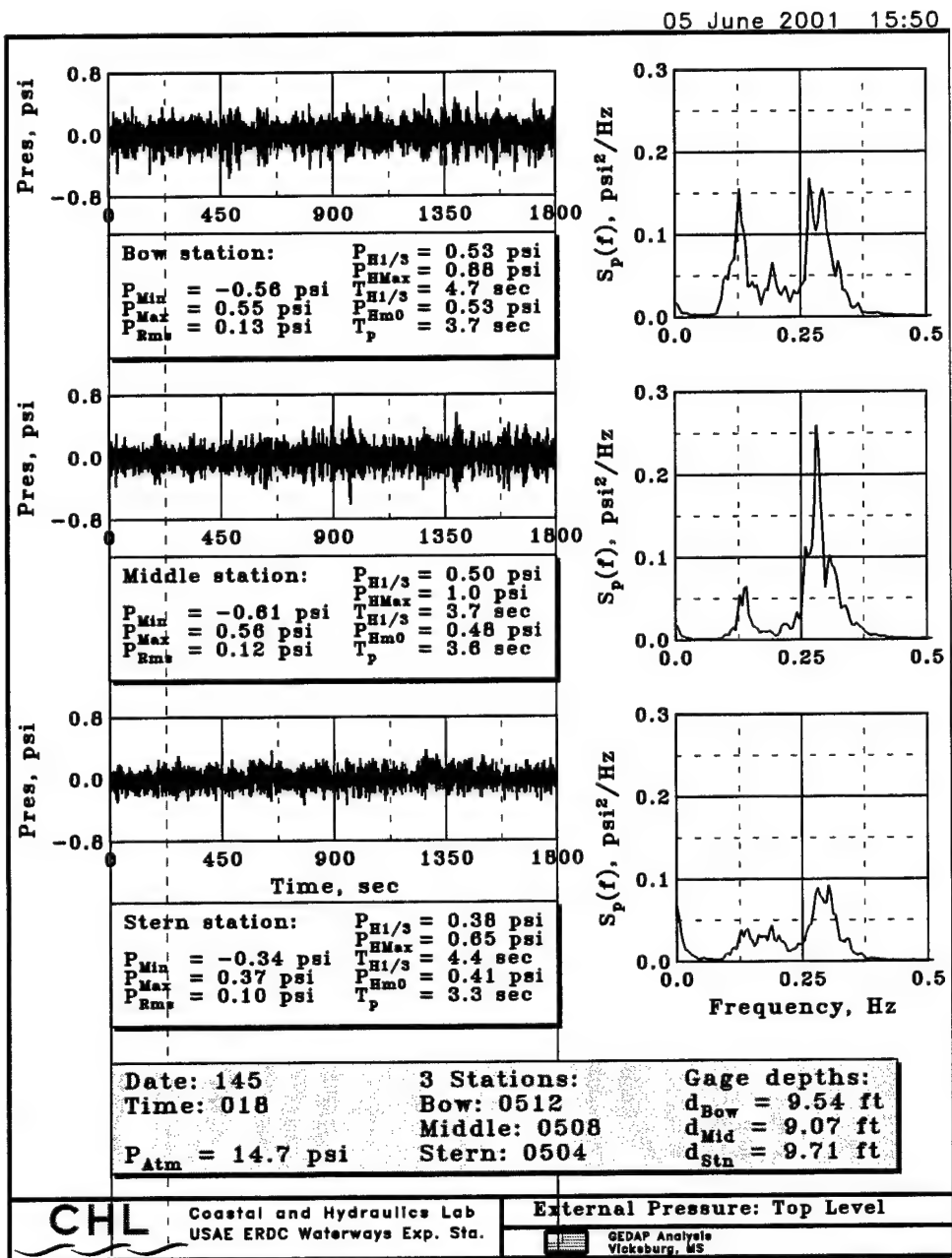


Figure 25. External pressure analysis for bow, middle, and stern stations of top level

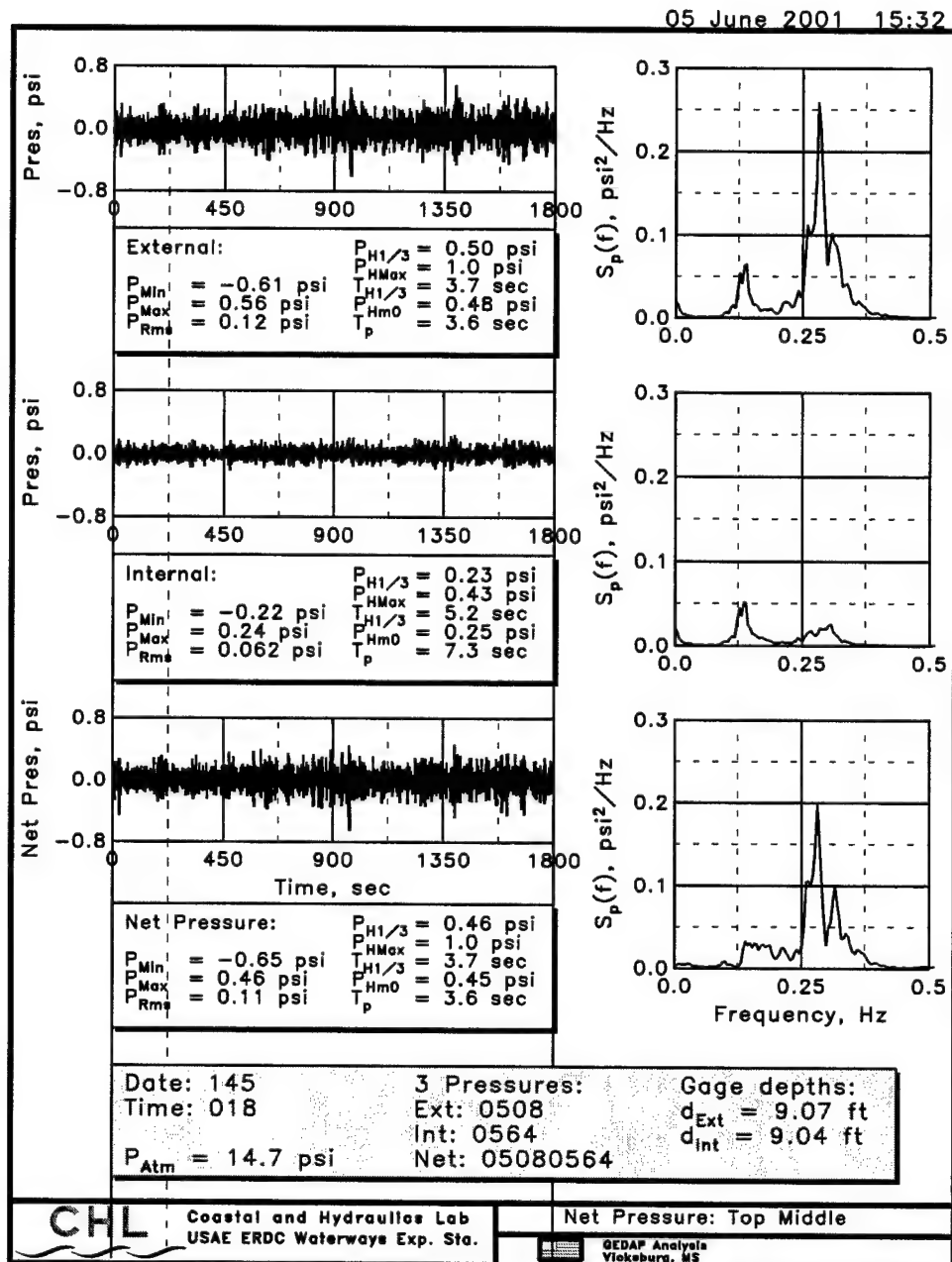


Figure 26. Net pressure analysis for bow, middle, and stern stations of top level

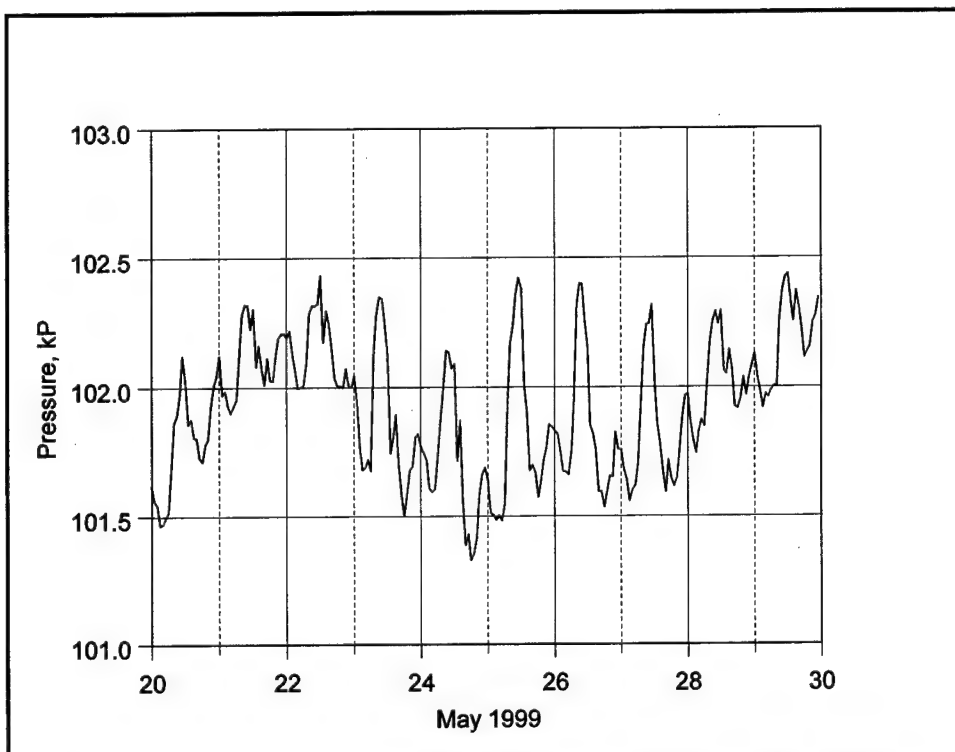


Figure 27. Average atmospheric pressure for three reference gages

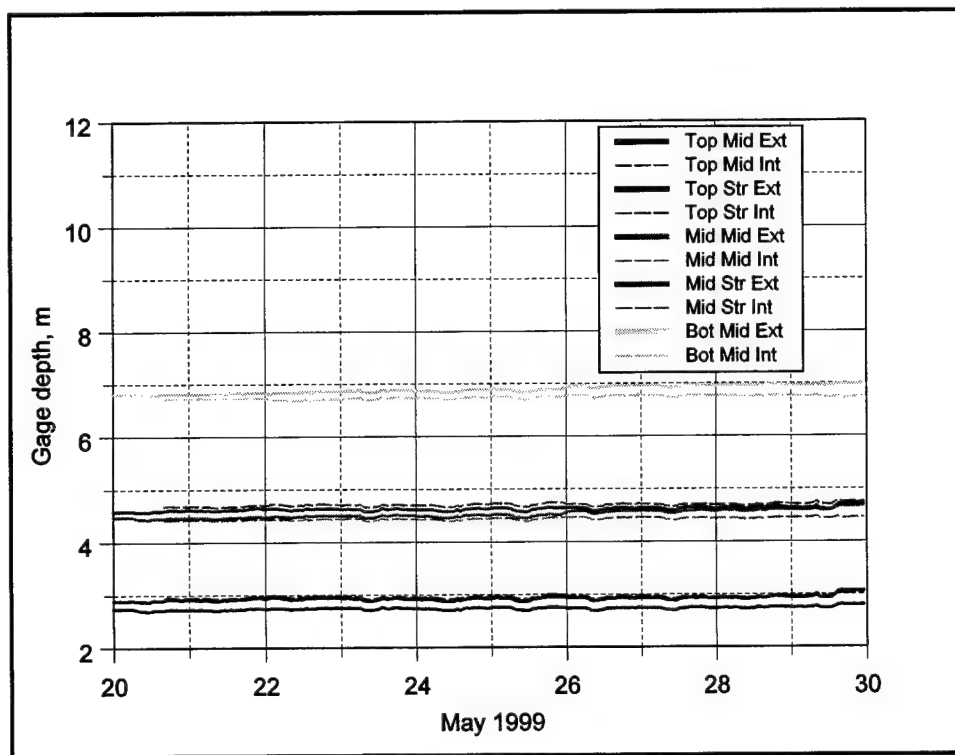


Figure 28. Measured external and internal pressure gage depths

The next three figures (Figures 29 to 31) show the external pressure gage depths in more detail for the top, middle, and bottom levels, respectively. For the top level (Figure 29), the variation in depth for all three gages was between approximately 2.7 and 3.1 m (8.85 and 10.1 ft). Figure 30 shows that the variation for the middle level gages was between 4.4 and 4.7 m (14.5 and 15.5 ft). For the bottom level, the variation was between 6.8 and 7.9 m (22.2 to 25.8 ft). The jumps on May 22, 26, and 29 for some of the gages correspond to changes in the integrity of the fabric and straps connecting the different levels. These were especially significant for the bottom stern gage, which reflected the cumulative displacements of the top two levels as well as some substantial deflection of its own on May 22 and 29. For comparisons to the analytical and numerical models, an average of 2.9, 4.4, and 6.9 m (9.5, 14.5, and 22.5 ft) was assumed for the three levels. Comparing these measurements of actual gage depths to the original values during the installation, indicates that the XM99 had about 21 to 36 cm (0.7 to 1.2 ft) of freeboard relative to the top level.

The next set of five figures, Figures 32 to 36, show the variation in external, internal, and net significant pressure for the five gage pairs. The significant double amplitude pressure is equivalent to the significant wave height for waves. It is based on the zero-downcrossing analysis in the time domain. Based on phasing between the external and internal gages, the net pressure can be greater than, equal, or less than the external pressure. The largest net pressure of approximately 9.31 kPa (1.35 psi) occurred on May 29 for the middle level, stern gage (Figure 35).

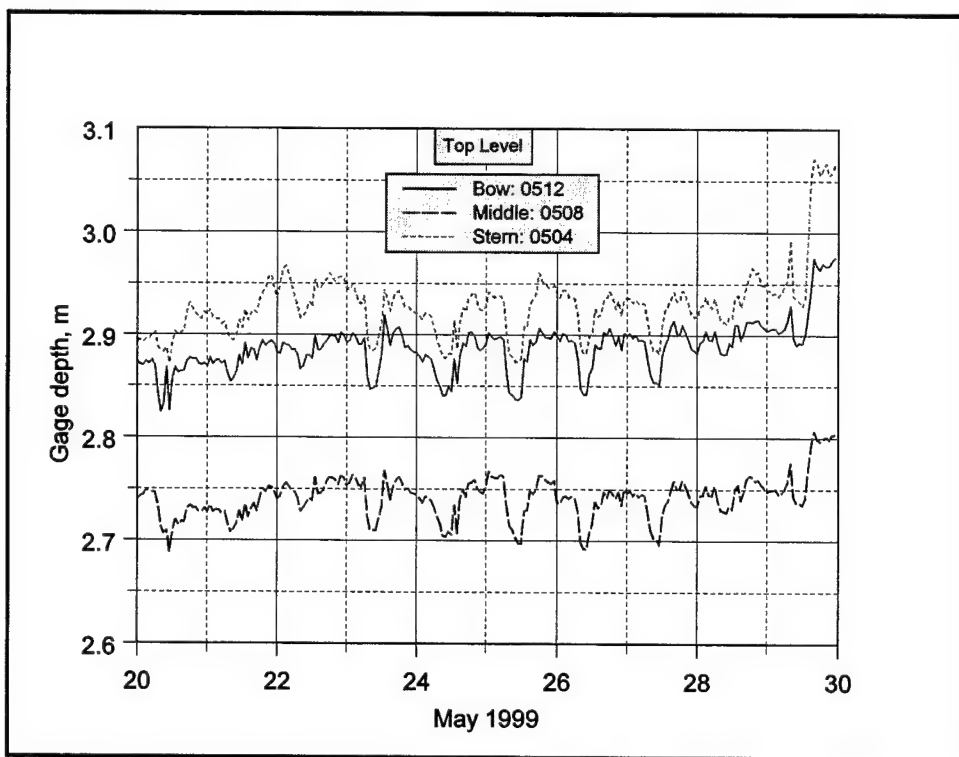


Figure 29. Top level external pressure gage depths

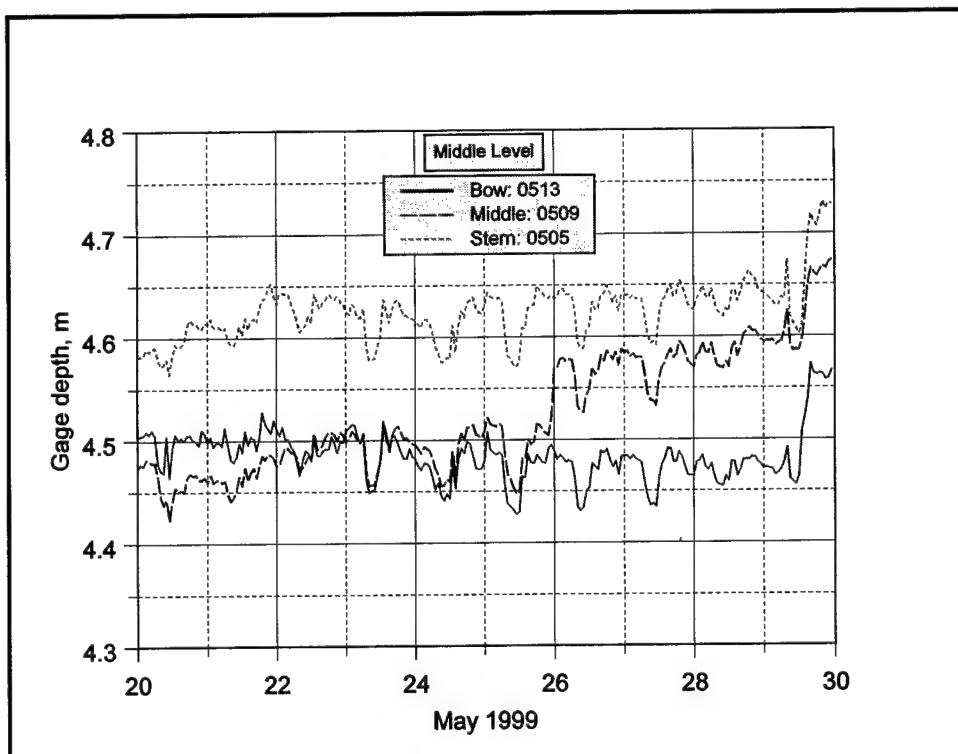


Figure 30. Middle level external pressure gage depths

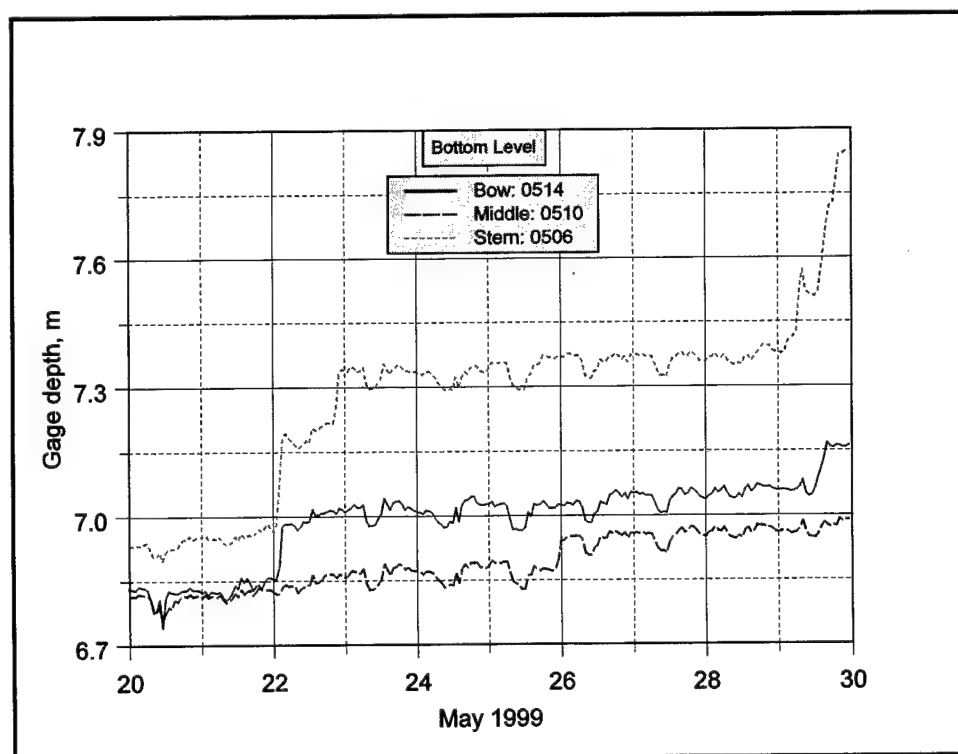


Figure 31. Bottom level external pressure gage depths

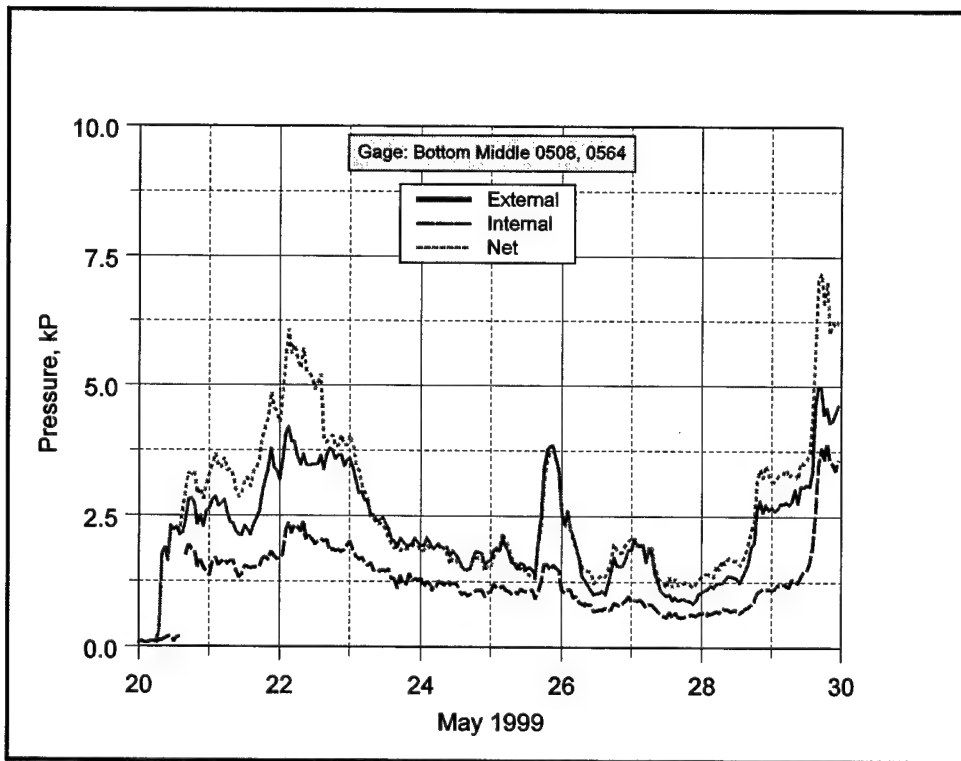


Figure 32. Time series of net pressure for top middle location

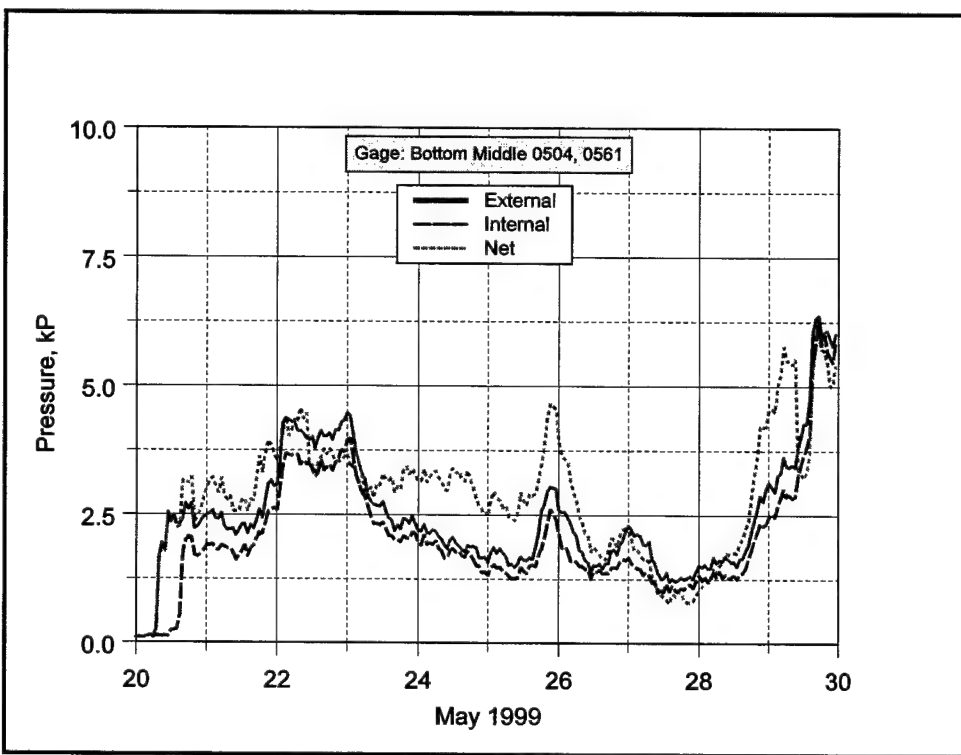


Figure 33. Time series of net pressure for top stern location

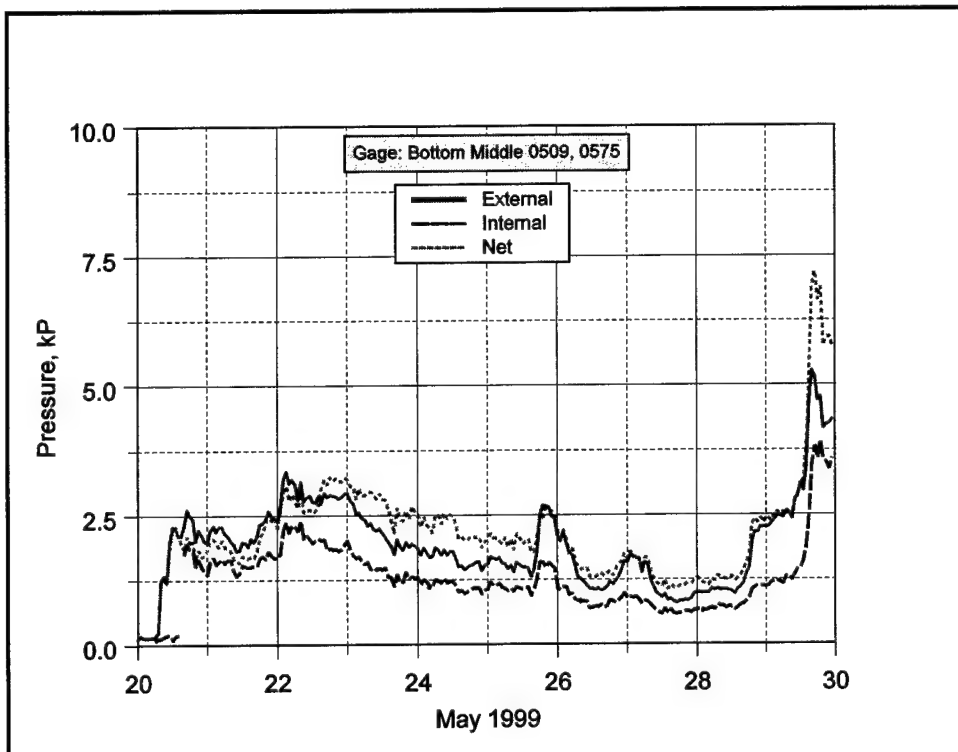


Figure 34. Time series of net pressure for middle middle location

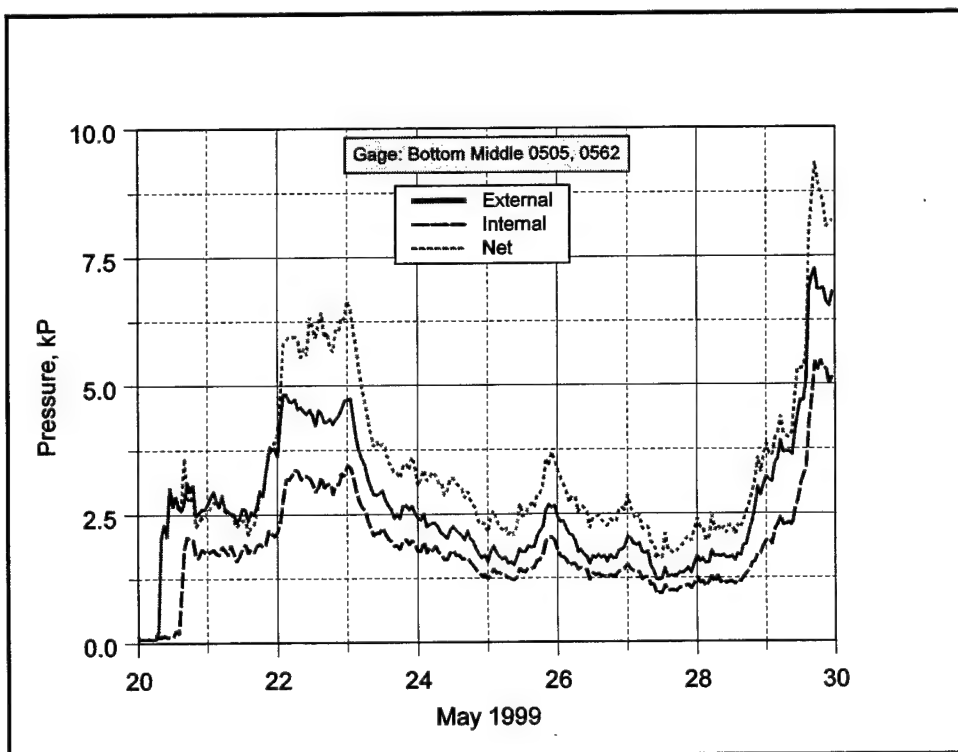


Figure 35. Time series of net pressure for middle stern location

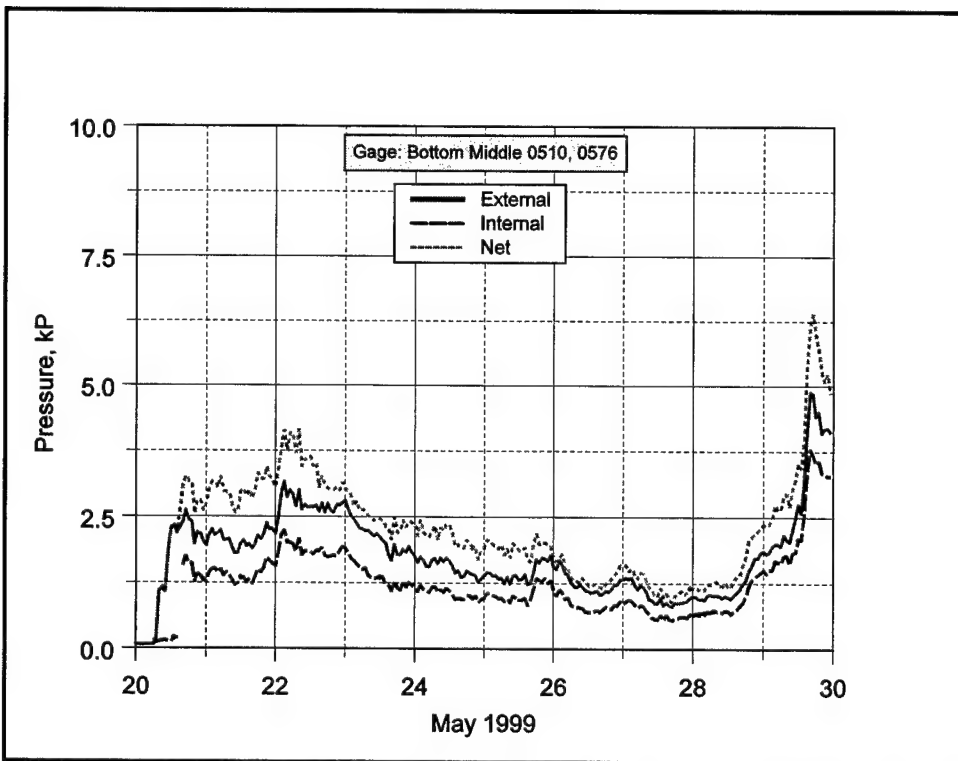


Figure 36. Time series of net pressure for bottom middle locations

Typical plots of minimum (solid line), maximum (dashed line), and RMS (dotted line) values are shown in the next three figures (Figures 37 to 39) for the external, internal, and net pressures at the top level, middle station. Twelve figures for the other four locations are contained in Appendix B.

The final group of three plots (Figures 40 to 42) from the measured data show the significant (solid line) and maximum (dashed line) double amplitude net pressures at the top, middle, and bottom levels, respectively. These pressure values are equivalent to significant and maximum wave heights. Two gage positions are included on the plots for the top and middle levels. The largest significant (9.31 kPa (1.35 psi)) and maximum (20.68 kPa (3.0 psi)) pressures occurred on May 29 for the middle level, stern gage.

### Analytical and numerical pressures

Figure 43 is a three-dimensional plot of the dynamic wave pressure from the WAMIT model for the 3-sec, 315-deg wave case. These pressures are “snapshots” in time of the spatial variation of pressure along the external side of the port leg. The twenty-four curves correspond to the estimated pressure at the center of each panel throughout the water column, spaced every 15 cm (0.5 ft) from the water surface. The decrease in pressure with depth is very apparent.

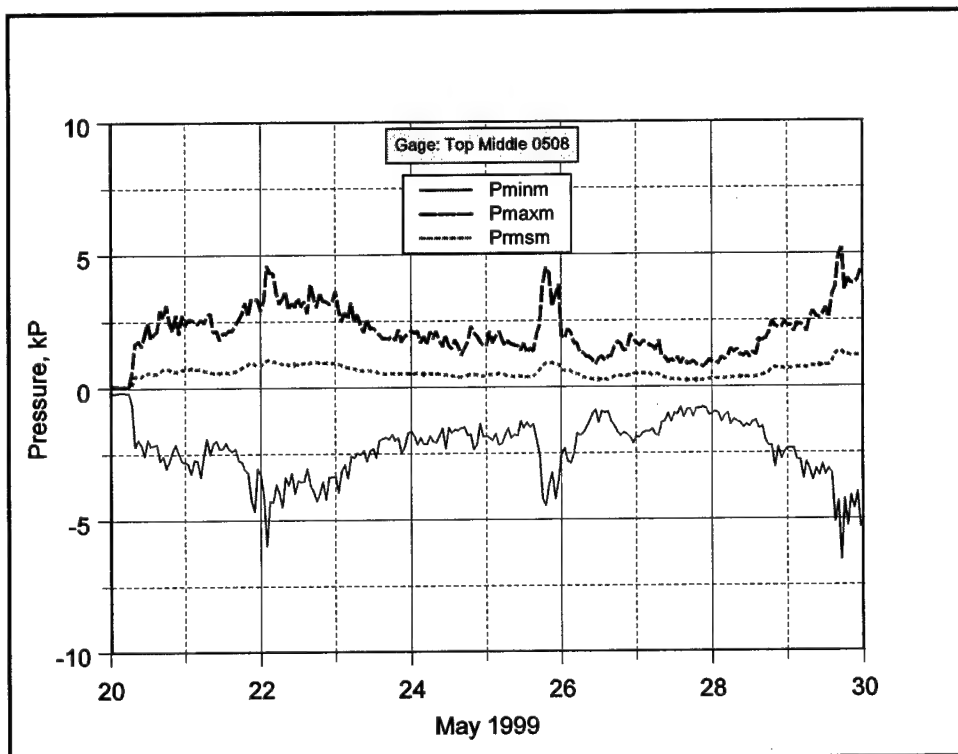


Figure 37. Time series of external pressure gage statistics for top middle location

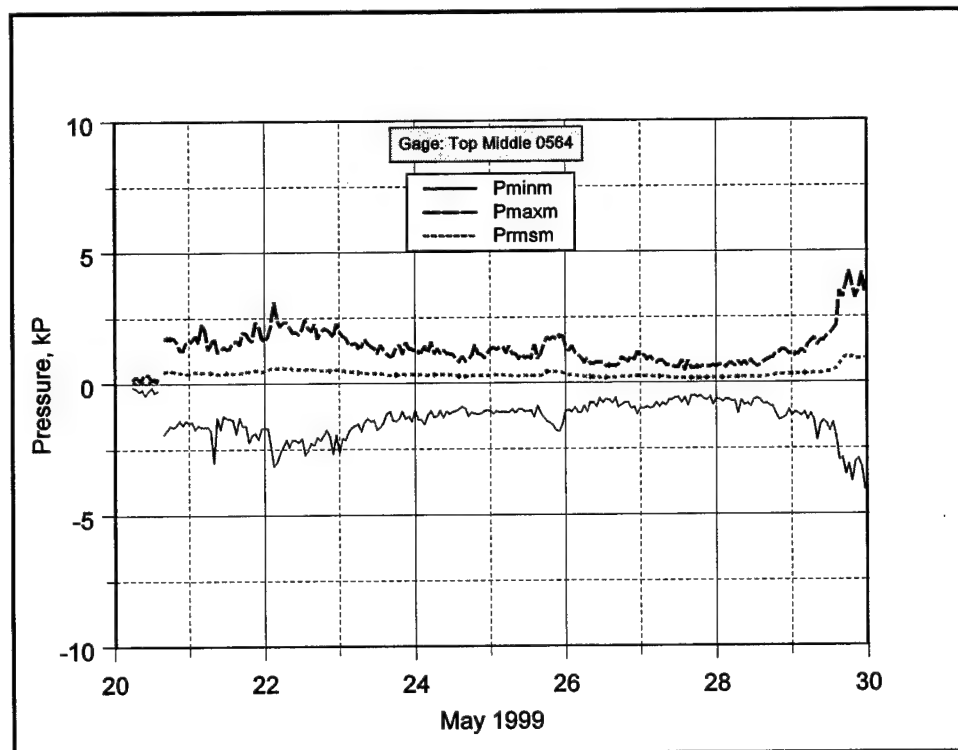


Figure 38. Time series of internal pressure gage statistics for top middle location

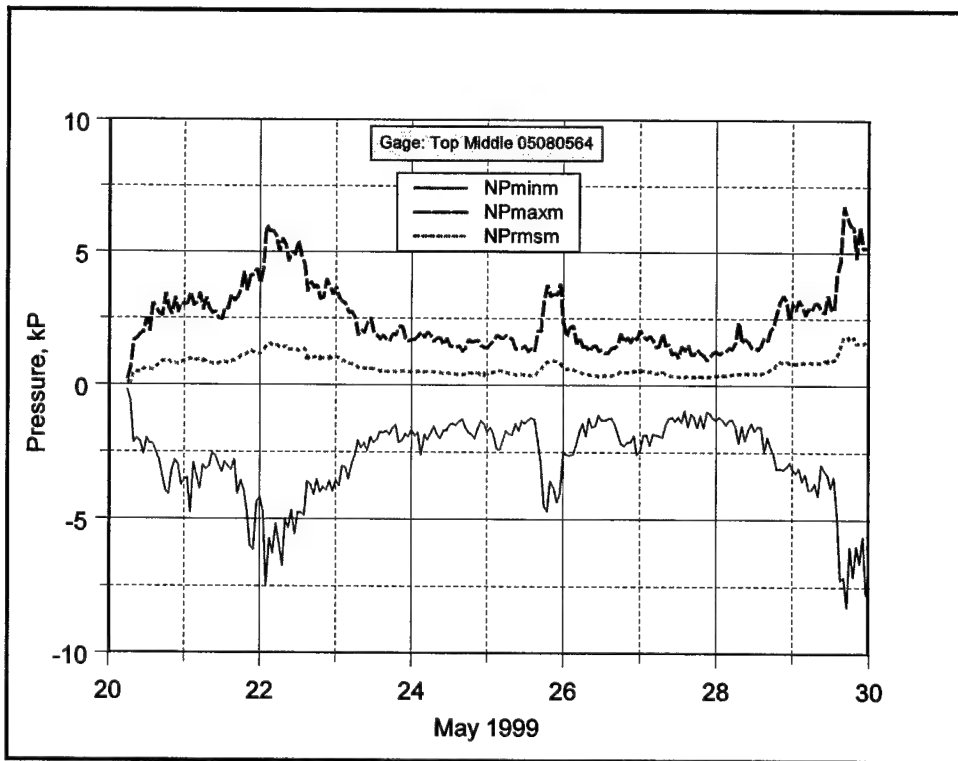


Figure 39. Time series of net pressure gage statistics for top middle location

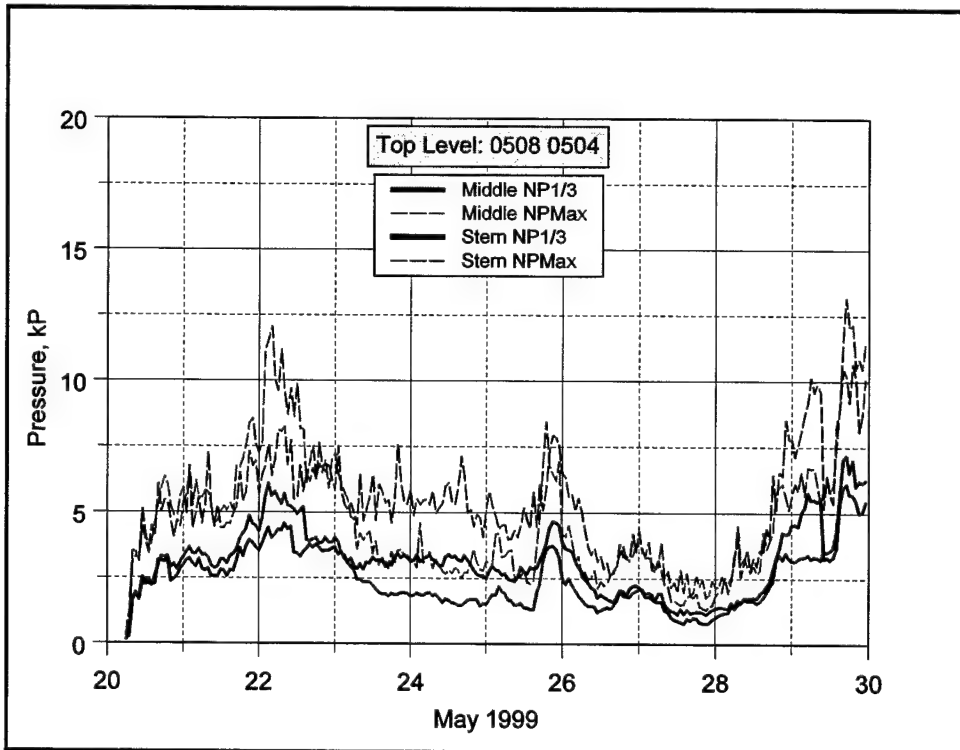


Figure 40. Time series of significant and maximum net pressures on top level

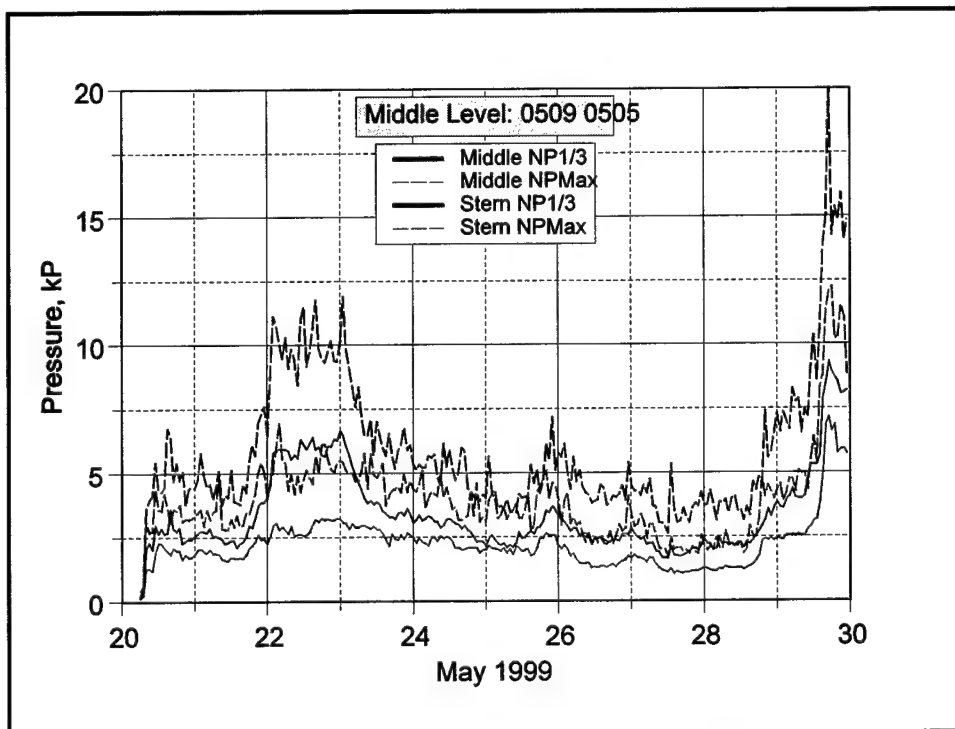


Figure 41. Time series of significant and maximum net pressures on middle level

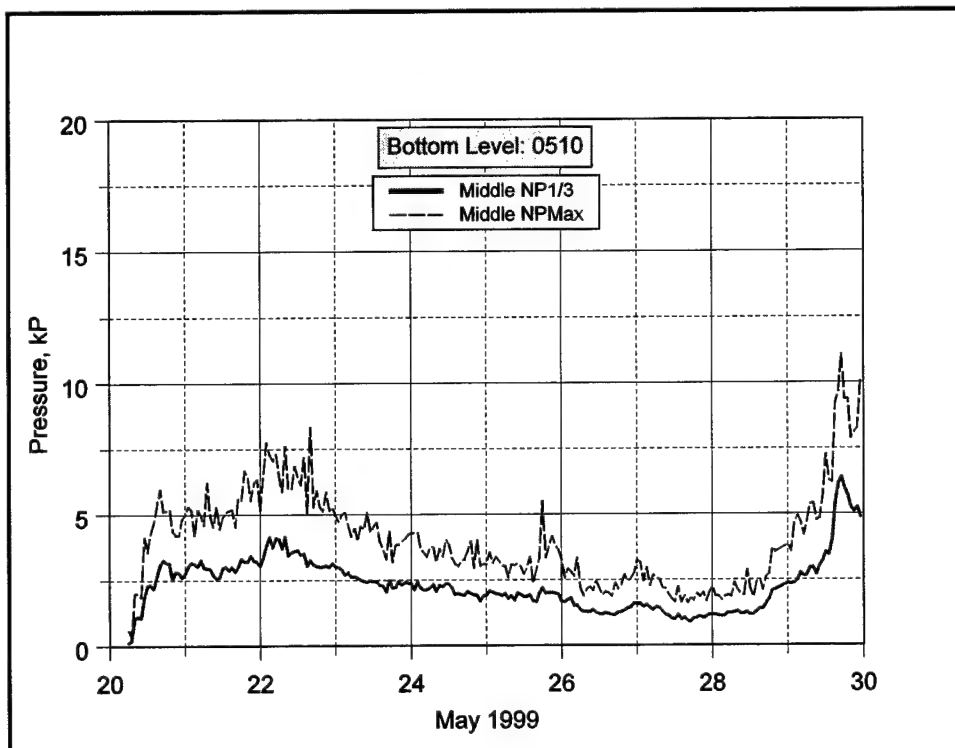


Figure 42. Time series of significant and maximum net pressures on bottom level

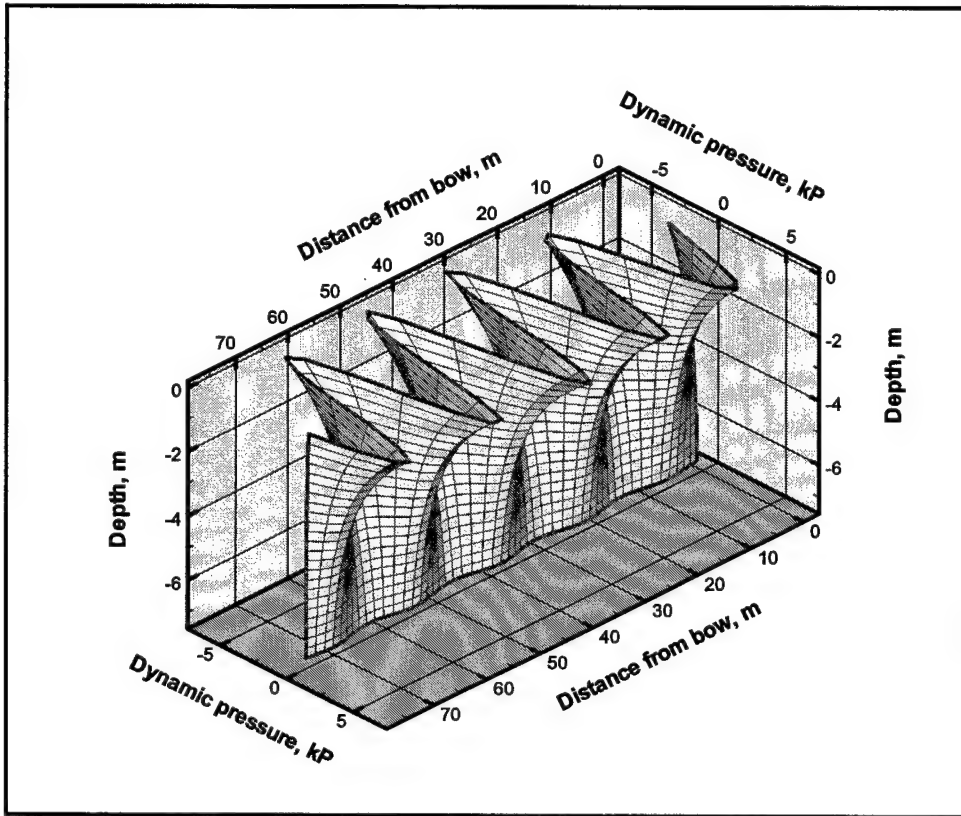


Figure 43. WAMIT external dynamic pressure, 3-D view

Figure 44 is an x-y plot of the same data as Figure 43 for the levels corresponding to the three pressure gage depths.

Figure 45 compares dynamic pressure significant double amplitudes from the analytical and numerical models to the field measurements. The nine locations representing the three levels and three stations along the external port leg are shown. Distances are measured from the nose or bow of the RIBS XM99. For the top level, the analytical prediction is constant along the length of the port leg. The WAMIT numerical predictions exhibit some variability along the leg, being smaller at the bow and larger in the middle, than the analytical value. The field measurement from the stern is much less than either analytical or numerical predictions. A possible explanation for this is that the stern was sitting lower in the water than the models and experienced some “tail wagging” oscillations that might have reduced the recorded pressures. At the middle level, field measurements were slightly higher than the analytical and numerical predictions. The bow middle level gage did not work during the entire deployment. At the lower level, the analytical and numerical predictions were in good agreement, but the field values were much higher. Since the bottom level was actually lower in the water than the model at the bow and stern (between 7.0 to 7.4 m (23 to 24.2 ft)), one would expect that the field dynamic pressures would be smaller and not larger than the model predictions. Additional comparisons are being made with other wave cases to see if this was an aberration in the data.

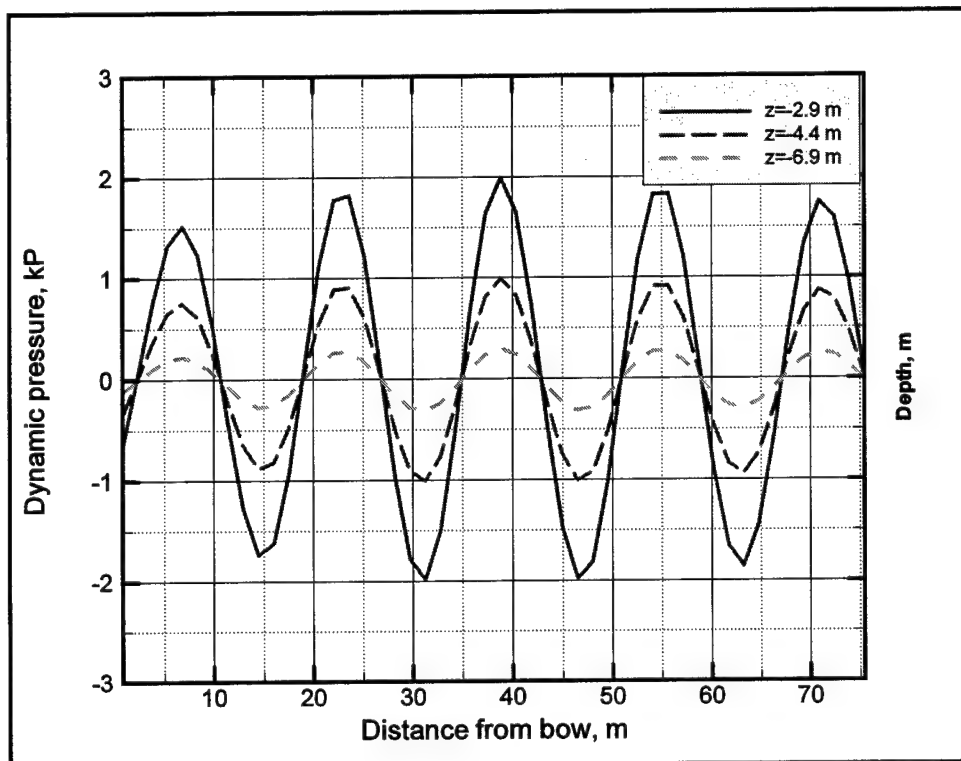


Figure 44. WAMIT external dynamic pressure, three gage levels

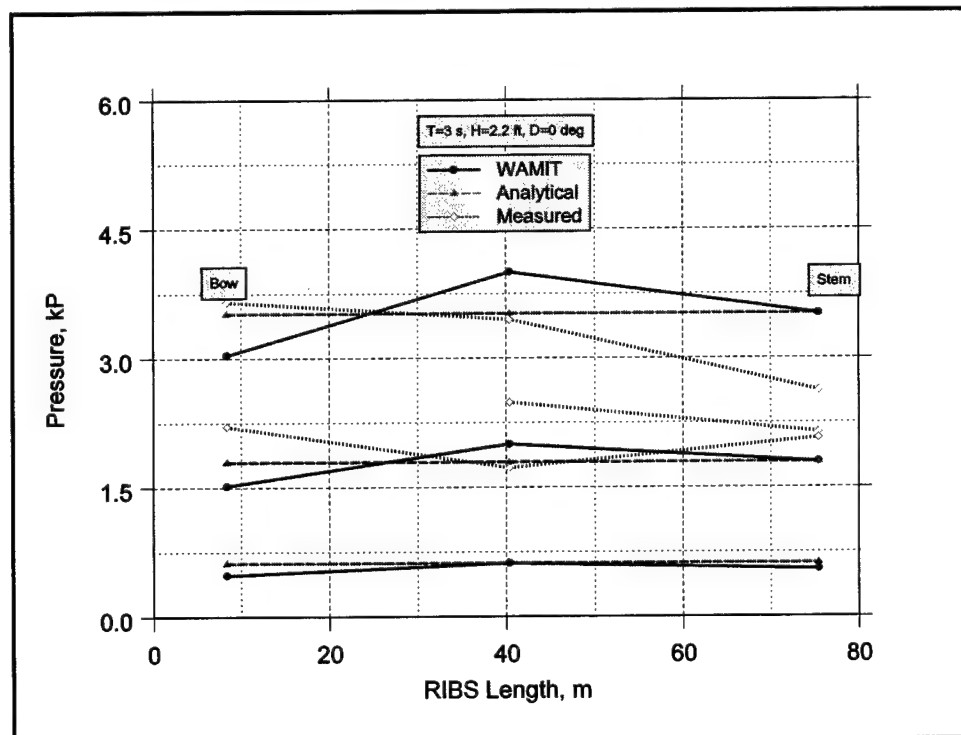


Figure 45. Comparison of analytical, WAMIT, and measured external pressures

## 7 Summary and Conclusions

---

The U.S. Army Engineer Research and Development Center deployed the first ocean-scale version of the RIBS approximately 4.8 km (3 miles) from Port Canaveral, FL, in May 1999. The RIBS XM99 prototype consisted of two legs in a “V” shape in plan view. Each leg was approximately 77.1 m (253 ft) long, 2.4 m (8 ft) wide, and 7.3 m (24 ft) deep. Water depth was 13.4 m (44 ft). The novel construction technique consisted of rigid steel truss frames and flexible membrane panels in a “Venetian blind” or vertically expandable arrangement.

This field study was one of the most heavily instrumented floating breakwater studies ever conducted. Instrumentation included sensors for measuring incident and transmitted waves, dynamic pressures, structural displacements, accelerations and strains, and mooring line loads.

The purpose of this report is to describe analytical and numerical models used to predict the performance and structural response of the RIBS XM99. The performance of a floating breakwater can be quantified by the wave transmission coefficient. The structural response can be estimated using the wave-induced dynamic pressures along the structure. These pressures can be used to calculate the wave forces and moments, operational stresses, and ultimate RIBS design for survivability.

The analytical model used in this study is based on linear wave theory and assumes the RIBS XM99 is idealized as a fixed, rigid, vertical barrier. This model includes contributions to the wave transmission and dynamic pressure from incident, reflected, and transmitted waves.

The numerical model used in this study is the linear radiation/diffraction program WAMIT for the analysis of wave-structure interaction. It solves a boundary value problem consisting of finding the velocity potential that satisfies the Laplace equation and four linearized boundary conditions for the free surface, bottom, body surface, and the radiation condition at infinity. The analysis is performed in the frequency domain, with the flow assumed to be ideal and time-harmonic. In the solution for the diffraction plus radiation potentials, WAMIT provides the wave transmission coefficients and dynamic pressures on a rigid, floating RIBS XM99 panel model.

Incident and transmitted wave parameters were calculated using time and frequency domain methods. In the frequency domain, both single channel and directional wave spectral analyses were performed. The GEDAP software package was used to estimate time domain and single channel frequency domain parameters. The directional spectral analysis was provided by the onboard Datawell software and a Matlab version of MLM patterned after the CHL laboratory standard. Significant wave heights and periods, and overall mean wave directions and directional spreads were estimated and compared. The data were presented in the form of x/y, frequency and directional spectra, and joint distribution plots.

The deployment period was characterized by unimodal sea or swell only, combined bimodal, and even multimodal, sea and swell wave spectra. The sea conditions are representative of SS3 and smaller sea states with wave periods less than 6 sec. Whether unimodal or multimodal, the wave data grouped into either sea or swell bands of frequencies or periods. During the deployment, significant wave heights were less than SS3, except for periods on May 22 and May 29. Maximum wave heights exceeded the SS3 lower limit on many occasions, however. Peak wave periods were within the SS3 window on many occasions. The largest significant wave height was 1.15 m (3.77 ft) at a peak wave period of 4.71 sec. The largest peak period was 10.9 sec at a significant wave height of 0.70 m (2.30 ft).

The optimum “design” condition included waves traveling from 255 to 375 deg, with the RIBS XM99 aligned with 315 deg. Waves were recorded in the vicinity of 315 deg for several hours between May 24 and May 27. Waves with mean wave directions of 315 deg occurred on three occasions. Waves within  $\pm 15$  deg of 315 deg occurred 22 times with wave periods ranging from 2.7 to 4.2 sec. Directional spreading ranged from 30 to 80 deg during the deployment, the former value representative of a more narrow directional spreading. The minimum spreading value was 29.5 deg at 4.2 sec.

Wave transmission coefficients are presented based on several different methods of calculation. An overall value for the entire wave field is based on the zero moment wave height  $H_{m0}$ . A frequency-dependent transmission coefficient  $K_T(f)$  is calculated as the ratio of transmitted and incident wave spectral estimates at frequency  $f$ . A weighted average of the frequency-dependent wave transmission coefficient is also calculated. It is based on multiplying the  $K_T(f)$  by a weighting function over a range of frequencies. Two different weighting functions were used. One was a simple average from a lower cutoff frequency of 0.17 Hz, corresponding to the SS3 frequency. The second method involved an energy-based weight determined from the amount of energy in each frequency band. Justification for these weighting functions is because the RIBS XM99 is smaller in length and shallower in draft than a full-scale prototype would be to efficiently reduce SS3 wave conditions. This procedure allows us to look at the performance of the XM99 on a frequency by frequency basis.

Comparisons of measured wave transmission coefficients were made for a sample case at 1800 hours on May 25, 1999. This incident wave had a peak

period of 3.4 sec, height of 72 cm (2.36 ft), direction of 321 deg, and directional spreading of 39 deg. It was an ideal case for SS3 waves traveling along the XM99 center line (i.e., 315 deg). The wave transmission coefficient was 0.43 for the zero moment method and 0.37 for the simple average method with lower cutoff frequency at SS3.

Time series of wave transmission coefficients during the XM99 deployment were plotted for the different methods of calculation. The simple average method estimates were usually smaller than those from the zero moment wave height method. Wave transmission coefficients were less than the  $K_T = 0.5$  desired level of efficiency (i.e., dashed line) for several hours every day, with the best performances on May 22, 23, 25, 26, and 28. These excellent performances correspond to times when wave periods, direction, directional spreading, and spectral shape were within the design limits of the RIBS XM99.

Joint distribution plots of wave transmission coefficient and peak wave period were plotted for the different estimation methods. Wave transmission values group into either sea or swell regimes depending on whether the dominant mode of the waves is in the sea or swell band of frequencies. There were a large number of wave transmission values less than the threshold for both sea and swell conditions, especially using the simple average method.

Comparisons of wave transmission coefficients from the WAMIT model and the field measurement for the example case were made. Along the center line, WAMIT predicted a slow oscillation with values ranging from 0.03 to 0.4. The transmitted gage appears to have been located at the point of an antinode for this wave period and direction. The agreement was very good. Additional comparisons between the numerical model and field measurements will be conducted and reported later.

Wave pressures were measured at 12 external and five internal locations on the port leg of the RIBS XM99. On the external side, gages were located at three stations on each of four vertical levels. The three stations are bow, middle, and stern. The four levels are the surface, top, middle, and bottom. The five gages on the internal side were located on the top, middle, and bottom levels at the middle and stern stations.

Gage depths for each pressure gage location were calculated after subtracting atmospheric pressure. Dynamic and net wave pressures were calculated for each location. The net pressure was calculated by subtracting the internal pressure gage from the external pressure at the five locations. Time and frequency domain parameters from the time series for external, internal, and net pressures included the minimum and maximum pressures, RMS pressure, significant pressure height and associated period, and maximum pressure height.

Time series of the external pressure gage depths for the top, middle, and bottom levels were plotted. For the top level, the variation in depth for all three gages was between approximately 2.7 and 3.1 m (8.85 and 10.1 ft). The variation for the middle level gages was between 4.4 and 4.7 m (14.5 and 15.5 ft).

For the bottom level, the variation was between 6.8 and 7.9 m (22.2 to 25.8 ft). Changes in the integrity of the fabric and straps connecting the different levels were reflected in jumps in depth on May 22, 26, and 29. These were especially significant for the bottom stern gage that reflected the cumulative displacements of the top two levels as well as some substantial deflection of its own on May 22 and 29.

Time series of significant pressures for the external, internal, and net pressures were plotted. The significant double amplitude pressure is equivalent to the significant wave height for waves. Based on phasing between the external and internal gages, the net pressure can be greater than, equal, or less than the external pressure. The largest net pressure of approximately 9.3 kP (1.35 psi) occurs on May 29 for the middle level, stern gage. The largest significant (9.3 kP (1.35 psi)) and maximum (20.7 kP (3.0 psi)) pressures occur on May 29 for the middle level, stern gage.

Comparisons among the analytical and numerical predictions and the field measurements were made for the example case at the nine external locations. The analytical predictions were constant at each level. The WAMIT predictions exhibited some variability along the leg, especially at the top level, relative to the analytical values. In general, the agreement between analytical and numerical predictions was very good. The field measurements exhibited more variability, but were good at most locations. Possible explanations for these discrepancies are nonlinear fluid motions and structural interactions (i.e., tail wagging, mach stem waves, oscillations of the fabric and levels) that the analytical and numerical models do not include.

Analysis of the myriad data collected during the XM99 deployment is ongoing. The purpose of this report was to document some of these initial efforts and make the reader aware of the wealth of data that is available and can be used to improve our analytical and numerical models. Future research efforts are expected to continue for several years as the RIBS team incorporates more of the performance and structural response results from this very successful field experiment in the design of the final prototype RIBS.

# References

---

American Institute of Steel Construction, Inc. (1990). *Manual of steel construction*. New York, NY.

Briggs, M. J., Fowler, J. E., Bratos, S. M., Resio, D. T., and Pollock, C. B. (1996). "RIBS: A potential solution for logistics-over-the-shore," *20<sup>th</sup> Army Science Conference*, Norfolk, VA.

Briggs, M. J., Demirbilek, Z., and Matheu, E. E. (1998). "An integrated study of wave phenomena affecting floating breakwater design for JLOTS," *21<sup>st</sup> Army Science Conference*, Norfolk, VA, Jun 15-17.

Fathi, D. E., Lee, C. -H., and Newman, J. N. (1994). "Computation of Wave induced motions on a flexible container," *Hydroelasticity in marine technology*. Faltinsen et al., ed., Balkema, Rotterdam, 301-308.

Fowler, J. E., Resio, D. T., Briggs, M. J., and Pollock, C. B. (1996). "Potential uses for the rapidly installed breakwater system," *International Conference on Coastal Engineering*, 127, 1631-1639, Orlando, FL.

Helm-Petersen, J. (1998). "Estimation of wave disturbance in harbors, Series Paper No. 15," Ph.D. diss., Hydraulics & Coastal Engineering Laboratory, Aalborg University, Aalborg, Denmark, 136.

Jones, J. B. (1971). "Transportable breakwaters - A survey of concepts, NTIS," Technical Report AD-887 841, Naval Facilities Engineering Command, Port Hueneme, CA.

Kobayashi, N. (1998). "RIB wave field model development," Contract Report DACA39-98-M-0279, Center for Applied Coastal Research, University of Delaware, Newark, DE.

Kriebel, D. L., and Bollman, C. A. (1996). "Wave transmission past vertical wave barriers," *25<sup>th</sup> International Conference on Coastal Engineering* 191, 2,470-2,483.

Krouse, J. (1998). "Virtual ocean computer simulation," *Sea Technology*, 64-65.

Lee, C. -H. (1995a). *WAMIT theory manual*. Massachusetts Institute of Technology, Cambridge, MA.

Lee, C. -H. (1995b). *WAMIT user's manual*, Version 5.3. Massachusetts Institute of Technology, Cambridge, MA.

Lee, C. -H. (1997). "Wave interactions with huge floating structure," BOSS 97.

Liu, P. L. -F., and Abbaspour, M. (1982). "Wave scattering by a rigid thin barrier," *Journal of Waterway, Port, Coastal, and Ocean Division*, 108(WW4), 479-491.

Losada, I. J., Losada, M. A., and Roldan, A. J. (1992). "Propagation of oblique incident waves past rigid vertical thin barriers," *Applied Ocean Research* 14, 191-199.

Mandal, B. N., and Dolai, D. P. (1994). "Oblique water wave diffraction by thin vertical barriers in water of uniform finite depth," *Applied Ocean Research*. Elsevier, 195-203.

Newman, J. N. (1994). "Wave effects on deformable bodies," *Applied Ocean Research* 16, 47-59.

Newman, J. N. (1997). "Recent results from numerical model tests," *OTRC '97 International Conference, Nonlinear Design Aspects of Physical Model Tests*, College Station, TX, 1-27.

Newman, J. N., and Lee, C. -H. (1992). "Sensitivity of wave loads to the discretization of bodies," *BOSS '92*, London.

Peratovich, Nottingham, and Drage, Inc. (1992). "Wave barrier development," Final report to the Alaska Science and Technology Foundation.

Resio, D. T., Fowler, J. E., and Briggs, M. J. (1995). "RIBS: A potential solution to the lots sea-state problem," *Army Office of Research Symposium*, Ft. Lee, VA.

Resio, D. T., Briggs, M. J., Fowler, J. E., and Markle, D. (1997). "Floating V-shaped breakwater," U.S. Patent No. 5,702,203, December 30, 1997.

Sawaragi, T. (1995). *Coastal engineering - Waves, beaches, wave-structure interactions*. Elsevier, New York, NY.

Ursell, F. (1947). "The effect of a fixed barrier on surface waves in deep water," *Proc. Camb. Phil. Soc.* 43, 374-82.

Wiegel, R. L. (1960). "Transmission of waves past a rigid vertical thin barrier," *Journal of Waterway, Port, Coastal, and Ocean Division*, 86(WW1), 1-12.

Zhao, R., and Triantafyllou, M. (1994). "Hydroelastic analyses of a long flexible tube in waves," *Hydroelasticity in marine technology*. Balkema, Rotterdam, 287-300.

# Appendix A

## Mass Moments of Inertia

---

### Theory

This appendix describes the procedure for calculating the mass moments of inertia for the RIBS XM99 as used in the WAMIT numerical model. Details are given for the pitch, roll, and yaw moments. The RIBS XM99 is idealized as a beam or channel (American Institute of Steel Construction Handbook 1990)<sup>1</sup> in these calculations.

#### Global coordinate system

The global coordinate system and layout for the RIBS is shown in Figure A1(a). It is the same as used in the main report for the WAMIT layout.

#### Pitch mass moment of inertia

Figure A1(b) is a schematic of the RIBS XM99 layout for one leg relative to pitch motions. A local coordinate system is defined relative to the global system. The  $y'$ -axis is parallel to the longitudinal axis of the leg, with origin at the center of gravity C. The RIBS XM99 leg has length  $L = 76.2$  m (250 ft) and beam  $B = 2.4$  m (8 ft). The angle  $\phi$  between the local  $x'$ -axis and the global  $x$ -axis is

$$\phi = 90 - \theta, \quad (A1)$$

The first step is to calculate the area moment of inertia  $I_y$  about the global  $y$ -axis for the one leg. It is defined as

$$I_y = I_{x'} \sin^2 \phi + I_{y'} \cos^2 \phi \quad (A2)$$

---

<sup>1</sup> References cited in this appendix are listed in the References at the end of the main text.

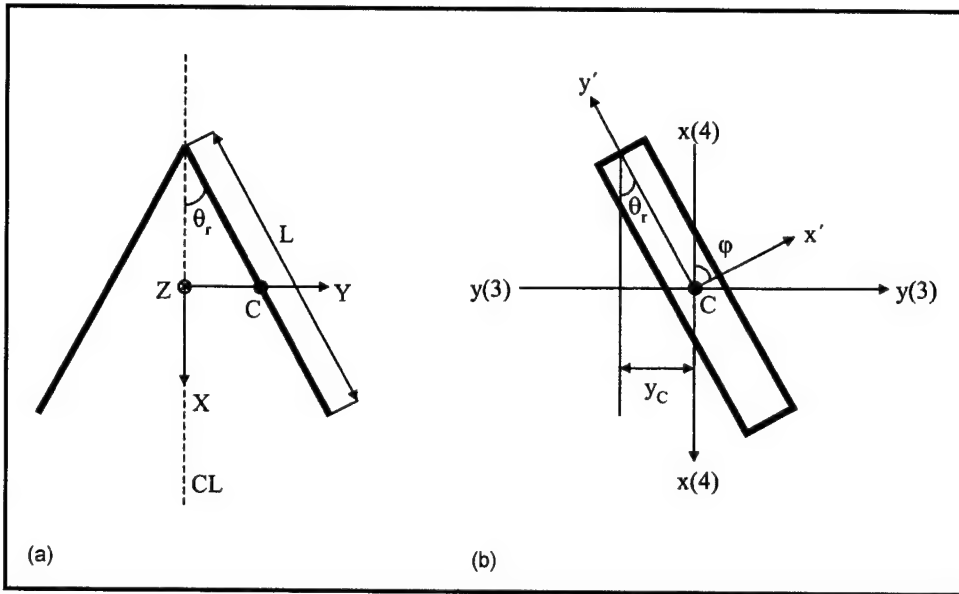


Figure A1. Schematic of RIBS XM99 for moment of inertia calculations. (a) plan view with global coordinate system, (b) expanded view of one leg with local coordinate system

where

$$I_{x'} = \frac{BL^3}{12} = \text{area moment of inertia about the local } x'\text{-axis and}$$

$$I_{y'} = \frac{LB^3}{12} = \text{area moment of inertia about the local } y'\text{-axis.}$$

After substitution and rearranging,  $I_y$  becomes

$$I_y = \frac{BL}{12} \left[ (L \cos \theta_r)^2 + (B \sin \theta_r)^2 \right] \quad (A3)$$

The next step is to calculate the pitch mass moment of inertia  $I_{yy}$  given by

$$I_{yy} = \frac{\rho BLT}{12} \left[ (L \cos \theta_r)^2 + (B \sin \theta_r)^2 \right] \quad (A4)$$

where  $\rho$  is water density and  $T$  is the RIBS draft. Finally, the total pitch moment for both RIBS legs is

$$I_{yy_{tot}} = 2I_{yy} = \frac{\rho BLT}{6} \left[ (L \cos \theta_r)^2 + (B \sin \theta_r)^2 \right] \quad (A5)$$

### Roll mass moment of inertia

The procedure is similar as before for the pitch moment. Because of the offset  $y_c$  of the center of gravity with the global  $x$ -axis, the parallel axis theorem is required to calculate the area moment of inertia for one leg about the  $x$ -axis. It is given by

$$I_x = \bar{I}_x + A y_c^2 \quad (A6)$$

where

$$\bar{I}_x = I_x \cos^2 \phi + I_y \sin^2 \phi = \frac{BL}{12} \left[ (L \sin \theta_r)^2 + (B \cos \theta_r)^2 \right] \quad (A7)$$

and

$$A y_c^2 = BL \left( \frac{L}{2} \cos \phi_r \right)^2 = \frac{BL^3}{4} \sin^2 \theta_r \quad (A8)$$

Combining Equation A6 and A7 and rearranging, the area moment of inertia about the  $x$ -axis is

$$I_x = \frac{BL}{12} \left[ 4(L \sin \theta_r)^2 + (B \cos \theta_r)^2 \right] \quad (A9)$$

The roll mass moment of inertia  $I_{xx}$  for one RIBS leg is

$$I_{xx} = \rho T I_x = \frac{\rho BL T}{12} [4(L \sin \theta_r)^2 + (B \cos \theta_r)^2] \quad (A10)$$

Finally, the mass moment of inertia in roll for both RIBS legs is

$$I_{xx_{tot}} = 2 I_{xx} = \frac{\rho BL T}{6} [4(L \sin \theta_r)^2 + (B \cos \theta_r)^2] \quad (A11)$$

### Yaw mass moment of inertia

The yaw mass moment of inertia  $I_{zz_{tot}}$  is just the sum of the pitch and roll moments given as

$$I_{zz_{tot}} = I_{xx_{tot}} + I_{yy_{tot}} \quad (A12)$$

## Example Problem

For the XM99, the input parameters are as follows:

$$\begin{aligned}L &= 76.2 \text{ m (250 ft)} \\B &= 2.4 \text{ m (8 ft)} \\T &= 7.3 \text{ m (24 ft)} \\\theta_r &= 30 \text{ deg} \\\rho &= 1025 \text{ kg/m}^3 (2 \text{ lb}_m / \text{ft}^3)\end{aligned}$$

The roll mass moment of inertia is given by Equation A10 as

$$I_{xx_{tot}} = \frac{1025(2.44)(76.2)(7.32)}{6} [4(76.2 \sin 30)^2 + (2.44 \cos 30)^2] = 1.351 \times 10^9 \text{ kg-m}^2 \quad (\text{A13})$$

The pitch mass moment of inertia is given by Equation A4 as

$$I_{yy_{tot}} = \frac{1025(2.44)(76.2)(7.32)}{6} [(76.2 \sin 30)^2 + (2.44 \cos 30)^2] = 1.013 \times 10^9 \text{ kg-m}^2 \quad (\text{A14})$$

Finally, the yaw mass moment of inertia is given by Equation A11

$$I_{zz_{tot}} = 2.364 \times 10^9 \text{ kg-m}^2 \quad (\text{A15})$$

# **Appendix B**

## **Time Series of External, Internal, and Net Pressure Gage Statistics**

---

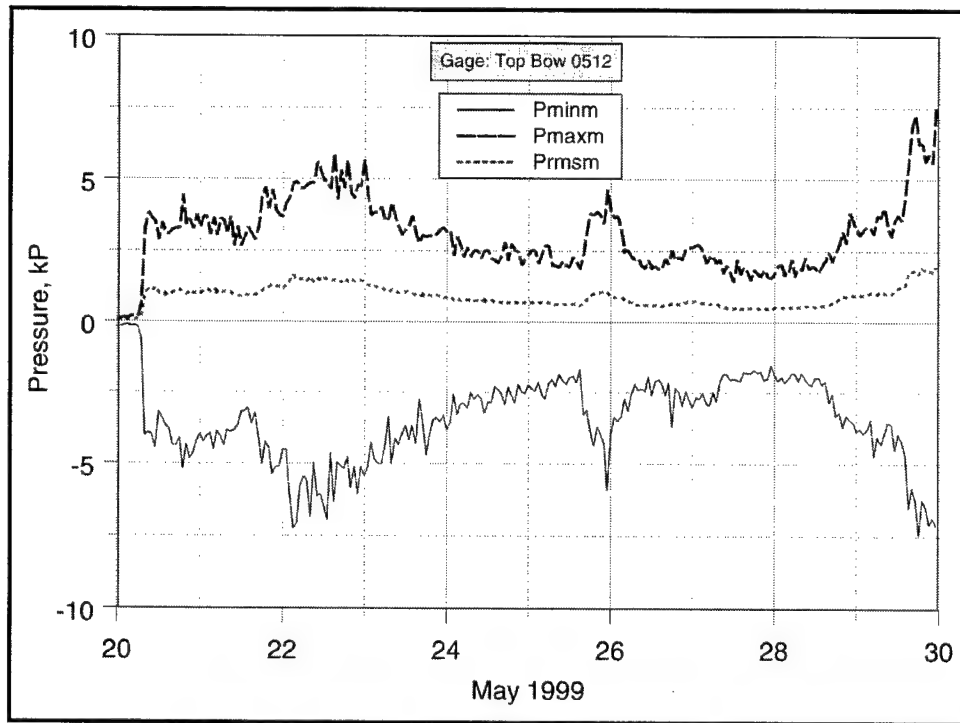


Figure B1. Time series of external pressure gage statistics for top bow location

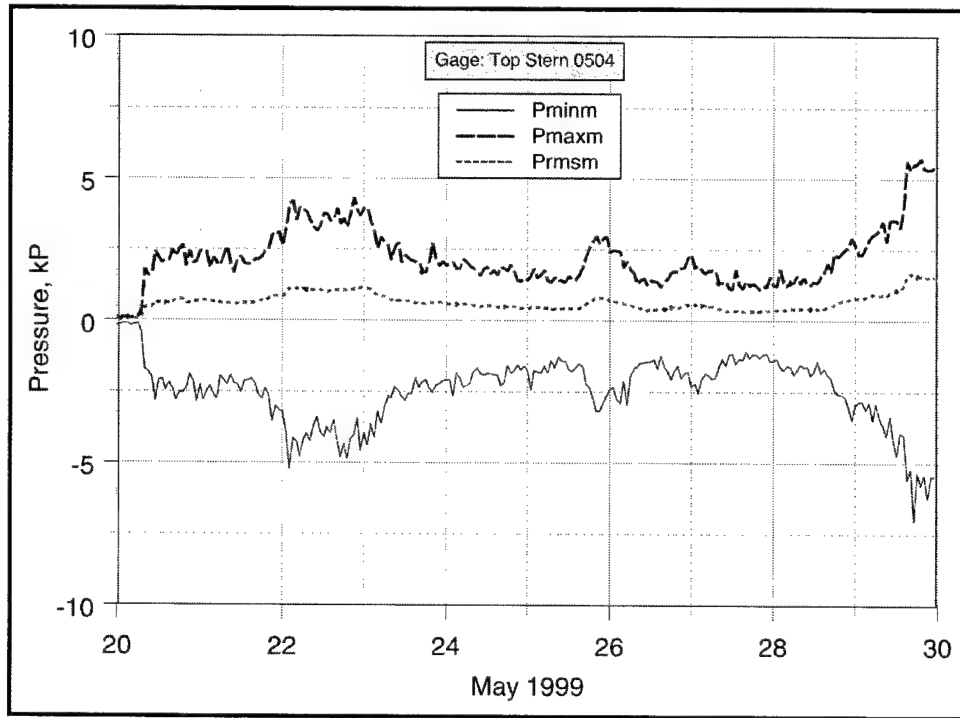


Figure B2. Time series of external pressure gage statistics for top stern location

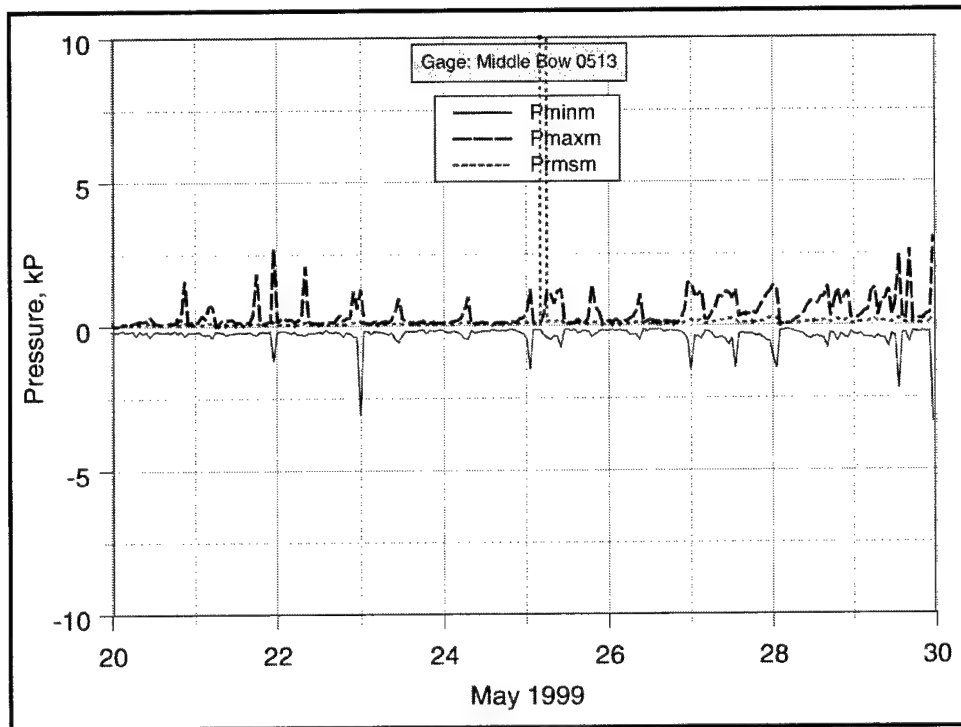


Figure B3. Time series of external pressure gage statistics for middle bow location

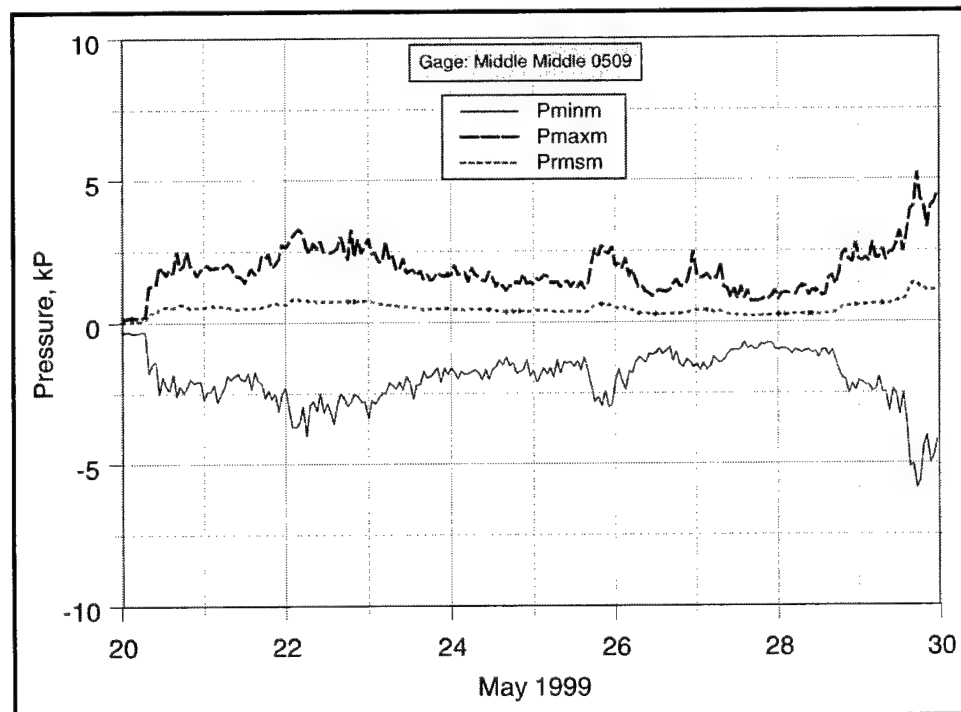


Figure B4. Time series of external pressure gage statistics for middle middle location

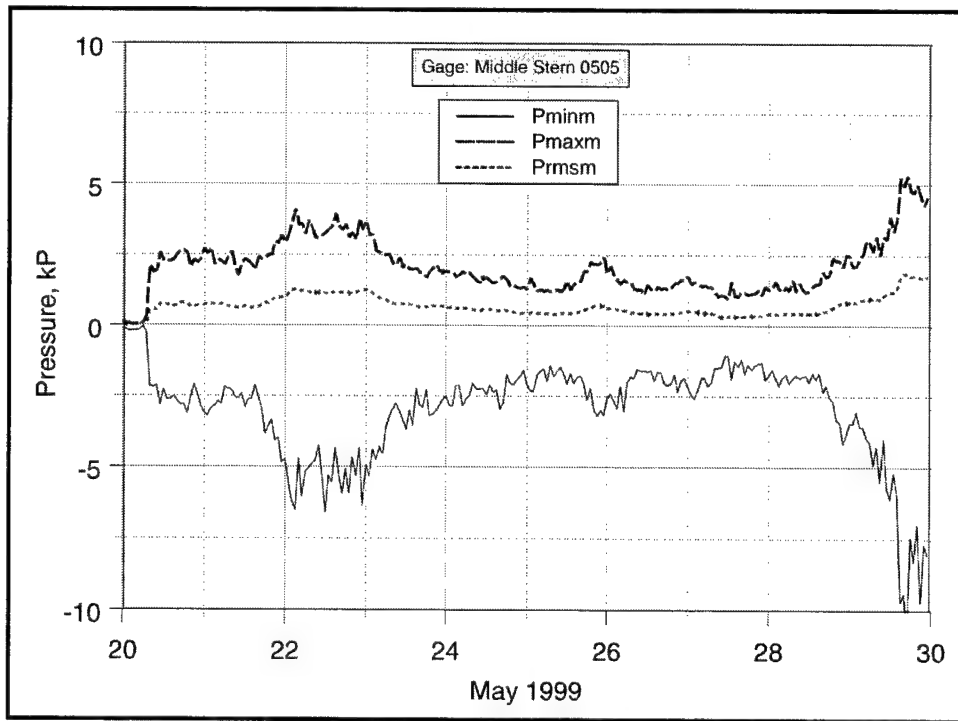


Figure B5. Time series of external pressure gage statistics for middle stern location

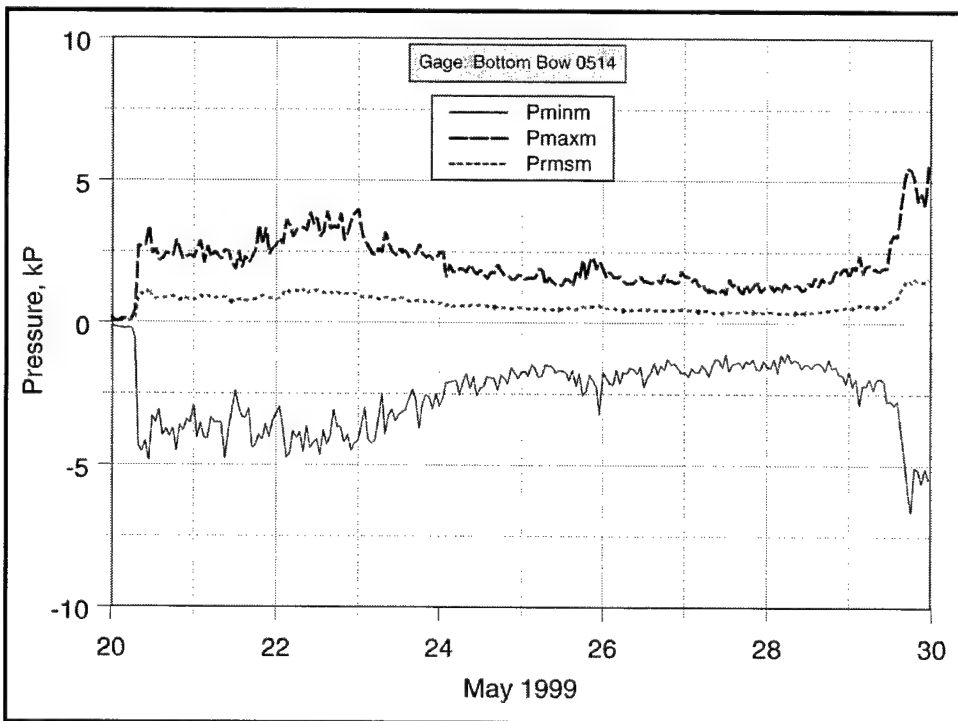


Figure B6. Time series of external pressure gage statistics for bottom bow location

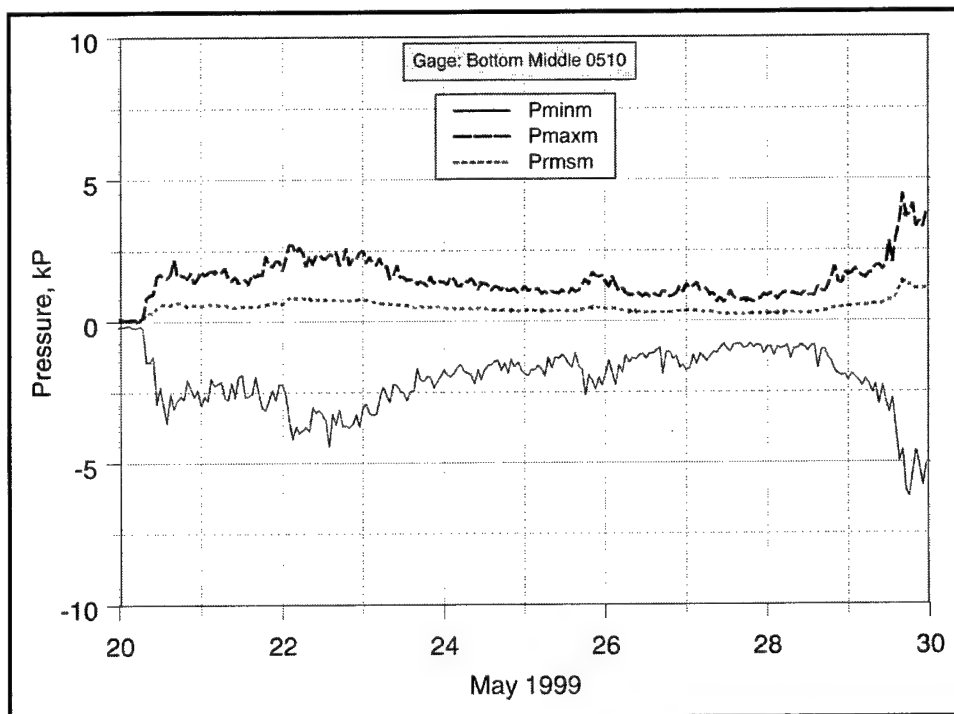


Figure B7. Time series of external pressure gage statistics for bottom middle location

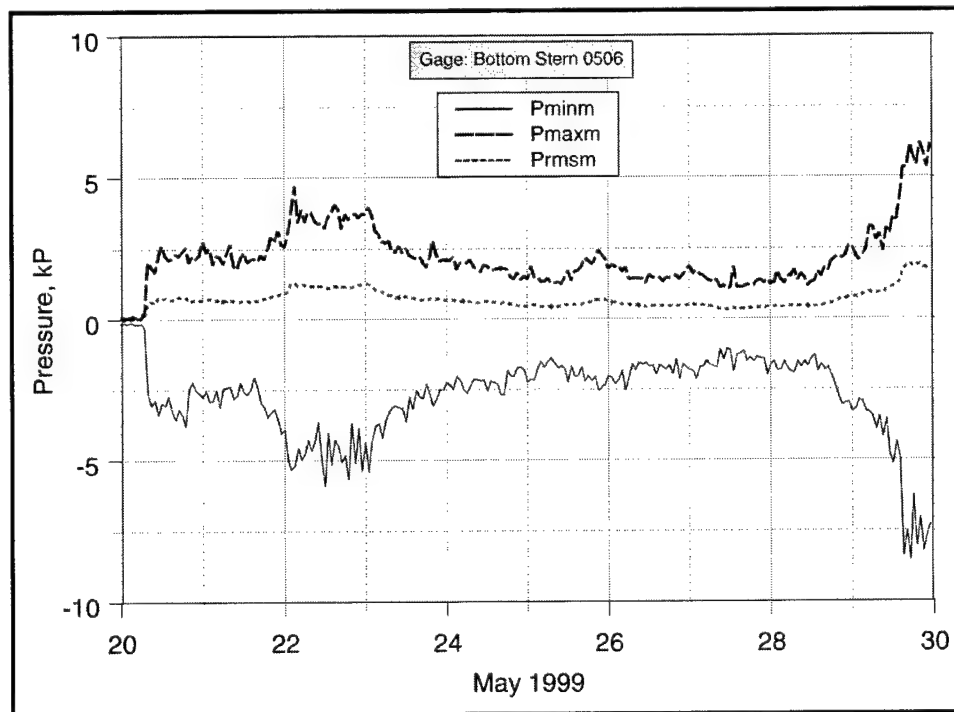


Figure B8. Time series of external pressure gage statistics for bottom stern location

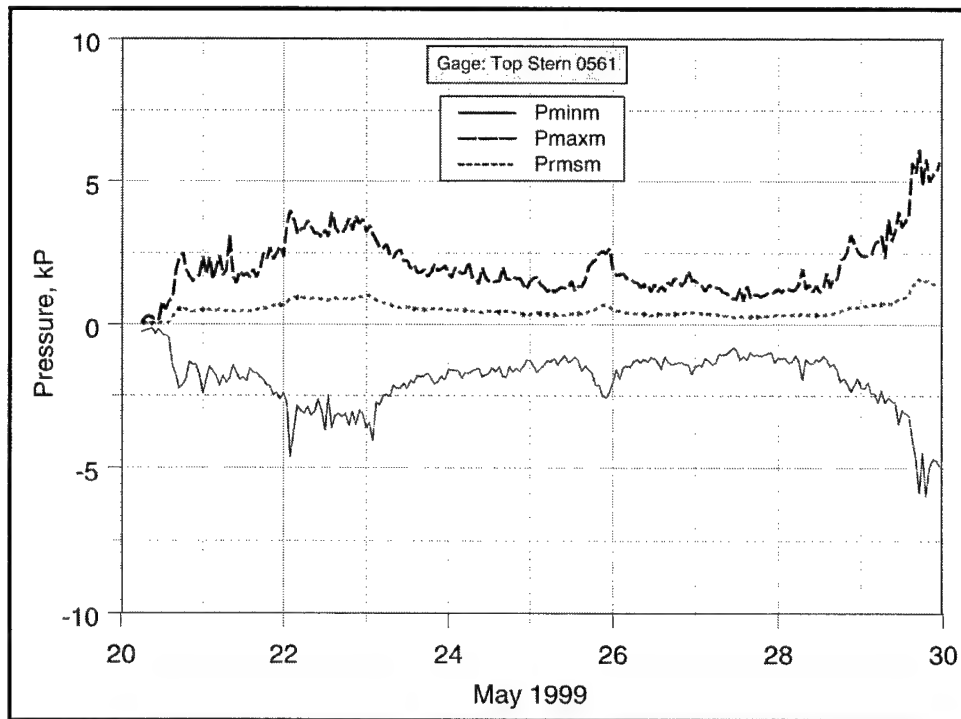


Figure B9. Time series of internal pressure gage statistics for top stern location

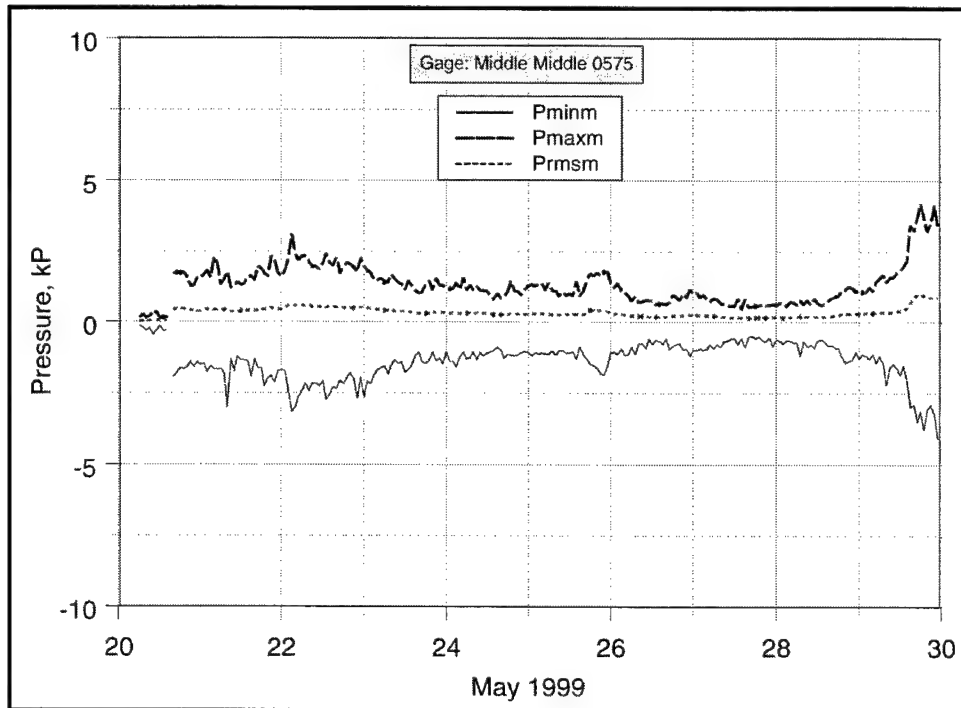


Figure B10. Time series of internal pressure gage statistics for middle middle location

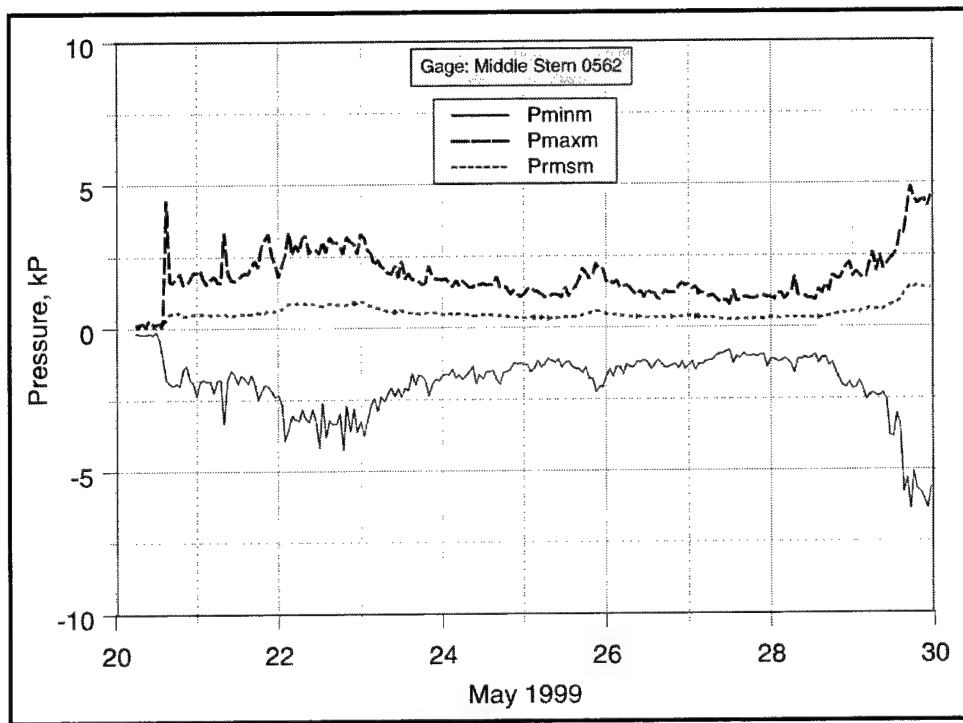


Figure B11. Time series of internal pressure gage statistics for middle stern location

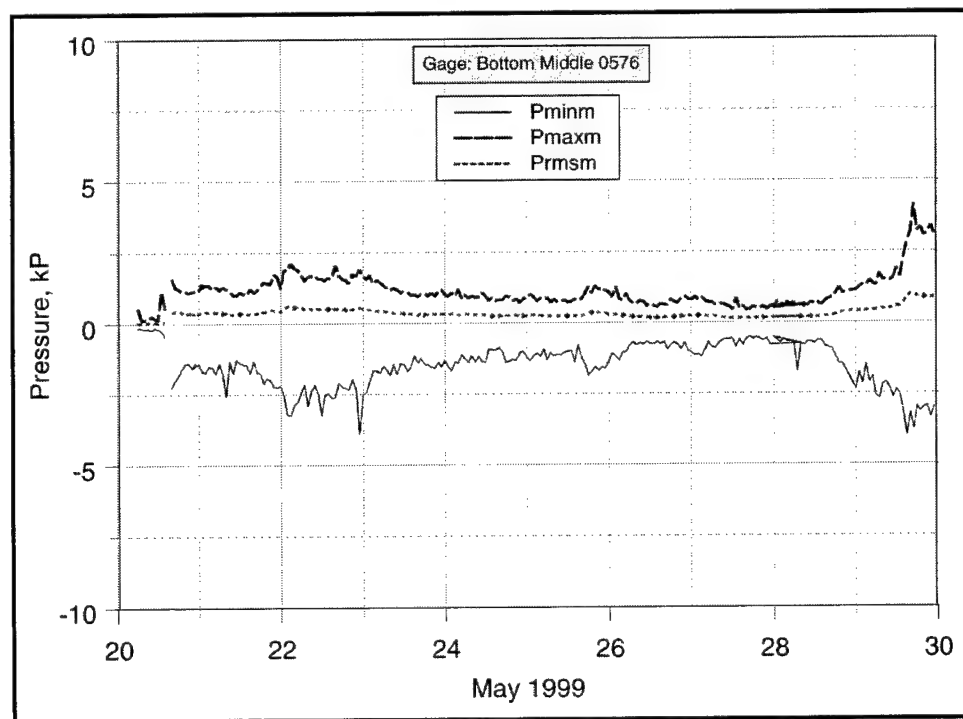


Figure B12. Time series of internal pressure gage statistics for bottom middle location

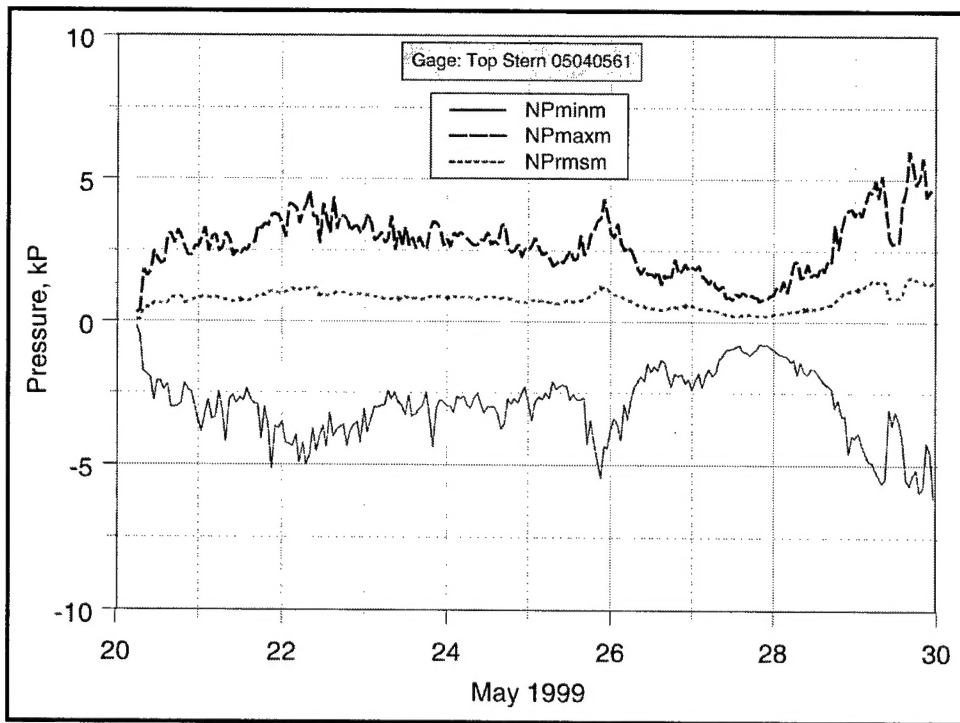


Figure B13. Time series of net pressure gage statistics for top stern location

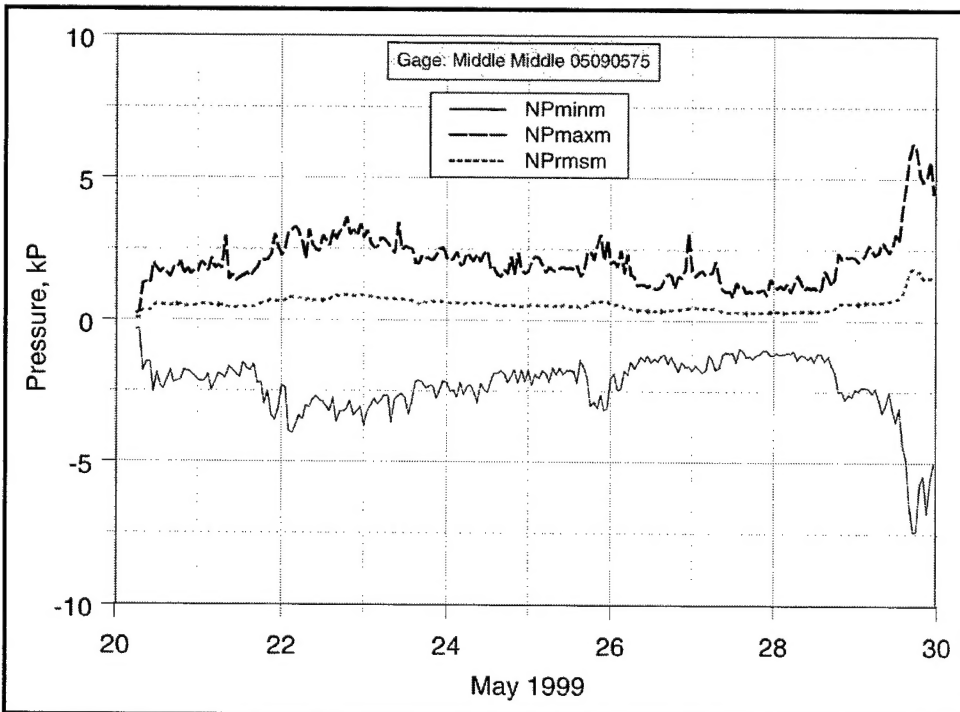


Figure B14. Time series of net pressure gage statistics for middle middle location

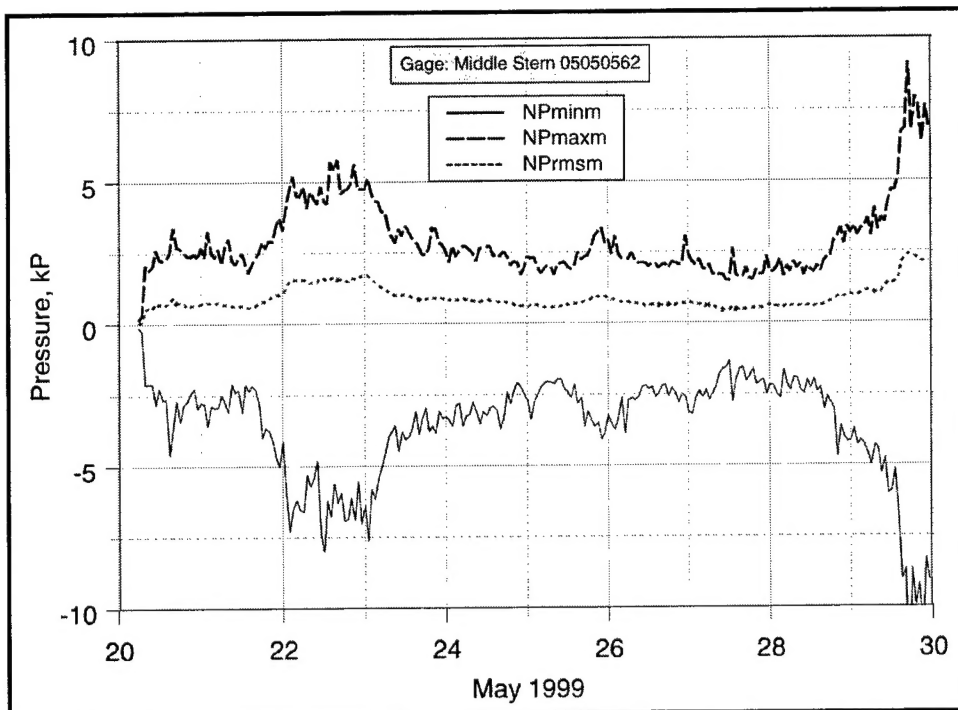


Figure B15. Time series of net pressure gage statistics for middle stern location

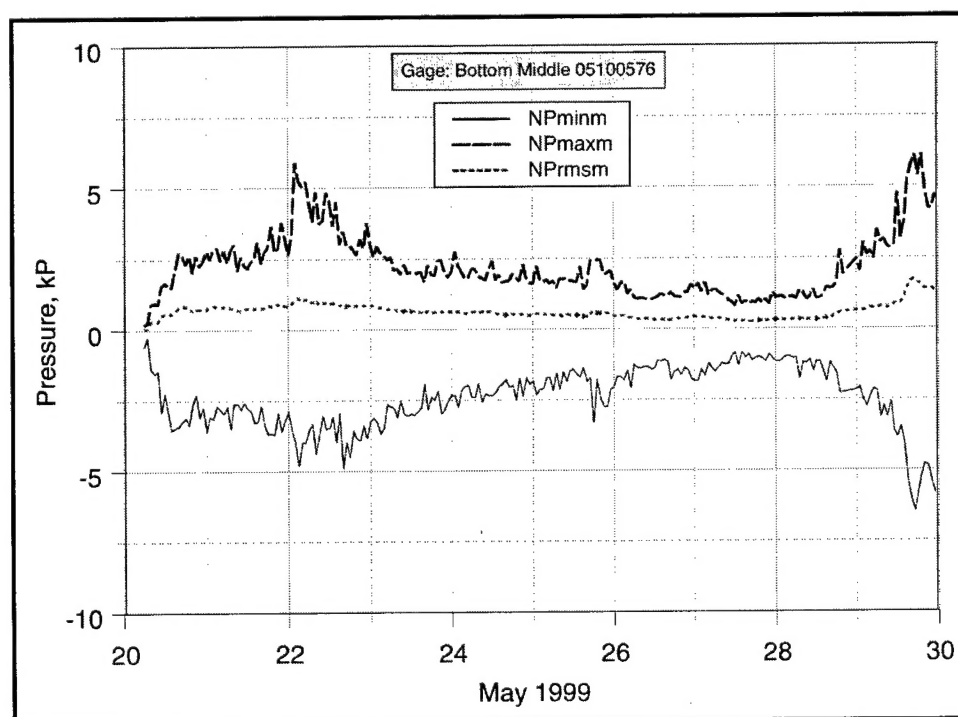


Figure B16. Time series of net pressure gage statistics for bottom middle location

# REPORT DOCUMENTATION PAGE

Form Approved  
OMB No. 0704-0188

Public reporting burden for this collection of information is estimated to average 1 hour per response, including the time for reviewing instructions, searching existing data sources, gathering and maintaining the data needed, and completing and reviewing this collection of information. Send comments regarding this burden estimate or any other aspect of this collection of information, including suggestions for reducing this burden to Department of Defense, Washington Headquarters Services, Directorate for Information Operations and Reports (0704-0188), 1215 Jefferson Davis Highway, Suite 1204, Arlington, VA 22202-4302. Respondents should be aware that notwithstanding any other provision of law, no person shall be subject to any penalty for failing to comply with a collection of information if it does not display a currently valid OMB control number. PLEASE DO NOT RETURN YOUR FORM TO THE ABOVE ADDRESS.

1. REPORT DATE (DD-MM-YYYY) September 2001		2. REPORT TYPE Final report		3. DATES COVERED (From - To)	
4. TITLE AND SUBTITLE  Analytical and Numerical Models of the RIBS XM99 Ocean-Scale Prototype				5a. CONTRACT NUMBER	
				5b. GRANT NUMBER	
				5c. PROGRAM ELEMENT NUMBER	
6. AUTHOR(S)  Michael J. Briggs				5d. PROJECT NUMBER	
				5e. TASK NUMBER	
				5f. WORK UNIT NUMBER	
7. PERFORMING ORGANIZATION NAME(S) AND ADDRESS(ES)  U.S. Army Engineer Research and Development Center Coastal and Hydraulics Laboratory 3909 Halls Ferry Road Vicksburg, MS 39180-6199				8. PERFORMING ORGANIZATION REPORT NUMBER  ERDC/CHL TR-01-19	
9. SPONSORING / MONITORING AGENCY NAME(S) AND ADDRESS(ES)  U.S. Army Corps of Engineers Washington, DC 20314-1000				10. SPONSOR/MONITOR'S ACRONYM(S)	
				11. SPONSOR/MONITOR'S REPORT NUMBER(S)	
12. DISTRIBUTION / AVAILABILITY STATEMENT  Approved for public release; distribution is unlimited.					
13. SUPPLEMENTARY NOTES					
14. ABSTRACT  This report describes analytical and numerical modeling efforts to quantify the performance and response of a new type of Rapidly Installed Breakwater System (RIBS) being developed at the U.S. Army Engineer Research and Development Center's (ERDC) Coastal and Hydraulics Center (CHL). The RIBS is a floating breakwater with two legs in a "V" shape in plan view which provide a sheltered region from waves and currents. The RIBS concept was initially developed to address problems encountered by military personnel during Logistics-Over-The-Shore (LOTS) operations. The primary problem occurs during these operations when sea states become elevated and negatively impact crews trying to discharge cargo and equipment onto smaller vessels from Tactical Auxiliary Crane Ships (TACS) and roll-on/roll-off (RO/RO) vessels. The performance of a floating breakwater can be quantified by the wave transmission coefficient. The structural response can be estimated using the wave-induced dynamic pressures along the structure. These pressures can be used to calculate the wave forces and moments. Preliminary results from the RIBS field study at Cape Canaveral, FL, May 1999, are presented and compared to analytical and numerical models of the RIBS wave transmission coefficient and dynamic wave pressures.					
15. SUBJECT TERMS  Analytical models Dynamic wave pressures		Floating breakwaters Joint Logistics over the Shore (JLOTS) Numerical models		Performance characteristics Prototype measurements Wave transmission coefficients	
16. SECURITY CLASSIFICATION OF:  a. REPORT UNCLASSIFIED			17. LIMITATION OF ABSTRACT	18. NUMBER OF PAGES 89	19a. NAME OF RESPONSIBLE PERSON
b. ABSTRACT UNCLASSIFIED					c. THIS PAGE UNCLASSIFIED

Destroy this report when no longer needed. Do not return it to the originator.